Chebyshev Spectral Method for Incompressible Viscous Flow with Boundary Layer Control via Suction or Blowing

by

Giuseppe Alescio

B.Eng., McGill University, Canada (1996)
M.Eng., McGill University, Canada (1998)

Submitted to the Department of Aeronautics and Astronautics
in partial fulfillment of the requirements for the degree of

Doctor of Philosophy

at the

MASSACHUSETTS INSTITUTE OF TECHNOLOGY

June 2006

Author_____
Department of Aeronautics and Astronautics
May 26, 2006

Certified by_____
Mark Drela
Professor of Aeronautics and Astronautics
Thesis Supervisor

Certified by_____
David L. Darmofal
Associate Professor of Aeronautics and Astronautics

Certified by_____
Jaime Peraire
Professor of Aeronautics and Astronautics

Certified by_____
Ian A. Waitz
Professor of Aeronautics and Astronautics

Accepted by_____
Jaime Peraire
Professor of Aeronautics and Astronautics
Chair, Committee on Graduate Students

Chebyshev Spectral Method for Incompressible Viscous Flow with Boundary Layer Control via Suction or Blowing

by

Giuseppe Alescio

Submitted to the Department of Aeronautics and Astronautics
on May 26, 2006, in partial fulfillment of the
requirements for the degree of
Doctor of Philosophy

Abstract

The MISES quasi 3-D design/analysis code implements a two-equation integral method with empirical closure relations to solve the boundary layer flow problem with or without suction, but lacks the option of flow control via blowing. The integral method is parameterized with the shape parameter $H \equiv \delta^*/\theta$ which cannot be applied to the blowing problem since $\theta \to 0$ downstream of the injection slot causing $H \to \infty$ — a computational disaster.

In this thesis, two alternate approaches are proposed to solve the blowing problem. First, a two-equation integral method parameterized with the profile parameters of a multi-deck representation of a turbulent jet based on Coles' law of the wake was formulated. The appearance of spurious singularities in the Jacobian matrices associated with the system of equations and the vector of unknowns prevented this method from being implemented. Second, a Chebyshev spectral method using the wall function technique was applied to the defect form of the incompressible viscous momentum equation. A turbulent jet profile was computed with $N = 40$ modes, a number low enough to allow the method's implementation into the MISES framework.

For the spectral approach, a stand-alone code was developed to solve laminar and turbulent flow over a flat plate with the following configurations: solid wall, porous wall with vertical suction/blowing, and fluid injection from an inclined slot. For the turbulent case, the Reynolds stress was replaced with a composite model for the eddy viscosity based on Spalding's law of the wall for the inner layer and Clauser's outer layer formulation. In the laminar regime, $N \sim 10$ modes are required for an accurate solution whereas the two-layer structure of a turbulent boundary layer increases this number to $N \sim 100$ modes. The incorporation of a wall function, consistent with the inner layer eddy viscosity model, in the approximation of the streamwise velocity, reduced the required number of modes by an order of magnitude — a major computational advantage.

The more general Spalart-Allmaras turbulence model was implemented in the spectral formulation to investigate the effect of using a wall function based on Spalding's law of the wall. For the flat plate case (solid wall), a small inconsistency between the wall function and the eddy viscosity model produced an erroneous shear stress near the wall. Nevertheless, the velocity profile was in close agreement with an accurate representation constructed from Spalding's law of the wall and Coles' law of the wake.

Thesis Supervisor: Mark Drela
Title: Professor of Aeronautics and Astronautics

Acknowledgments

I am indebted to Professor Drela for suggesting the topic of this thesis, for his guidance and support and, above all, for his patience throughout this endeavour. I would like to thank Professor Darmofal for his critical comments of the work as well as his many suggestions for improvement of the manuscript. Thanks to Professor Peraire for agreeing to serve as both committee member and minor advisor. Thanks to Professor Waitz for continuing to participate in all research meetings despite the shift to a more computationally-oriented project. Special thanks to Professor Sonin for agreeing to be an external reader and for giving me the opportunity to gain valuable teaching experience with his turbulent flow course. Thanks to Dr. Merchant for being an external reader and for always showing an interest in my work. Thanks to Bob Haimes for his expertise with system administration matters. Many thanks to Jean Sofronas for her help in scheduling the defense, for her administration of the lab, and for providing me with a seemingly endless supply of sticky notes. Special thanks to Marie Stuppard for her academic advice. Many thanks to the members of the ACDL (formerly the FDRL) for providing an environment conducive to both learning and having fun. Lastly, I would like to thank my family and friends for their love, support, and encouragement.

Contents

List of Figures

List of Tables

Chapter 1

Introduction

1.1 Motivation

The viscous/inviscid computational formulation and method of Drela and Giles [10] has become an established tool in the aircraft industry for airfoil design and analysis work. It has since been extended by Youngren [44] with the inclusion of streamtube thickness and rotation effects, permitting application to turbomachinery cascades. Further developments by Merchant [28, 29] have been to include boundary layer suction modeling in both the airfoil and the cascade formulations. Application of these methods to aspirated transonic compressor designs has been extremely successful, as described in Kerrebrock et al. [19, 20].

The ensuing research effort carried out on aspirated compressors in collaboration with the NASA Glenn Research Center has produced more promising designs. For instance, the loading limit with aspiration was doubled in the design of two high pressure ratio fan stages. This result was successfully demonstrated both computationally by Merchant [30] and experimentally by Schuler et al. [37] in MIT's Gas Turbine Laboratory. The aspiration concept has also led to the development of an advanced aerothermal design system which is an essential ingredient in the success of the program.

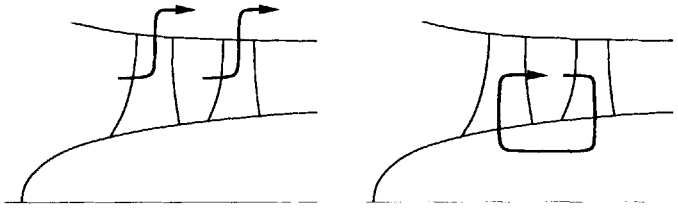

Figure 1-1: Aspirated compressor vis-à-vis a blown/aspirated compressor.

In an engine environment, however, it may not always be practical to use aspiration without incurring a penalty. The low total pressure in a front fan or first stage of a compressor makes it difficult to extract the flow. Alternatively, it may be more feasible to aspirate in high pressure regions of the compressor and blow in low pressure front stages (see Figure 1-1). The performance of a compressor could be improved by utilizing a suitable combination of both suction and blowing (see Figure 1-2). In order to investigate these alternate designs, flow control via blowing would have to be an added feature in the current suite of computational tools.

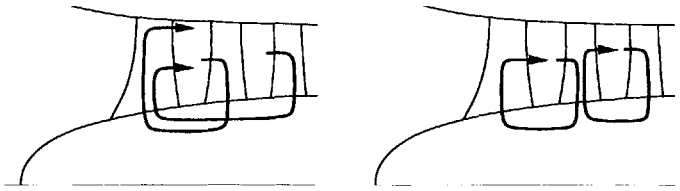

Figure 1-2: Blowing/suction flow possibilities in a compressor.

1.2 Integral Methods for Suction and Blowing

The MISES[1] quasi 3-D design/analysis code implements a two-equation integral method with empirical closure relations to solve the boundary layer flow problem with or without suction. The method is parameterized with the shape parameter $H \equiv \delta^*/\theta$, where δ^* and θ are, respectively, the displacement and momentum thicknesses. For flow with or without suction, δ^* and θ are both positive indicating a defect in mass and momentum of the viscous flow relative to the inviscid flow. Conversely, these thicknesses will be negative for a strong blowing case since there is now an excess of mass and momentum in the boundary layer. As the jet dissipates downstream, $\theta \rightarrow 0$ which will cause $H \rightarrow \infty$ — a computational disaster.

The value of the shape parameter is a good indicator of the state of the boundary layer. For a favourable pressure gradient, H is small but for an adverse pressure gradient, H is large. The comparison is usually made relative to the shape parameter values for a flat plate with no pressure gradient and for separated flow. In the laminar regime, $H \approx 2.6$ for a flat plate whereas at separation $H \approx 4$. In the turbulent regime, $H \approx 1.3$ for the flat plate and $H \approx 3$ at separation. Suction profiles will always have $H > 1$ and be far from the separation value. For a jet, the shape parameter values are meaningless since the ratio of δ^* to θ is non-unique.

Solving the blowing problem via the two-equation integral method requires new closure relations. In MISES, the skin friction, C_f, dissipation coefficient, C_D, etc. are all functions of the shape parameter H and Re_θ, the Reynolds number based on θ. These relations are useless for a jet since $H \rightarrow \infty$ as $\theta \rightarrow 0$ and $\mathrm{Re}_\theta < 0$ whenever $\theta < 0$. Conversely, the suction case requires no changes to these correlations since $H > 1$ and $\theta > 0$. In other words, suction is treated in the same fashion as the solid wall case with the exception of performing some record-keeping on the fluid removed from the boundary layer (i.e. source terms in the integral equations).

In Chapter 2, an integral method parameterized with the profile parameters of a multi-deck representation of a turbulent jet based on Coles' law of the wake [6] was proposed. The blowing model does a fairly good job in approximating experimental jet profile data. Consequently, the dimensionless form of both the von Kármán integral momentum equation and the integral Kinetic Energy (KE) equation were derived for each layer with the closure relations modeled in terms of the profile parameters. It was discovered that the Jacobian matrices associated with the system of equations and the vector of unknowns have spurious singularities. Conversely, applying the model to a wake profile and using the integral approach yields a well-constrained system. Therefore, the application of the integral boundary layer method to compute a multi-deck representation of a turbulent jet profile is inherently

[1]MISES is an acronym for Multiple blade Interacting Streamtube Euler Solver.

difficult. An alternate approach would have to be found to efficiently compute the blowing case within the MISES framework.

1.3 Spectral Method with Wall Function

In certain areas of computational fluid dynamics, spectral methods have become the prevailing numerical tool for large-scale computations [17]. The three-dimensional direct simulation of homogeneous turbulence, computation of transition in shear flows, and global weather modeling are typical examples. For many other applications, such as heat transfer, boundary layers, reacting flows, compressible flows, and magnetohydrodynamics, spectral methods have proven to be a viable alternative to the finite-difference and finite-element techniques.

Spectral methods are characterized by the expansion of the solution in terms of global and usually, orthogonal polynomials. Although originating in early-20th-century work of Galerkin and Lanczos, numerical spectral methods for partial differential equations (PDEs) were first developed by meteorologists in the 1950s. The expense of computing nonlinear terms remained a severe drawback until the early 1970s when Orszag [31] and Eliasen et al. [12] developed the transform methods that still form the backbone of many large-scale spectral computations.

These methods and others used in fluid mechanics prior to 1970 are termed spectral Galerkin methods. The fundamental unknowns are the expansion coefficients and the equations for these are derived by the techniques used in classical analysis. With the advent of the computer, an alternate discretization was made possible. Termed the spectral collocation technique, the fundamental unknowns are the solution values at selected collocation points and the series expansion is used solely for the purpose of approximating derivatives. This approach was proposed by Kreiss and Oliger [22] and by Orszag [32] in the early 1970s.

Boyd [2]) divides spectral methods into two broad categories using a more generic classification: interpolating and non-interpolating. The interpolating methods (comprised of the collocation or pseudospectral methods) associate a grid of points with each basis set. The coefficients of a known function are found by requiring that its truncated series agree with it at each point in the grid. In the case of a PDE, the associated residual is forced to vanish at each collocation point. The non-interpolating category includes Galerkin's method and the Lanczos tau-method [23]. There is no grid of interpolation points. Instead, the coefficients of a known function are computed by multiplying its truncated series by a given basis function and integrating. For a PDE, the residual is weighted by a given basis function and integrated.

In Chapter 3, the use of a Chebyshev spectral formulation (Galerkin-type approach) to curve-fit experimental turbulent jet profiles obtained from Zhou and Wygnanski [45] demonstrated that few modes are required to capture the outer layer profile. The inner layer could then be approximated using an appropriate wall function to complete the profile. The wall function technique is a common strategy employed in current Navier-Stokes methods to reduce the grid density requirements in the near-wall region. Spalding's law of the wall [39] is a good candidate since it captures the turbulent inner layer profile for flat plate flow and it has an eddy viscosity model associated with it.

The Galerkin form of the Chebyshev spectral method formulated with the defect form of the incompressible viscous momentum equation was developed. Application of the method to laminar flow over a flat plate with or without flow control was successful, as shown in

Chapter 4. The solution to the analogous turbulent flow problem, described in Chapter 5, required a large number of Chebyshev modes due to the two-layer structure of the boundary layer. An algebraic model for the eddy viscosity based on Spalding's law of the wall for the inner layer and Clauser's outer layer formulation [5] was implemented. Including a wall function in the velocity approximation that is consistent with the inner layer eddy viscosity model drastically reduced the number of Chebyshev modes. In the jet case, the number of modes is low enough to have the method coded into the MISES framework thus allowing design and analysis work on cascades with flow control via blowing.

1.4 Thesis Objective

The main objective of this thesis is:

- To develop a computationally efficient model for boundary layers with blowing in order to extend the capability of the MISES code to design turbomachinery cascades with this flow control method.

1.5 Contributions

The following is a summary of the main contributions of this thesis:

- First demonstration of the inherent difficulties of applying the two-equation integral method to solve the blowing problem with a multi-deck representation of a turbulent jet velocity profile based on Coles' law of the wake.
- First application of the Galerkin form of the Chebyshev spectral method to the defect form of the incompressible viscous momentum equation. Results for laminar and turbulent flow over a flat plate with or without boundary layer control are in excellent agreement with theory and/or experiment.
- First incorporation of Spalding's inner layer eddy viscosity model, in conjunction with Clauser's outer layer formulation, within an algebraic turbulence model for the spectral method described previously.
- First application of the wall function technique for the spectral method described previously. An order of magnitude reduction in Chebyshev modes is observed for all the test cases. Such a drastic drop in the number of modes can only be achieved if the wall function is consistent with the inner layer eddy viscosity model.
- First incorporation of the Spalart-Allmaras turbulence model within the spectral formulation as applied to the flat plate case with no flow control. The inconsistency between the wall function based on Spalding's law of the wall and the Spalart-Allmaras eddy viscosity is observed with an erroneous shear stress near the wall.

1.6 Overview

The thesis is structured in the following manner. Chapter 2 applies the integral method to a blowing model and spurious singularities are discovered in the Jacobian matrices associated

with the system of equations and the vector of unknowns. Chapter 3 presents the Galerkin form of the Chebyshev spectral method and applies it to a curve-fitting example. Chapter 4 applies the spectral method to solve the laminar incompressible boundary layer flow problem over a flat plate with or without flow control. Chapter 5 solves the analogous turbulent flow problem using an algebraic model for the eddy viscosity and then demonstrates the reduction in modes achieved with the incorporation of a wall function in the velocity approximation. Chapter 6 describes the Spalart-Allmaras turbulence model and applies it to the flat plate case with no flow control. Chapter 7 summarizes the contributions of the thesis and offers a few recommendations for future work. Appendix A presents the Falkner-Skan wedge flows which are used for comparison purposes with the spectral solution. In Appendix B, boundary layer separation in a diffuser is computed via the two-equation integral method and the results are compared to those obtained from the spectral formulation.

Chapter 2

Integral Method

An integral method parameterized with the profile parameters of a multi-deck representation of a turbulent jet based on Coles' law of the wake [6] is proposed. The blowing model does a fairly good job in approximating experimental jet profile data. Consequently, the dimensionless form of both the von Kármán integral momentum equation and the integral Kinetic Energy (KE) equation are derived for each layer with the closure relations modeled in terms of the profile parameters. It was discovered that the Jacobian matrices associated with the system of equations and the vector of unknowns have spurious singularities. Conversely, applying the model to a wake profile and using the integral approach yields a well-constrained system. Therefore, the application of the integral boundary layer method to compute a multi-deck representation of a turbulent jet profile is inherently difficult.

2.1 Blowing Model

Consider modeling a turbulent jet profile using a multi-deck representation as shown in Figure 2-1. Coles' law of the wake [6] is used to express the velocity profile in each layer given by

$$\begin{aligned} &\text{Top} && u = u_Y + (u_e - u_Y)\,\tfrac{1}{2}\left[1 - \cos\left(\pi \tfrac{y-Y}{\delta - Y}\right)\right], && Y \le y \le \delta, \\ &\text{Bottom} && u = u_0 + (u_Y - u_0)\,\tfrac{1}{2}\left[1 - \cos\left(\pi \tfrac{y}{Y}\right)\right], && 0 \le y \le Y. \end{aligned} \tag{2.1}$$

In these expressions, u_0 and u_Y are, respectively, the streamwise velocities at $y = 0$ and $y = Y$. The boundary layer thickness is denoted by δ and u_e is the edge velocity (streamwise component).

This simple model was applied to sets of turbulent jet profiles obtained from experiments conducted by Zhou and Wygnanski [45] as shown in Figures 2-2 to 2-4. The data from three jet strengths $u_\infty/u_{\text{jet}} = \{0.085, 0.59, 0.38\}$ each consisting of five profiles measured at 32, 100, 200, 300, and 400 mm from the slot location were used.

The experimental jet velocity was first normalized with its edge velocity such that $U_{\text{exp}} = u_{\text{exp}}/u_e$. Next, the MATLAB[1] piecewise cubic Hermite interpolation technique was used to approximate the profile with 181 points. The points were chosen by setting $x = -\cos\varphi$ with φ ranging from $[0, \pi]$ in increments of $\pi/180$ and then applying the transformation $\eta = (x+1)/2$ such that $\eta = y/\delta$ ranges from $[0, 1]$. Using the interpolated jet velocity

[1]The Mathworks, Inc., Natick, MA, `http://www.mathworks.com`

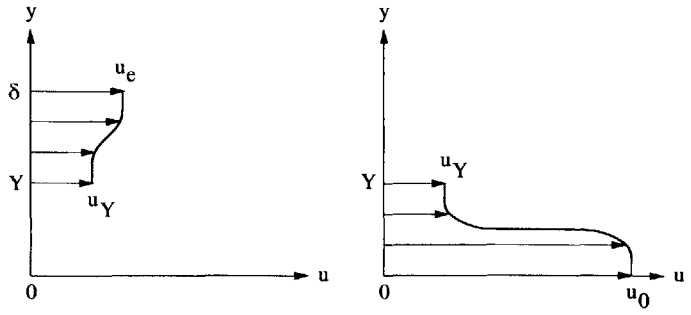

Figure 2-1: Multi-deck representation of the jet profile.

$U_{\text{int}} = u_{\text{int}}/u_e$, the maximum velocity in each profile was set to $U_0 = u_0/u_e$ whereas the minimum velocity in the outer layer was set to $U_Y = u_Y/u_e$. The location of U_Y will be Y/δ in the normalized η coordinate. Hence, the model profiles can be constructed and compared.

Overall, the blowing model does a fairly good job of approximating the experimental profiles. Figure 2-2 is a pathological case for the model since $Y = \delta$ (where $u_Y = u_e$). The top layer cannot be used since the denominator of the cosine function blows up. The same would be true for the bottom layer if $Y = 0$ (where $u_Y = u_0$). Figures 2-3 and 2-4 represent the types of profiles the model was intended to predict. Due to this close agreement between model and experiment, there was substantial motivation to attempt to include blowing in an integral formulation.

2.2 Integral Boundary Layer Equations

2.2.1 Turbulent Flow

The 2-D, steady, incompressible Reynolds-averaged continuity and x-momentum thin shear layer equations governing the real viscous flow (RVF) in the turbulent regime are given by

$$\frac{\partial u}{\partial x} + \frac{\partial v}{\partial y} = 0, \tag{2.2}$$

$$\frac{\partial}{\partial x}\left(u^2\right) + \frac{\partial}{\partial y}\left(uv\right) + \frac{1}{\rho}\frac{\partial p}{\partial x} - \frac{1}{\rho}\frac{\partial \tau}{\partial y} = 0. \tag{2.3}$$

In these expressions, u and v are, respectively, the x- and y-components of the RVF velocity; ρ is the mass density; p is the static pressure and τ is the shear stress given by

$$\tau = \mu\frac{\partial u}{\partial y} - \rho\overline{u'v'}, \tag{2.4}$$

where μ is the dynamic viscosity and $-\rho\overline{u'v'}$ is the turbulent shear (or Reynolds stress).

2.2.2 Dimensional Form

Integrating across the shear layer (see Drela [9])

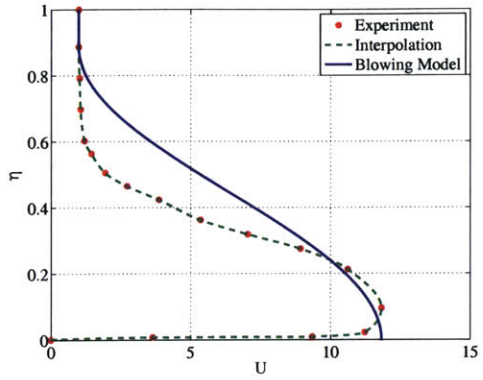

(a) 32 mm

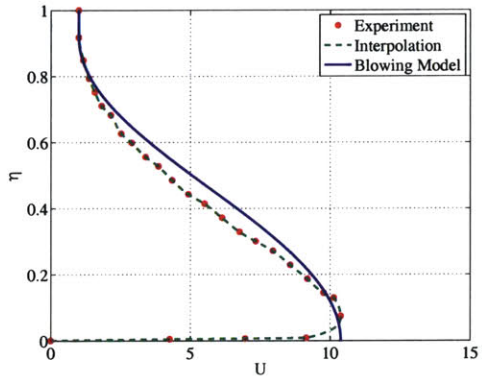

(b) 100 mm

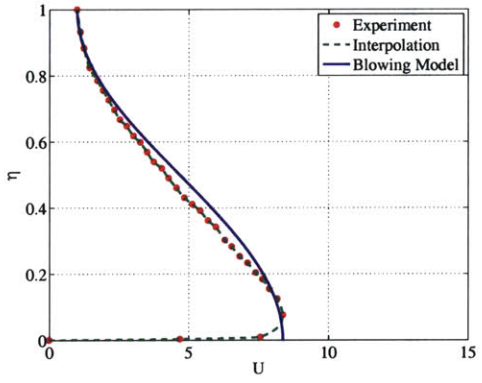

(c) 200 mm

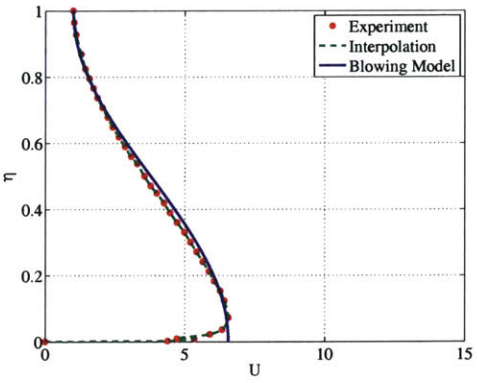

(d) 300 mm

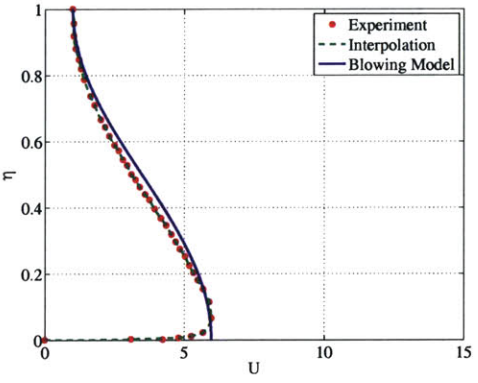

(e) 400 mm

Figure 2-2: Blowing model results: Jet strength $u_\infty/u_{\text{jet}} = 0.085$.

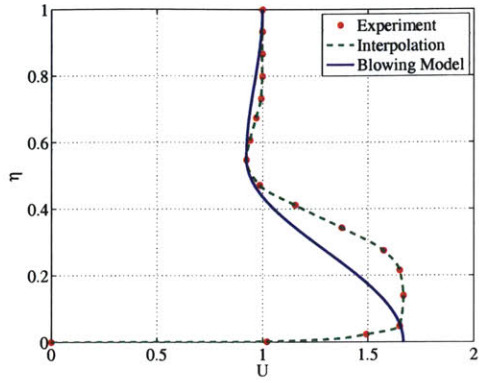

(a) 32 mm

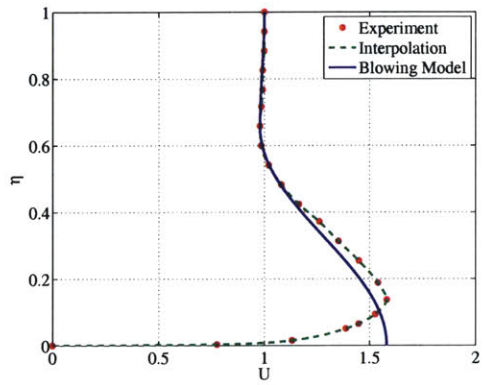

(b) 100 mm

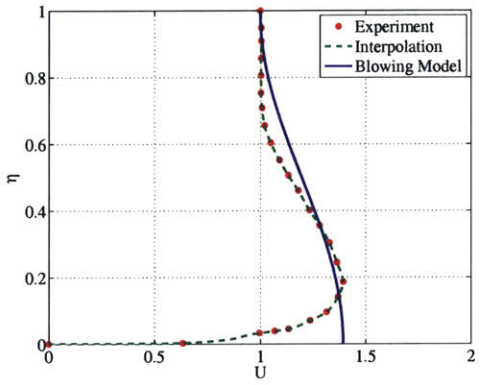

(c) 200 mm

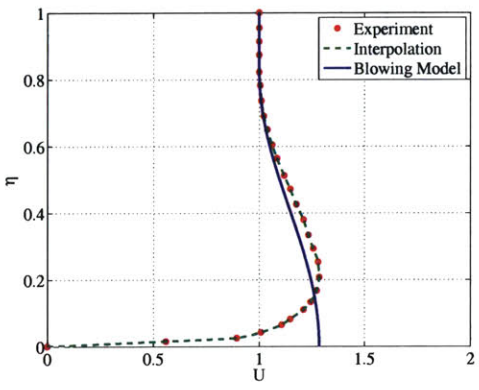

(d) 300 mm

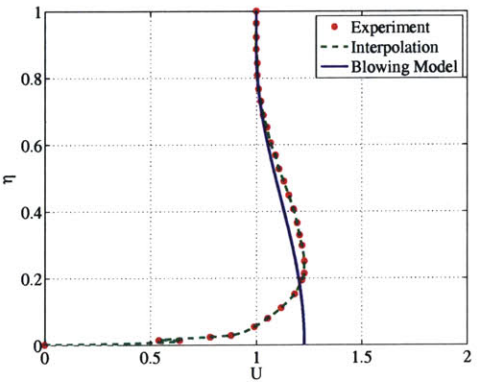

(e) 400 mm

Figure 2-3: Blowing model results: Jet strength $u_\infty/u_{\text{jet}} = 0.59$.

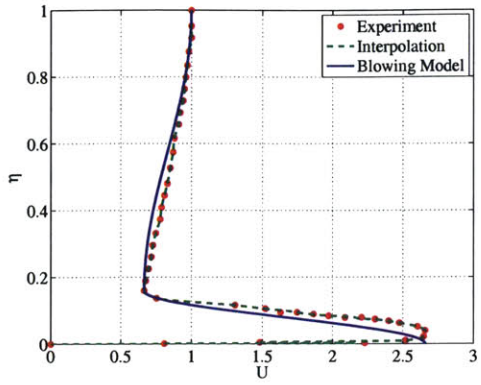

(a) 32 mm

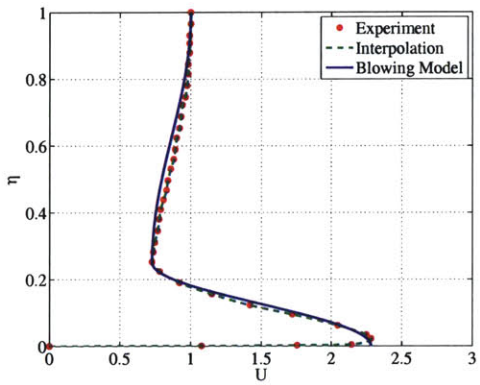

(b) 100 mm

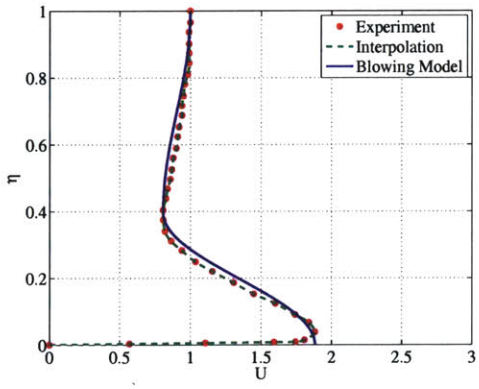

(c) 200 mm

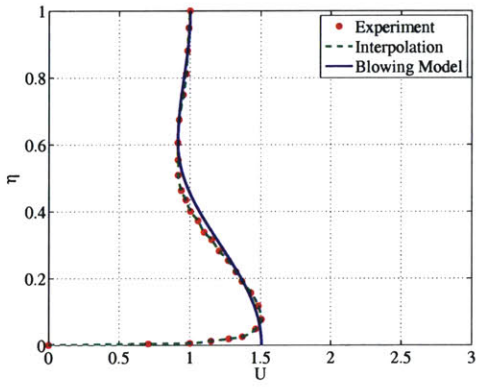

(d) 300 mm

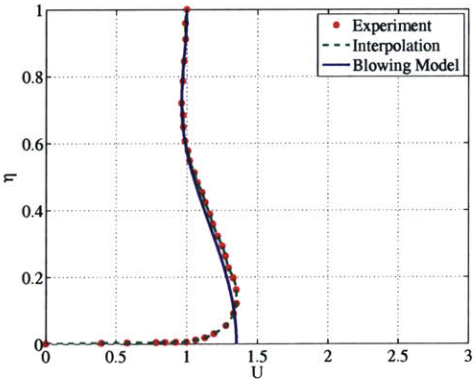

(e) 400 mm

Figure 2-4: Blowing model results: Jet strength $u_\infty/u_{\text{jet}} = 0.38$.

$$\int_{Y_1}^{Y_2} \left[(u-u_e)\times(2.2)+(2.3)\right] dy, \tag{2.5}$$

$$\int_{Y_1}^{Y_2} \left[\left(u^2-u_e^2\right)\times(2.2)+2u\times(2.3)\right] dy, \tag{2.6}$$

yields the dimensional form of both the von Kármán integral momentum equation and the integral Kinetic Energy (KE) equation

$$\frac{d}{dx}\left(\rho_e u_e^2\theta\right)+\rho_e u_e\delta^*\frac{du_e}{dx}-\tau_1+\tau_2=\rho_2 E_2\left(u_e-u_2\right)-\rho_1 E_1\left(u_e-u_1\right), \tag{2.7}$$

$$\frac{d}{dx}\left(\rho_e u_e^3\theta^*\right)-2D-2u_1\tau_1+2u_2\tau_2=\rho_2 E_2\left(u_e^2-u_2^2\right)-\rho_1 E_1\left(u_e^2-u_1^2\right). \tag{2.8}$$

These equations involve the standard integral definitions for the displacement thickness δ^*, momentum thickness θ, and KE thickness θ^* given by

$$\delta^* \equiv \int_{Y_1}^{Y_2}\left(1-\frac{u}{u_e}\right) dy, \tag{2.9}$$

$$\theta \equiv \int_{Y_1}^{Y_2}\left(1-\frac{u}{u_e}\right)\frac{u}{u_e} dy, \tag{2.10}$$

$$\theta^* \equiv \int_{Y_1}^{Y_2}\left(1-\frac{u^2}{u_e^2}\right)\frac{u}{u_e} dy. \tag{2.11}$$

The shear dissipation D and entrainment velocity E, which is the velocity component normal to the demarkation line $Y(x)$ as shown in Figure 2-5, are defined by

$$D \equiv \int_{Y_1}^{Y_2} \tau\frac{\partial u}{\partial y} dy \qquad \text{and} \qquad E \equiv u\frac{dY}{dx}-v. \tag{2.12}$$

The pressure gradient term has been written in terms of the edge velocity u_e. This comes from the assumption that in a boundary layer

$$p(x,y)\approx p(x)=p_e(x), \tag{2.13}$$

where $p_e(x)$ is the static pressure at the edge and using Bernoulli, it can be shown that

$$\frac{dp_e}{dx}=-\rho_e u_e\frac{du_e}{dx}. \tag{2.14}$$

The edge density $\rho_e=\rho$ since the flow is incompressible.

For a single (solid) wall boundary layer, the integration is typically performed across the entire layer. In this case, Y_1 is at the wall where $u_1=E_1=0$ and Y_2 is outside the layer where $u_e-u_2=\tau_2=0$. This results in both righthand sides being zero and gives the more familiar entrainment-free forms of these equations. For multi-deck representations of confluent shear layers the entrainment terms will be present. Moreover, if flow control via blowing occurs over a slot (usually inclined at some angle and flush with the surface), the no-slip condition will not hold. Over the slot, $u_1=u_w$ and $v_1=v_w$ which are, respectively, the streamwise and normal velocity components of the fluid that is either removed or injected.

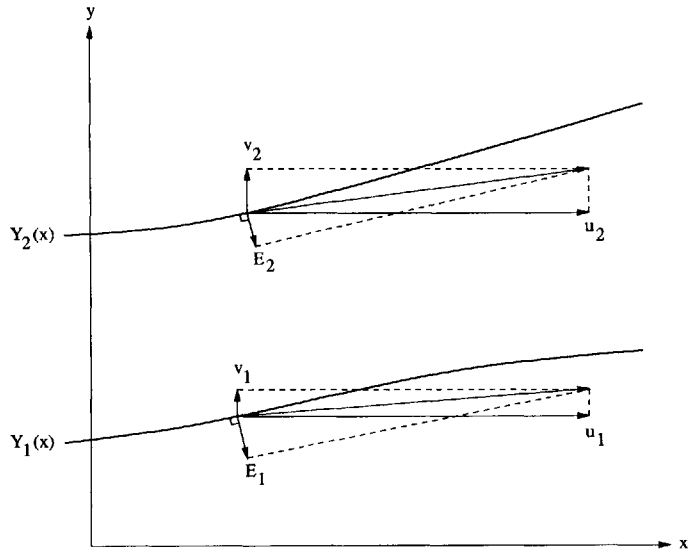

Figure 2-5: Layer demarkation lines and entrainment velocities.

The governing equations for the blowing model can be derived by performing two integrations. First, integrate from $Y_1 = 0$ to $Y_2 = Y$ to obtain the governing equations for the bottom layer. Second, integrate over the entire layer and remove the respective von Kármán integral momentum and KE integral equations from the bottom layer to obtain the top layer equations. Lastly, express these equations in dimensionless form as required in the MISES framework.

2.2.3 Dimensionless Form

The dimensionless form of both the von Kármán integral momentum equation and the integral KE equation governing the entire boundary layer for the blowing case are

$$\frac{d\theta}{dx} + \left(\frac{\delta^*}{\theta} + 2\right)\frac{\theta}{u_e}\frac{du_e}{dx} = \frac{\rho_w v_w}{\rho_e u_e}\left(1 - \frac{u_w}{u_e}\right) + \frac{C_f}{2}, \tag{2.15}$$

$$\frac{d\theta^*}{dx} + 3\frac{\theta^*}{u_e}\frac{du_e}{dx} = \frac{\rho_w v_w}{\rho_e u_e}\left(1 - \frac{u_w^2}{u_e^2}\right) + \frac{u_w}{u_e}C_f + 2C_D, \tag{2.16}$$

whereas the bottom layer is governed by

$$\frac{d\theta_Y}{dx} + \left(\frac{\delta_Y^*}{\theta_Y} + 2\right)\frac{\theta_Y}{u_e}\frac{du_e}{dx} = \frac{\rho_Y E_Y}{\rho_e u_e}\left(1 - \frac{u_Y}{u_e}\right) + \frac{\rho_w v_w}{\rho_e u_e}\left(1 - \frac{u_w}{u_e}\right) + \frac{C_f}{2}, \tag{2.17}$$

$$\frac{d\theta_Y^*}{dx} + 3\frac{\theta_Y^*}{u_e}\frac{du_e}{dx} = \frac{\rho_Y E_Y}{\rho_e u_e}\left(1 - \frac{u_Y^2}{u_e^2}\right) + \frac{\rho_w v_w}{\rho_e u_e}\left(1 - \frac{u_w^2}{u_e^2}\right) + \frac{u_w}{u_e}C_f + 2C_{D_Y}. \tag{2.18}$$

The skin friction C_f and dissipation coefficient C_D are defined by

$$C_f \equiv \frac{\tau_w}{\frac{1}{2}\rho_e u_e^2} \qquad \text{and} \qquad C_D \equiv \frac{D}{\rho_e u_e^3}, \tag{2.19}$$

where τ_w is the shear stress at the wall given by

$$\tau_w = \mu \left.\frac{\partial u}{\partial y}\right|_{y=0}. \tag{2.20}$$

The Y subscript on the terms δ_Y^*, θ_Y, θ_Y^* and C_{D_Y} indicates that the limits of the integration go from 0 to Y. The entrainment velocity at the height Y is denoted E_Y. The term $\rho_w v_w$ represents the injected mass flux and u_w is the streamwise velocity component of the injected fluid.

2.3 Inherent Difficulties

For the blowing case, the vectors of unknowns and profile parameters are, respectively, $\mathbf{U}$ and $\mathbf{W}$ given by

$$\mathbf{U} = \begin{bmatrix} \theta - \theta_Y \\ \delta^* - \delta_Y^* \\ \theta_Y \\ \delta_Y^* \end{bmatrix} \qquad \text{and} \qquad \mathbf{W} = \begin{bmatrix} Y \\ \delta \\ U_Y \\ U_0 \end{bmatrix}. \tag{2.21}$$

Appropriate closure relations can be modeled for C_f, C_D, E_Y, etc. in terms of $\mathbf{W}$ such that the governing equations can be expressed as

$$\frac{d}{dx}\mathbf{V}(\mathbf{W}) = f(\mathbf{W}), \tag{2.22}$$

where the vector $\mathbf{V}$ is given by

$$\mathbf{V} = \begin{bmatrix} \theta - \theta_Y \\ \theta^* - \theta_Y^* \\ \theta_Y \\ \theta_Y^* \end{bmatrix}. \tag{2.23}$$

By performing the chain rule and inverting yields

$$\frac{d\mathbf{W}}{dx} = \left[\frac{\partial \mathbf{V}}{\partial \mathbf{W}}\right]^{-1} f(\mathbf{W}), \tag{2.24}$$

where $[\partial \mathbf{V}/\partial \mathbf{W}]$ is the Jacobian matrix for the system of equations. Furthermore, since $\mathbf{U} = g(\mathbf{W})$ then to determine $\mathbf{W}$ given $\mathbf{U}$ requires $[\partial \mathbf{U}/\partial \mathbf{W}]^{-1}$. The term $[\partial \mathbf{U}/\partial \mathbf{W}]$ is the Jacobian matrix for the vector of unknowns.

It turns out that both these Jacobian matrices have spurious singularities as shown in Figure 2-6. These contour plots were obtained by varying U_0 in the range $[0, 4]$ and U_Y in the range $[0, 1]$. The ratio $Y/\delta = 0.2$ with δ being set to unity. The value of δ is required since the integral thicknesses are lengths.

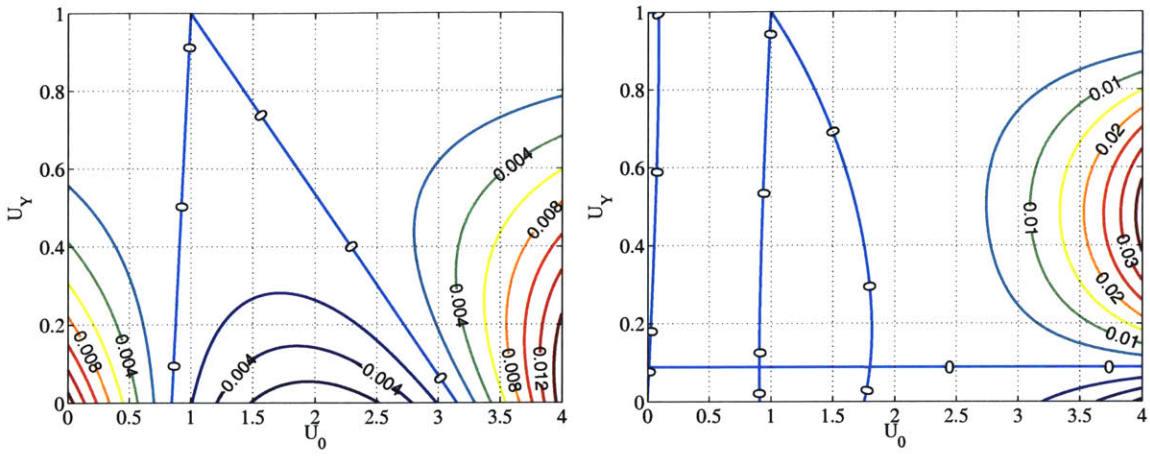

(a) $|\partial \mathbf{U}/\partial \mathbf{W}|$ (b) $|\partial \mathbf{V}/\partial \mathbf{W}|$

Figure 2-6: Singularities in Jacobian matrices for the jet.

2.4 Wake Model Comparison

As a means of comparison, the idea to model the jet profile with a two-layer velocity deck was applied to a wake profile as shown in Figure 2-7. In this case, the expression for the velocity profile in each layer is given by

$$\begin{aligned} &\text{Top} && u = u_{0+} + (u_e - u_{0+})\,\tfrac{1}{2}\left[1 - \cos\left(\pi \tfrac{y}{\delta^+}\right)\right], \quad 0 \le y \le \delta^+, \\ &\text{Bottom} && u = u_{0-} + (u_e - u_{0-})\,\tfrac{1}{2}\left[1 - \cos\left(\pi \tfrac{y}{\delta^-}\right)\right], \quad \delta^- \le y \le 0. \end{aligned} \tag{2.25}$$

In these expressions, u_{0+} and u_{0-} are, respectively, the streamwise velocities at $y = 0$ for the top and bottom layers. The boundary layer thicknesses are denoted δ^+ and δ^-. Note that these thicknesses cannot be zero or else the cosine function in the velocity expression for their respective layers will blow up. Furthermore, if $u_{0+} = u_e$ or $u_{0-} = u_e$, both δ^+ and δ^- will be ill-defined.

For the wake case, the vectors of unknowns and profile parameters are, respectively, $\mathbf{U}$ and $\mathbf{W}$ given by

$$\mathbf{U} = \begin{bmatrix} \theta - \theta_0 \\ \delta^* - \delta_0^* \\ \theta_0 \\ \delta_0^* \end{bmatrix} \quad \text{and} \quad \mathbf{W} = \begin{bmatrix} \delta^+ \\ \delta^- \\ U_{0+} \\ U_{0-} \end{bmatrix}. \tag{2.26}$$

In these expressions the 0 subscript indicates that the limits of the integration go from δ^- to 0. Thicknesses with no subscript have been integrated over the entire layer or from δ^- to δ^+. Furthermore, $U_{0+} = u_{0+}/u_e$ and $U_{0-} = u_{0-}/u_e$.

Following the same arguments as the blowing case, the vector $\mathbf{V}$ is given by

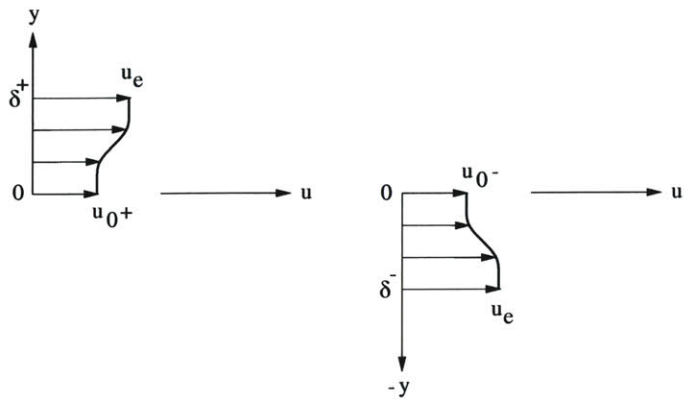

Figure 2-7: Multi-deck representation of a wake profile.

$$\mathbf{V} = \begin{bmatrix} \theta - \theta_0 \\ \theta^* - \theta_0^* \\ \theta_0 \\ \theta_0^* \end{bmatrix} \tag{2.27}$$

and the contour plots of the Jacobian matrices are shown in Figure 2-8. In this case, both U_{0-} and U_{0+} were varied in the range $[0, 1]$. The height δ^+ was set to unity and $\delta^- = -\delta^+$. The Jacobian matrix $[\partial\mathbf{U}/\partial\mathbf{W}]$ has no spurious singularities whereas $[\partial\mathbf{V}/\partial\mathbf{W}]$ has singularities at $U_{0-} = U_{0+} = \left(-5 + 2\sqrt{10}\right)/15$.

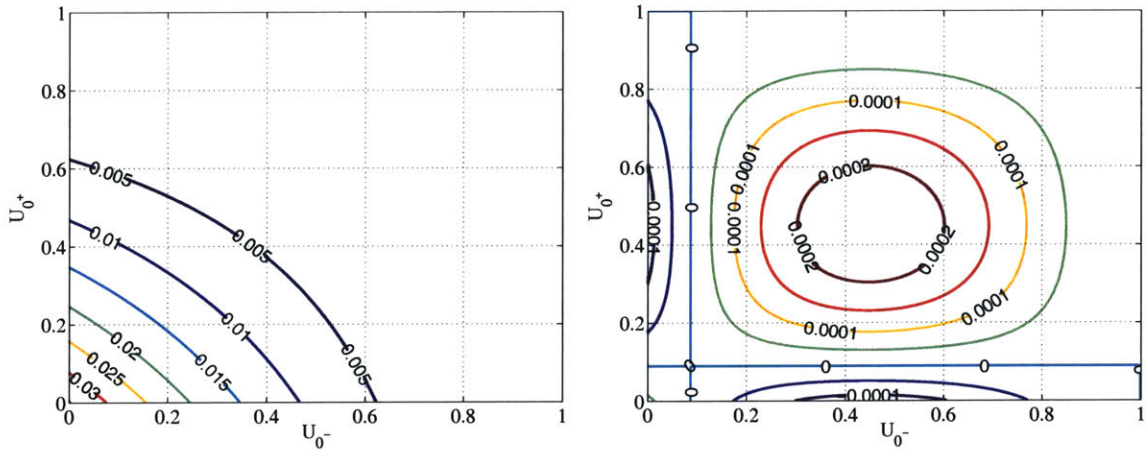

(a) $|\partial\mathbf{U}/\partial\mathbf{W}|$ (b) $|\partial\mathbf{V}/\partial\mathbf{W}|$

Figure 2-8: Singularities in Jacobian matrices for a wake.

2.5 Perturbation Analysis

In order to gain some insight as to what the singularities in $[\partial \mathbf{V}/\partial \mathbf{W}]$ mean to the set of integral equations, consider a perturbation $\delta \mathbf{V}$ due to the perturbation $\delta \mathbf{W_V}$ such that

$$\delta \mathbf{V} = \left[\frac{\partial \mathbf{V}}{\partial \mathbf{W}}\right] \delta \mathbf{W_V} = \lambda \mathbf{e} \delta \mathbf{W_V}, \tag{2.28}$$

where λ and $\mathbf{e}$ are, respectively, the diagonal matrix of eigenvalues and the matrix of eigenvectors associated with $[\partial \mathbf{V}/\partial \mathbf{W}]$. Denoting the zero eigenvalue corresponding to each singularity as λ_0 and its associated eigenvector as $\mathbf{e}_0$, the perturbation $\delta \mathbf{U}$ will be

$$\delta \mathbf{U} = \left[\frac{\partial \mathbf{U}}{\partial \mathbf{W}}\right] \underbrace{\mathbf{e}_0 \delta \mathbf{W_V}}_{\delta \mathbf{W_U}}. \tag{2.29}$$

For the wake, both singularities in $[\partial \mathbf{V}/\partial \mathbf{W}]$ produce a nonzero perturbation in the displacement thicknesses for each layer. Recall that in reality the edge velocity u_e, assumed given here, does depend on the displacement thickness δ^*. In fact, computing the flow past separation is only possible with Interacting Boundary Layer Theory (IBLT) where the governing equation for u_e is written in terms of δ^* and the geometry of the problem (see Appendix B). In Classical Boundary Layer Theory (CBLT), u_e is prescribed and the computation fails at the separation point due to the Goldstein singularity. Therefore, although $[\partial \mathbf{V}/\partial \mathbf{W}]$ has spurious singularities, the governing equation for u_e will prevent the Jacobian matrix for the entire system of equations from being singular for the wake case.

In the blowing case, both $[\partial \mathbf{U}/\partial \mathbf{W}]$ and $[\partial \mathbf{V}/\partial \mathbf{W}]$ have spurious singularities. Applying the above analysis to $[\partial \mathbf{V}/\partial \mathbf{W}]$ yields zero perturbations in both the momentum and displacement thicknesses for each layer. Hence, the Jacobian matrix for the entire system of equations will be singular. Therefore, using a two-equation integral boundary layer method to compute the multi-deck representation of a turbulent jet profile is inherently difficult. In the following chapters, an alternate approach is taken to efficiently compute the blowing case within the MISES framework.

Chapter 3

Spectral Method

In this chapter, the Galerkin form of the Chebyshev spectral method is presented. By using the idea of a residual, it will be shown how spectral approximation can be defined for the representation of a given function as well as for the solution of a partial differential equation (PDE). The boundary conditions will be imposed by means of the tau method. The Chebyshev polynomials will be defined and their orthogonality property examined. Lastly, the methodology will be applied to solve a simple curve-fitting example. The notation used in the formulation has been adopted from Peyret [33] and Boyd [2].

3.1 Basic Idea

Spectral methods are encompassed within the framework of the method of weighted residuals (MWR) as described in Finlayson [14]. This family of methods for solving PDEs utilize approximations defined in terms of a truncated series expansion, such that some quantity (error or residual) which should be identically zero is forced to be zero only in an approximate (mean) sense. This is done through the inner product defined by

$$(u, v)_w \equiv \int_a^b u(x)\, v(x)\, w(x)\, dx, \tag{3.1}$$

where $u(x)$ and $v(x)$ are arbitrary functions defined on $[a, b]$ and $w(x)$ is some given weight function.

3.2 Function Approximation

Assume the function $u(x)$ defined on $[a, b]$ can be approximated by a truncated series expansion

$$u(x) \approx u_N(x) = \sum_{k=0}^{N} c_k \phi_k(x), \tag{3.2}$$

where the $N+1$ basis (or trial) functions $\phi_k(x)$ are given and the series coefficients c_k must be determined. In spectral methods, the chosen basis functions are either trigonometric functions e^{ikx} (i.e. Fourier series) for spatially periodic problems or Chebyshev $T_k(x)$ and Legendre $P_k(x)$ polynomials for nonperiodic problems. In general, the trial functions are orthogonal with respect to some weight $w(x)$, such that

$$(\phi_k, \phi_l)_w = C_k \delta_{kl}, \tag{3.3}$$

where C_k = constant and δ_{kl} is the Kronecker delta symbol.

The aforementioned basis functions possess two other useful properties. First, they are easy to compute. Indeed, both trigonometric functions and polynomials fulfill this criterion. Second, they form a complete set. To satisfy this property, the basis functions must be sufficient to represent all functions in the class we are interested in with arbitrarily high accuracy.

When the series $u_N(x)$ is substituted into the PDE

$$Lu(x) = f(x), \tag{3.4}$$

where L is either the linear or nonlinear homogeneous differential operator associated with the PDE under consideration and $f(x)$ is the corresponding inhomogeneous term, the result is the residual function defined by

$$R_N(x) \equiv Lu_N(x) - f(x). \tag{3.5}$$

The residual function $R_N(x)$ is identically equal to zero for the exact solution. The difficulty lies in choosing the series coefficients c_k in such a way so as to minimize the residual function.

3.3 Method of Weighted Residuals

The MWR sets to zero the inner product

$$(R_N, \psi_j)_{w_\star} = \int_a^b R_N(x)\, \psi_j(x)\, w_\star(x)\, dx = 0, \tag{3.6}$$

where $\psi_j(x)$ are the test (or weighting) functions and the weight $w_\star(x)$ is associated with the method and basis functions. Note that $j \in J_N$ where the dimension of the discrete set J_N depends on the problem under consideration.

The choice of the test functions and of the weight defines the method. The Galerkin-type approach corresponds to the case where the test functions are the basis functions themselves and the weight $w_\star$ is the weight associated with the orthogonality of the basis functions, that is,

$$\psi_j = \phi_j \qquad \text{and} \qquad w_\star = w. \tag{3.7}$$

3.4 Boundary Conditions

The traditional Galerkin method applies when the basis functions $\phi_k(x)$ in the expansion of $u_N(x)$ satisfy the homogeneous boundary conditions of either Dirichlet, Neumann, or Robin type. In this case, $J_N = \{0, \ldots, N\}$ which furnishes $N+1$ Galerkin equations of the form (3.6) to determine the $N+1$ series coefficients c_k. If the basis functions do not satisfy the homogeneous boundary conditions, the method may be applied by first using basis recombination. However, it is usually simpler to use the tau method.

In 1938, Lanczos [23] introduced the tau method to allow the use of basis functions not satisfying the homogeneous boundary conditions. Basically, this technique replaces Galerkin

equations with boundary conditions. For instance, if there are two boundary conditions then $J_N = \{0, \ldots, N-2\}$. The omission of the Galerkin equations for $j = N-1$ and $j = N$ introduces a supplementary error, the tau error, which has given its name to the method. The reader is referred to Gottlieb and Orszag [15] and Canuto et al. [3] for further details. In brief, high order derivatives of Chebyshev (and Legendre) polynomials grow rapidly as the endpoints are approached. The mismatch between the large values of the derivatives near $x \pm 1$ and the small values near the origin can lead to poorly conditioned matrices and accumulation of roundoff error. However, the ill-conditioning of an uncombined basis is usually not a problem unless $N \sim 100$ or the PDE has third or higher derivatives.

3.5 Chebyshev Polynomials

The Chebyshev polynomial of the first kind $T_k(x)$ is the polynomial of degree k defined for $x \in [-1, 1]$ by

$$T_k(x) = \cos\left(k \cos^{-1} x\right), \tag{3.8}$$

where $k = 0, 1, 2 \ldots$, and hence $-1 \leq T_k(x) \leq 1$. Now, setting $x = \cos z$ yields

$$T_k(z) = \cos kz, \tag{3.9}$$

from which it is a simple matter to obtain the first Chebyshev polynomials

$$T_0(x) = 1, \quad T_1(x) = \cos z = x, \quad T_2(x) = \cos 2z = 2\cos^2 z - 1 = 2x^2 - 1, \ldots . \tag{3.10}$$

Alternatively, using the trigonometric identity

$$\cos(k+1)z + \cos(k-1)z = 2\cos z \cos kz \tag{3.11}$$

the following recurrence relation can be deduced

$$T_{k+1}(x) = 2xT_k(x) - T_{k-1}(x), \tag{3.12}$$

where $k \geq 1$. The polynomials $T_k(x)$ for $k \geq 2$ can be obtained from the knowledge of $T_0(x)$ and $T_1(x)$. The graph of the first few polynomials is shown in Figure 3-1.

Consequently, the recurrence relations for the first, second, and higher order derivatives of the Chebyshev polynomials can be determined by simple differentiation. For instance, the first and second derivative recurrence relations are given by

$$T'_{k+1}(x) = 2T_k(x) + 2xT'_k(x) - T'_{k-1}(x), \tag{3.13}$$

$$T''_{k+1}(x) = 4T'_k(x) + 2xT''_k(x) - T''_{k-1}(x). \tag{3.14}$$

The Chebyshev polynomials are orthogonal on $[-1, 1]$ with the weight

$$w(x) = \frac{1}{\sqrt{1-x^2}}. \tag{3.15}$$

The orthogonality property is

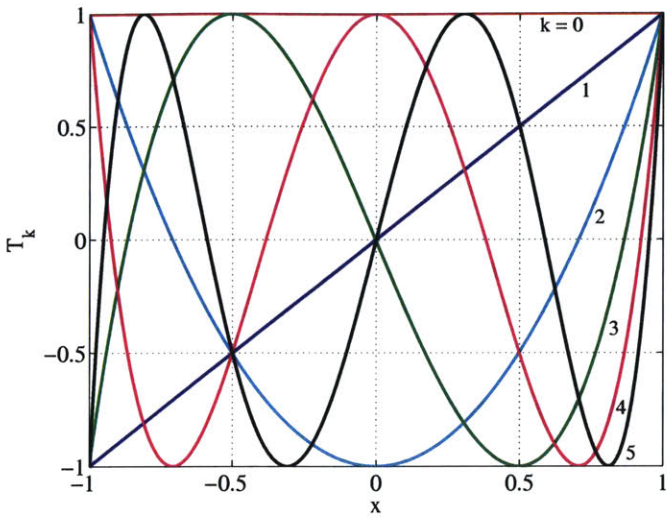

Figure 3-1: Graphs of the Chebyshev polynomials $T_k(x)$, for $k = 0, \ldots, 5$.

$$(T_k, T_l)_w = \int_{-1}^{1} T_k(x)\, T_l(x)\, w(x)\, dx = \frac{\pi}{2} C_k \delta_{kl}, \tag{3.16}$$

where C_k takes on the values

$$C_k = \begin{cases} 2 & \text{if } k = 0, \\ 1 & \text{if } k \geq 1. \end{cases} \tag{3.17}$$

3.6 Curve-Fit Example

Consider curve-fitting sets of turbulent jet profiles obtained from experiments conducted by Zhou and Wygnanski [45] using the spectral method. Once again, the data from three jet strengths $u_\infty/u_{\text{jet}} = \{0.085, 0.59, 0.38\}$ each consisting of five profiles measured at 32, 100, 200, 300, and 400 mm from the slot location were used.

The experimental jet velocity was first normalized with its edge velocity such that $U_{\text{exp}} = u_{\text{exp}}/u_e$. Next, the MATLAB piecewise cubic Hermite interpolation technique was used to approximate the profile with 181 points. The points were chosen by setting $x = -\cos\varphi$ with φ ranging from $[0, \pi]$ in increments of $\pi/180$ and then applying the transformation $\eta = (x+1)/2$ such that $\eta = y/\delta$ ranges from $[0, 1]$. The interpolated jet velocity $U_{\text{int}} = u_{\text{int}}/u_e$ is denoted $U(\eta)$ defined on $[0, 1]$ and its truncated series expansion $U_N(\eta)$ has the form

$$U_N(\eta) = \sum_{k=0}^{N} c_k \phi_k(\eta). \tag{3.18}$$

Choosing the basis functions $\phi_k(\eta)$ to be the Chebyshev polynomials $T_k(x)$ defined on $[-1, 1]$ requires a change of variable from η to x given by

$$x = 2\eta - 1. \tag{3.19}$$

The residual function $R_N(x)$ is given by

$$R_N(x) = U(x) - U_N(x) = U(x) - \sum_{k=0}^{N} c_k T_k(x). \tag{3.20}$$

Applying the MWR (Galerkin-type) gives

$$(R_N, T_j)_w = \int_{-1}^{1} R_N(x)\, T_j(x)\, w(x)\, dx = 0, \tag{3.21}$$

where the weight $w(x)$ is once again

$$w(x) = \frac{1}{\sqrt{1-x^2}}. \tag{3.22}$$

The weight can be removed with a change of variable. Setting $x = -\cos\varphi$ reduces the weighted residual statement to

$$\int_0^{\pi} R_N(\varphi)\, T_j(\varphi)\, d\varphi = 0. \tag{3.23}$$

Substituting the residual function and rearranging yields

$$\underbrace{\sum_{k=0}^{N} \left[\int_0^{\pi} T_k(\varphi)\, T_j(\varphi)\, d\varphi\right]}_{\mathbf{K}} \underbrace{c_k}_{\mathbf{c}} = \underbrace{\int_0^{\pi} U(\varphi)\, T_j(\varphi)\, d\varphi}_{\mathbf{f}}, \tag{3.24}$$

which is the simple matrix system

$$\mathbf{Kc} = \mathbf{f}. \tag{3.25}$$

The matrix $\mathbf{K}$ is known as the stiffness matrix from dynamics, $\mathbf{c}$ is the vector of unknown series coefficients, and $\mathbf{f}$ is the righthand side vector.

Before solving the above system the boundary conditions at $\eta = 1$, namely,

$$U_N(1) = 1 \qquad \text{and} \qquad U_N'(1) = 0, \tag{3.26}$$

must be imposed. For this, the tau method is implemented in which the last two Galerkin equations are replaced by the equations for the boundary conditions. Therefore, $j \in J_N$ has $J_N = \{0, \ldots, N-2\}$ where $N = 20$ in this example. The integration was performed using the trapezoidal rule with the integration points corresponding to the location of the interpolation points.

The results of this example are shown in Figures 3-2 to 3-4. Overall the approximation is fairly good especially near the edge. Near the wall the high velocity gradients cause large errors in the approximation. Applying the no-slip condition at the wall would have required increasing N dramatically. If the inner layer could somehow be resolved independently of the rest of the profile, it seems clear that only a few modes would be required to compute the outer layer. This is, in fact, the motivation for using a wall function.

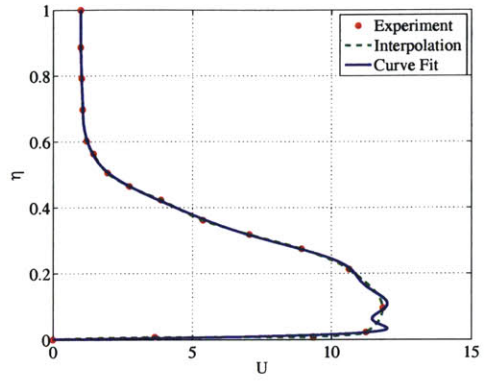

(a) 32 mm

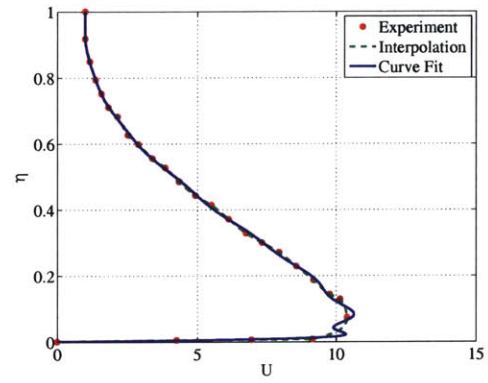

(b) 100 mm

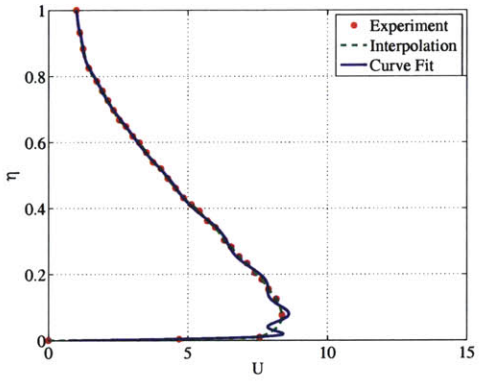

(c) 200 mm

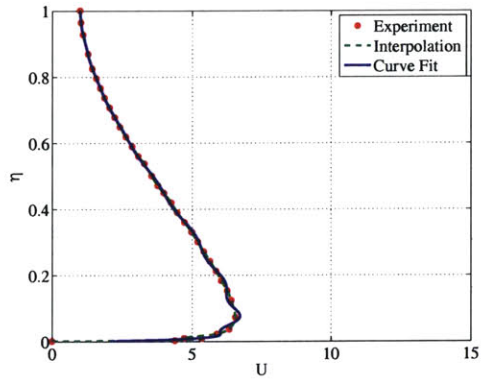

(d) 300 mm

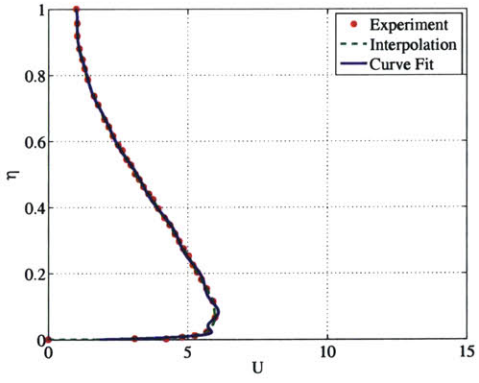

(e) 400 mm

Figure 3-2: Curve-fit results: Jet strength $u_\infty/u_{\text{jet}} = 0.085$.

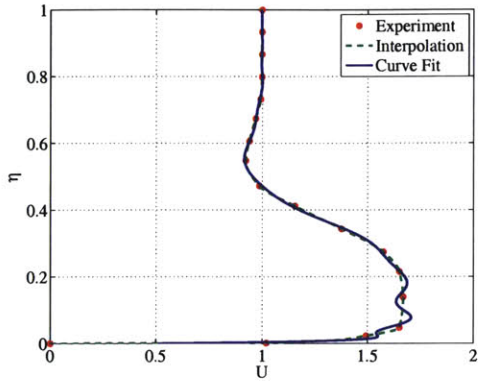

(a) 32 mm

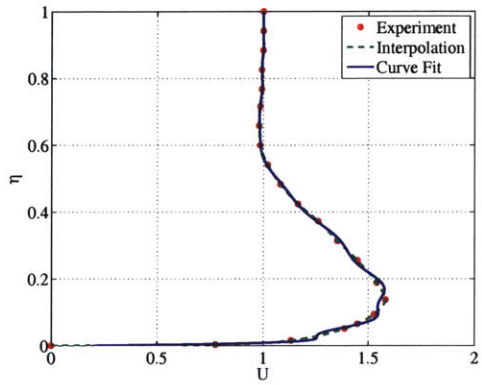

(b) 100 mm

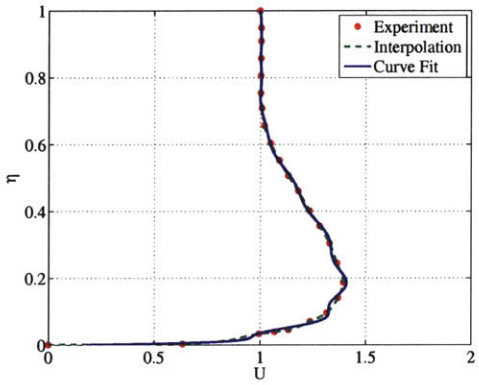

(c) 200 mm

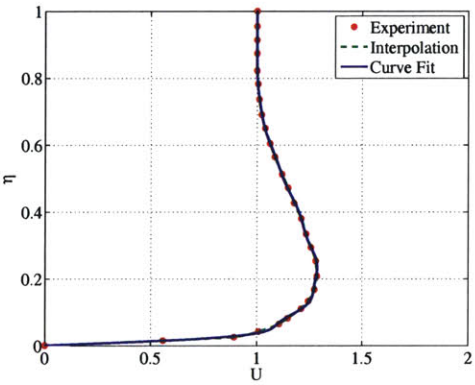

(d) 300 mm

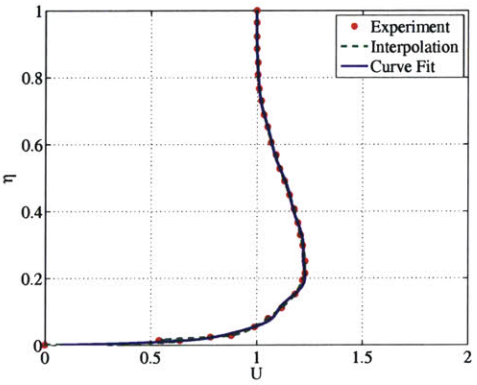

(e) 400 mm

Figure 3-3: Curve-fit results: Jet strength $u_\infty/u_{\text{jet}} = 0.59$.

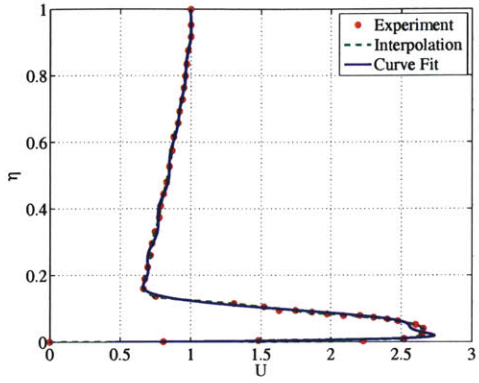

(a) 32 mm

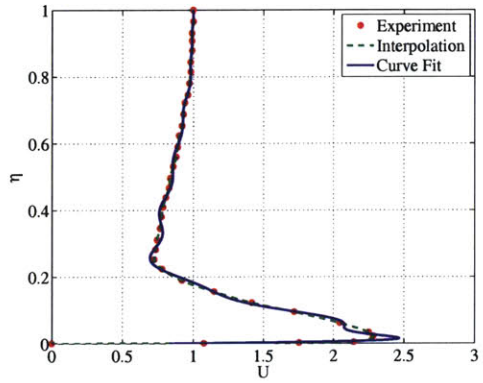

(b) 100 mm

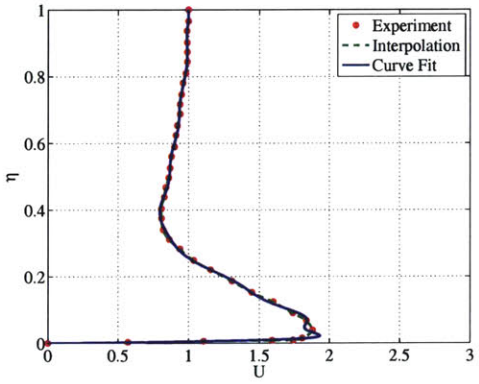

(c) 200 mm

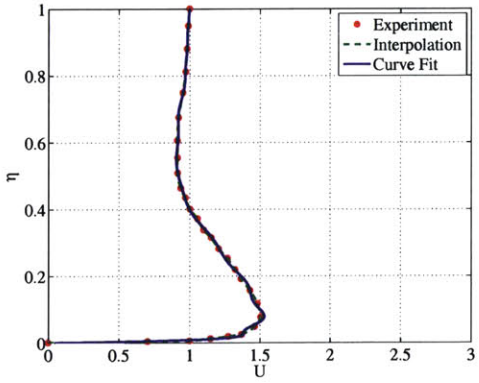

(d) 300 mm

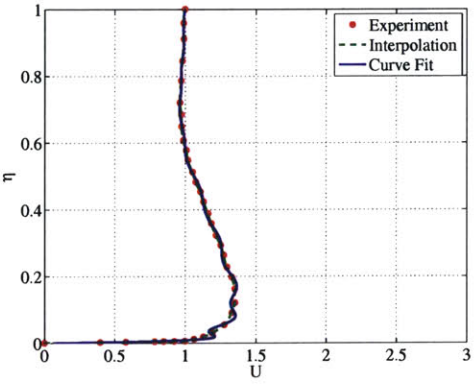

(e) 400 mm

Figure 3-4: Curve-fit results: Jet strength $u_\infty/u_{\text{jet}} = 0.38$.

Chapter 4

Laminar Flow

The spectral method is applied to solve the laminar incompressible boundary layer flow problem. The defect form of the momentum equation is derived and constitutes the partial differential equation (PDE) of interest. Truncated Chebyshev series expansions for the unknown velocities are substituted into the PDE to obtain the residual function. The weighted residual statement is formed using the Galerkin-type approach and the boundary conditions are imposed with the tau method. Additional constraints are required for the edge velocity and the boundary layer thickness. The Newton method is implemented to solve the system of nonlinear equations in an iterative fashion. The results for a flat plate with or without boundary layer flow control via vertical suction/blowing are reported. The laminar jet on a flat plate is also simulated.

4.1 Boundary Layer Equations

4.1.1 Real Viscous Flow

The 2-D, steady, incompressible continuity and x-momentum thin shear layer equations governing the real viscous flow (RVF) in the laminar regime are given by

$$\frac{\partial u}{\partial x} + \frac{\partial v}{\partial y} = 0, \tag{4.1}$$

$$\frac{\partial}{\partial x}\left(u^2\right) + \frac{\partial}{\partial y}\left(uv\right) + \frac{1}{\rho}\frac{\partial p}{\partial x} - \frac{1}{\rho}\frac{\partial \tau}{\partial y} = 0. \tag{4.2}$$

In these expressions, u and v are, respectively, the x- and y-components of the RVF velocity; ρ is the mass density; p is the static pressure and τ is the shear stress given by

$$\tau = \mu \frac{\partial u}{\partial y}, \tag{4.3}$$

where μ is the dynamic viscosity.

4.1.2 Equivalent Inviscid Flow

In analogous fashion, the 2-D, steady, incompressible continuity and x-momentum thin shear layer equations governing the equivalent inviscid flow (EIF) in the laminar regime are given by

$$\frac{\partial u_i}{\partial x} + \frac{\partial v_i}{\partial y} = 0, \tag{4.4}$$

$$\frac{\partial}{\partial x}\left(u_i^2\right) + \frac{\partial}{\partial y}\left(u_i v_i\right) + \frac{1}{\rho_i}\frac{\partial p_i}{\partial x} = 0. \tag{4.5}$$

In these expressions, the subscript i denotes the EIF condition. As such, u_i and v_i are, respectively, the x- and y-components of the EIF velocity; ρ_i is the mass density and p_i is the static pressure.

4.1.3 Defect Form of the Momentum Equation

Subtracting (4.2) from (4.5) gives

$$\frac{\partial}{\partial x}\left(u_i^2 - u^2\right) + \frac{\partial}{\partial y}\left(u_i v_i - uv\right) + \frac{1}{\rho_i}\frac{\partial p_i}{\partial x} - \frac{1}{\rho}\frac{\partial p}{\partial x} + \frac{1}{\rho}\frac{\partial \tau}{\partial y} = 0, \tag{4.6}$$

which can be simplified noting that

$$\rho = \rho_i \qquad \text{and} \qquad p\left(x, y\right) \approx p\left(x\right) = p_i\left(x\right), \tag{4.7}$$

such that

$$\frac{\partial}{\partial x}\left(u_i^2 - u^2\right) + \frac{\partial}{\partial y}\left(u_i v_i - uv\right) + \nu\frac{\partial}{\partial y}\left(\frac{\partial u}{\partial y}\right) = 0. \tag{4.8}$$

This is the defect form of the x-momentum equation. The expression for τ has already been substituted where the kinematic viscosity, ν, is the ratio of the dynamic viscosity μ to the density ρ, or

$$\nu = \frac{\mu}{\rho}. \tag{4.9}$$

4.1.4 Local Scaling Transformation

The coordinate transformation $(x, y) \rightarrow (\xi, \eta)$ is given by

$$\xi = x, \tag{4.10}$$

$$\eta = 2\frac{y}{\delta} - 1, \tag{4.11}$$

where δ is the thickness of the boundary layer. The partial derivatives transform to

$$\frac{\partial}{\partial x} = \frac{\partial}{\partial \xi} - \frac{(\eta + 1)}{\delta}\frac{d\delta}{d\xi}\frac{\partial}{\partial \eta}, \tag{4.12}$$

$$\frac{\partial}{\partial y} = \frac{2}{\delta}\frac{\partial}{\partial \eta}. \tag{4.13}$$

Applying this transformation to (4.8) gives

$$\frac{\partial}{\partial \xi}\left(u_i^2 - u^2\right) - \frac{(\eta+1)}{\delta}\frac{d\delta}{d\xi}\frac{\partial}{\partial \eta}\left(u_i^2 - u^2\right) + \frac{2}{\delta}\frac{\partial}{\partial \eta}\left(u_i v_i - uv\right) + \nu\frac{4}{\delta^2}\frac{\partial}{\partial \eta}\left(\frac{\partial u}{\partial \eta}\right) = 0, \quad (4.14)$$

which is the PDE of interest.

4.2 Series Expansions

4.2.1 Viscous Streamwise Velocity

The viscous streamwise velocity $u(\xi,\eta)$ defined on $\xi \in (0,\infty)$ and $\eta \in [-1,1]$ can be approximated by the truncated series expansion given by

$$u(\xi,\eta) \approx u_N(\xi,\eta) = u_e(\xi)\sum_{k=0}^{N} c_k(\xi)\,T_k(\eta), \quad (4.15)$$

where $u_e(\xi)$ is the edge velocity (streamwise component), $c_k(\xi)$ are the series coefficients, and the chosen basis functions $T_k(\eta)$ are the Chebyshev polynomials.

4.2.2 Viscous Normal Velocity

An expression for the viscous normal velocity $v(\xi,\eta)$ can be obtained by making use of the continuity equation (4.1). Rewriting

$$\frac{\partial v}{\partial y} = -\frac{\partial u}{\partial x}, \quad (4.16)$$

and integrating between 0 and y gives

$$\int_0^y \frac{\partial v}{\partial y}dy = -\int_0^y \frac{\partial u}{\partial x}dy, \quad (4.17a)$$

$$v(x,y) - v(x,0) = -\int_0^y \frac{\partial u}{\partial x}dy, \quad (4.17b)$$

$$v(x,y) = v_w(x) - \int_0^y \frac{\partial u}{\partial x}dy. \quad (4.17c)$$

The term $v_w(x) = v(x,0)$ is the wall velocity (or transpiration) which can be positive or negative or zero (solid wall case). Applying the coordinate transformation $(x,y) \to (\xi,\eta)$ gives

$$v(\xi,\eta) = v_w(\xi) - \frac{\delta}{2}\int_{-1}^{\eta}\left[\frac{\partial u}{\partial \xi} - \frac{(\eta+1)}{\delta}\frac{d\delta}{d\xi}\frac{\partial u}{\partial \eta}\right]d\eta, \quad (4.18)$$

which can be expanded to

$$v(\xi,\eta) = v_w(\xi) - \frac{\delta}{2}\int_{-1}^{\eta}\frac{\partial u}{\partial \xi}d\eta + \frac{1}{2}\frac{d\delta}{d\xi}\int_{-1}^{\eta}(\eta+1)\frac{\partial u}{\partial \eta}d\eta, \quad (4.19)$$

and using integration by parts on the last integral gives

$$v(\xi,\eta) = v_w(\xi) - \frac{\delta}{2}\int_{-1}^{\eta}\frac{\partial u}{\partial \xi}d\eta + \frac{1}{2}\frac{d\delta}{d\xi}\left[(\eta+1)u - \int_{-1}^{\eta} u d\eta\right], \tag{4.20}$$

where $v_w(\xi) = v(\xi,-1)$.

4.2.3 Inviscid Streamwise Velocity

The inviscid streamwise velocity $u_i(\xi,\eta)$ is nothing but the edge velocity $u_e(\xi)$, or

$$u_i(\xi,\eta) = u_i(\xi) = u_e(\xi). \tag{4.21}$$

4.2.4 Inviscid Normal Velocity

The inviscid normal velocity $v_i(\xi,\eta)$ can similarly be derived from its corresponding continuity equation (4.4). Rewriting

$$\frac{\partial v_i}{\partial y} = -\frac{\partial u_i}{\partial x}, \tag{4.22}$$

and noting that

$$u_i(x,y) = u_i(x) = u_e(x), \tag{4.23}$$

yields

$$\frac{\partial v_i}{\partial y} = -\frac{du_e}{dx}. \tag{4.24}$$

Integrating between y and δ gives

$$\int_y^{\delta}\frac{\partial v_i}{\partial y}dy = -\int_y^{\delta}\frac{du_e}{dx}dy, \tag{4.25a}$$

$$v_i(x,\delta) - v_i(x,y) = -(\delta - y)\frac{du_e}{dx}, \tag{4.25b}$$

$$v_i(x,y) = v_i(x,\delta) + (\delta - y)\frac{du_e}{dx}, \tag{4.25c}$$

where $v_i(x,\delta) = v(x,\delta) = v_e(x)$, the normal component of the edge velocity. Applying the coordinate transformation $(x,y) \rightarrow (\xi,\eta)$ gives

$$v_i(\xi,\eta) = v_i(\xi,1) + \frac{\delta}{2}(1-\eta)\frac{du_e}{dx}, \tag{4.26}$$

where $v_i(\xi,1) = v(\xi,1) = v_e(\xi)$.

4.3 Weighted Residual Statement

4.3.1 Residual Function

Substituting the expressions for u, v, u_i, and v_i into the PDE of interest (4.14) yields the residual function $R(\xi,\eta)$. It has the form

$$R(\xi,\eta) = \frac{\partial}{\partial\xi}\left(u_i^2 - u^2\right) - \frac{(\eta+1)}{\delta}\frac{d\delta}{d\xi}\frac{\partial}{\partial\eta}\left(u_i^2 - u^2\right) + \frac{2}{\delta}\frac{\partial}{\partial\eta}\left(u_i v_i - uv\right) + \nu\frac{4}{\delta^2}\frac{\partial}{\partial\eta}\left(\frac{\partial u}{\partial\eta}\right). \tag{4.27}$$

4.3.2 Galerkin Approach

Applying the MWR (Galerkin-type) gives

$$\left(R, T_j\right)_w = \int_{-1}^{1} R(\xi,\eta)\, T_j(\eta)\, w(\eta)\, d\eta = 0, \tag{4.28}$$

where the weight $w(\eta)$ is

$$w(\eta) = \frac{1}{\sqrt{1-\eta^2}}. \tag{4.29}$$

The weight can be removed with a change of variable. Setting $\eta = -\cos\varphi$ with $\varphi \in [0,\pi]$ yields

$$\int_0^{\pi} R(\xi,\varphi)\, T_j(\varphi)\, d\varphi = 0. \tag{4.30}$$

Hence, there are $N+1$ Galerkin equations $R_{G_j}(\xi)$ defined by

$$R_{G_j}(\xi) \equiv \int_0^{\pi} R(\xi,\varphi)\, T_j(\varphi)\, d\varphi = 0. \tag{4.31}$$

Unless otherwise noted, the integration will be performed using the trapezoidal rule with $\Delta\varphi = \pi/180$.

4.4 Boundary Conditions

4.4.1 Tau Method

At the edge of the boundary layer

$$u(x,\delta) = u_e(x) \qquad \text{or} \qquad u(\xi,1) = u_e(\xi), \tag{4.32}$$

whereas at the wall the no-slip condition is

$$u(x,0) = 0 \qquad \text{or} \qquad u(\xi,-1) = 0. \tag{4.33}$$

The tau method is used to impose these two boundary conditions. As such, the last two Galerkin equations are replaced by the equations for the boundary conditions denoted by

$$R_{BC_1}(x,\delta) = u(x,\delta) - u_e(x) = 0 \qquad \text{or} \qquad R_{BC_1}(\xi,1) = u(\xi,1) - u_e(\xi) = 0, \tag{4.34}$$

and

$$R_{BC_2}(x,0) = u(x,0) = 0 \qquad \text{or} \qquad R_{BC_2}(\xi,-1) = u(\xi,-1) = 0. \tag{4.35}$$

Therefore, $j \in J_N$ has $J_N = \{0,\ldots,N-2\}$.

4.5 Additional Constraints

4.5.1 Boundary Layer Thickness

The height of the η interval in y space is simply δ, which is best set to match, or slightly exceed, the physical boundary layer thickness. Here, this δ is constrained with the residual

$$R_\delta\left(x,\frac{\delta}{2}\right) = u\left(x,\frac{\delta}{2}\right) - 0.95u_e(x) = 0, \tag{4.36}$$

or equivalently,

$$R_\delta(\xi,0) = u(\xi,0) - 0.95u_e(\xi) = 0. \tag{4.37}$$

The precise form of R_δ is not critical, as long as δ is larger than the physical boundary layer thickness.

4.5.2 Edge Velocity

The edge velocity is simply specified

$$R_{u_e}(x) = u_e(x) - u_{e_{\text{spec}}}(x) = 0, \tag{4.38}$$

or equivalently,

$$R_{u_e}(\xi) = u_e(\xi) - u_{e_{\text{spec}}}(\xi) = 0. \tag{4.39}$$

4.6 Solver

4.6.1 Newton Method

The system of nonlinear equations is solved by means of the Newton iteration scheme. For a vector of equations $\mathbf{F}$ and a vector of unknowns $\mathbf{U}$ such that

$$\mathbf{F}(\mathbf{U}) = 0, \tag{4.40}$$

the solution procedure at some iteration level n is

$$\mathbf{F}\left(\mathbf{U}^{n+1}\right) \equiv \mathbf{F}\left(\mathbf{U}^n + \delta\mathbf{U}^n\right) \approx \mathbf{F}\left(\mathbf{U}^n\right) + \left[\frac{\partial\mathbf{F}}{\partial\mathbf{U}}\right]^n \delta\mathbf{U}^n = 0, \tag{4.41a}$$

$$\delta\mathbf{U}^n = -\left[\frac{\partial\mathbf{F}}{\partial\mathbf{U}}\right]^{n^{-1}} \mathbf{F}\left(\mathbf{U}^n\right), \tag{4.41b}$$

$$\mathbf{U}^{n+1} = \mathbf{U}^n + \delta\mathbf{U}^n. \tag{4.41c}$$

The term $[\partial\mathbf{F}/\partial\mathbf{U}]^n$ is the Jacobian matrix whose (i,j) entry is the partial derivative of the i'th equation in $\mathbf{F}$ with respect to the j'th variable in $\mathbf{U}$, evaluated at $\mathbf{U}^n$. The algorithm

converges quadratically for fairly accurate $\mathbf{U}^n$. Solving the linear system in (4.41b) is the most expensive step.

In the present application the vector of equations $\mathbf{F}$ will consist of the $N-1$ Galerkin equations R_G, the two boundary conditions, R_{BC_1} and R_{BC_2}, as well as the two constraint equations, R_δ and R_{u_e}. The vector of unknowns $\mathbf{U}$ will contain the $N+1$ series coefficients c_k, the boundary layer thickness δ, and the edge velocity u_e. These vectors are given by

$$\mathbf{F} = \begin{bmatrix} R_{G_0} \\ \vdots \\ R_{G_{N-2}} \\ R_{BC_1} \\ R_{BC_2} \\ R_\delta \\ R_{u_e} \end{bmatrix} \quad \text{and} \quad \mathbf{U} = \begin{bmatrix} c_0 \\ \vdots \\ c_{N-2} \\ c_{N-1} \\ c_N \\ \delta \\ u_e \end{bmatrix}. \tag{4.42}$$

The Jacobian matrix $[\partial\mathbf{F}/\partial\mathbf{U}]$ will be an $(N+3)\times(N+3)$ matrix of the form

$$\left[\frac{\partial \mathbf{F}}{\partial \mathbf{U}}\right] = \begin{bmatrix} \frac{\partial R_{G_0}}{\partial c_0} & \cdots & \frac{\partial R_{G_0}}{\partial c_{N-2}} & \frac{\partial R_{G_0}}{\partial c_{N-1}} & \frac{\partial R_{G_0}}{\partial c_N} & \frac{\partial R_{G_0}}{\partial \delta} & \frac{\partial R_{G_0}}{\partial u_e} \\ \vdots & \ddots & \vdots & \vdots & \vdots & \vdots & \vdots \\ \frac{\partial R_{G_{N-2}}}{\partial c_0} & \cdots & \frac{\partial R_{G_{N-2}}}{\partial c_{N-2}} & \frac{\partial R_{G_{N-2}}}{\partial c_{N-1}} & \frac{\partial R_{G_{N-2}}}{\partial c_N} & \frac{\partial R_{G_{N-2}}}{\partial \delta} & \frac{\partial R_{G_{N-2}}}{\partial u_e} \\ \frac{\partial R_{BC_1}}{\partial c_0} & \cdots & \frac{\partial R_{BC_1}}{\partial c_{N-2}} & \frac{\partial R_{BC_1}}{\partial c_{N-1}} & \frac{\partial R_{BC_1}}{\partial c_N} & \frac{\partial R_{BC_1}}{\partial \delta} & \frac{\partial R_{BC_1}}{\partial u_e} \\ \frac{\partial R_{BC_2}}{\partial c_0} & \cdots & \frac{\partial R_{BC_2}}{\partial c_{N-2}} & \frac{\partial R_{BC_2}}{\partial c_{N-1}} & \frac{\partial R_{BC_2}}{\partial c_N} & \frac{\partial R_{BC_2}}{\partial \delta} & \frac{\partial R_{BC_2}}{\partial u_e} \\ \frac{\partial R_\delta}{\partial c_0} & \cdots & \frac{\partial R_\delta}{\partial c_{N-2}} & \frac{\partial R_\delta}{\partial c_{N-1}} & \frac{\partial R_\delta}{\partial c_N} & \frac{\partial R_\delta}{\partial \delta} & \frac{\partial R_\delta}{\partial u_e} \\ \frac{\partial R_{u_e}}{\partial c_0} & \cdots & \frac{\partial R_{u_e}}{\partial c_{N-2}} & \frac{\partial R_{u_e}}{\partial c_{N-1}} & \frac{\partial R_{u_e}}{\partial c_N} & \frac{\partial R_{u_e}}{\partial \delta} & \frac{\partial R_{u_e}}{\partial u_e} \end{bmatrix}. \tag{4.43}$$

4.7 Discretization

4.7.1 Similarity Station

The flow is assumed to be similar from $\xi > 0$ until the first grid point. Setting the first grid point to station 2 and anywhere before this point as station 1 (except at the origin), the similarity condition

$$\left.\frac{u}{u_i}\right|_1 = \left.\frac{u}{u_i}\right|_2, \tag{4.44}$$

must hold true at any given η value. In addition,

$$u_i = C_i\xi^{\beta_u}, \qquad m = C_m\xi^{\beta_m}, \qquad \text{and} \qquad \delta = C_\delta\xi^{\beta_\delta}, \tag{4.45}$$

where C_i, C_m, and C_δ are constants and β_u, β_m, and β_δ are constant in ξ, such that

$$\beta_u \equiv \frac{\xi}{u_e}\frac{du_e}{d\xi}, \qquad \beta_m \equiv \frac{\xi}{m}\frac{dm}{d\xi}, \qquad \text{and} \qquad \beta_\delta \equiv \frac{\xi}{\delta}\frac{d\delta}{d\xi}. \tag{4.46}$$

Noting that $m \equiv u_e\delta$ then the relationships between the various β's are

$$\beta_m = \frac{1+\beta_u}{2} \qquad \text{and} \qquad \beta_\delta = \frac{1-\beta_u}{2}. \tag{4.47}$$

Therefore, at station 2 it is possible to deduce

$$\frac{du_i}{d\xi} = \beta_u \frac{u_i}{\xi}, \tag{4.48}$$

$$\frac{du_i^2}{d\xi} = 2\beta_u \frac{u_i^2}{\xi}, \tag{4.49}$$

$$\frac{\partial u}{\partial \xi} = \beta_u \frac{u}{\xi}, \tag{4.50}$$

$$\frac{\partial u^2}{\partial \xi} = 2\beta_u \frac{u^2}{\xi}, \tag{4.51}$$

$$\frac{d\delta}{d\xi} = \left(\frac{1-\beta_u}{2}\right)\frac{\delta}{\xi}. \tag{4.52}$$

4.7.2 Logarithmic Differencing

Outside the similarity station, logarithmic differencing is employed to get

$$\frac{du_i}{d\xi} = \frac{u_i}{\xi}\frac{d(\ln u_i)}{d(\ln \xi)} \approx \frac{u_i}{\xi}\frac{\Delta(\ln u_i)}{\Delta(\ln \xi)} = \frac{u_{i_2}}{\xi_2}\frac{\ln u_{i_2} - \ln u_{i_1}}{\ln \xi_2 - \ln \xi_1} = \frac{u_{i_2}}{\xi_2}\frac{\ln\left(\frac{u_{i_2}}{u_{i_1}}\right)}{\ln\left(\frac{\xi_2}{\xi_1}\right)}, \tag{4.53}$$

$$\frac{du_i^2}{d\xi} = 2\frac{u_{i_2}^2}{\xi_2}\frac{\ln\left(\frac{u_{i_2}}{u_{i_1}}\right)}{\ln\left(\frac{\xi_2}{\xi_1}\right)}, \tag{4.54}$$

$$\frac{\partial u}{\partial \xi} = \frac{\partial}{\partial \xi}(U u_i) = u_i\frac{\partial U}{\partial \xi} + U\frac{du_i}{d\xi} \approx u_{i_2}\frac{U_2 - U_1}{\xi_2 - \xi_1} + U_2\frac{u_{i_2}}{\xi_2}\frac{\ln\left(\frac{u_{i_2}}{u_{i_1}}\right)}{\ln\left(\frac{\xi_2}{\xi_1}\right)}, \tag{4.55}$$

$$\frac{\partial u^2}{\partial \xi} = \frac{\partial}{\partial \xi}\left(U^2 u_i^2\right) = u_i^2\frac{\partial U^2}{\partial \xi} + U^2\frac{du_i^2}{d\xi} \approx u_{i_2}^2\frac{U_2^2 - U_1^2}{\xi_2 - \xi_1} + U_2^2 2\frac{u_{i_2}^2}{\xi_2}\frac{\ln\left(\frac{u_{i_2}}{u_{i_1}}\right)}{\ln\left(\frac{\xi_2}{\xi_1}\right)}, \tag{4.56}$$

$$\frac{d\delta}{d\xi} = \frac{\delta}{\xi}\frac{d(\ln \delta)}{d(\ln \xi)} \approx \frac{\delta}{\xi}\frac{\Delta(\ln \delta)}{\Delta(\ln \xi)} = \frac{\delta_2}{\xi_2}\frac{\ln \delta_2 - \ln \delta_1}{\ln \xi_2 - \ln \xi_1} = \frac{\delta_2}{\xi_2}\frac{\ln\left(\frac{\delta_2}{\delta_1}\right)}{\ln\left(\frac{\xi_2}{\xi_1}\right)}. \tag{4.57}$$

The difference forms above are exact in laminar similar flows with negligible curvature effects even if $\Delta\xi/\xi$ is not small. Hence, logarithmic differencing greatly reduces the streamwise resolution requirements near the leading edge where $\xi \to 0$. For small $\Delta\xi/\xi$ these are equivalent to Backward-Euler to first order in $\Delta\xi/\xi$.

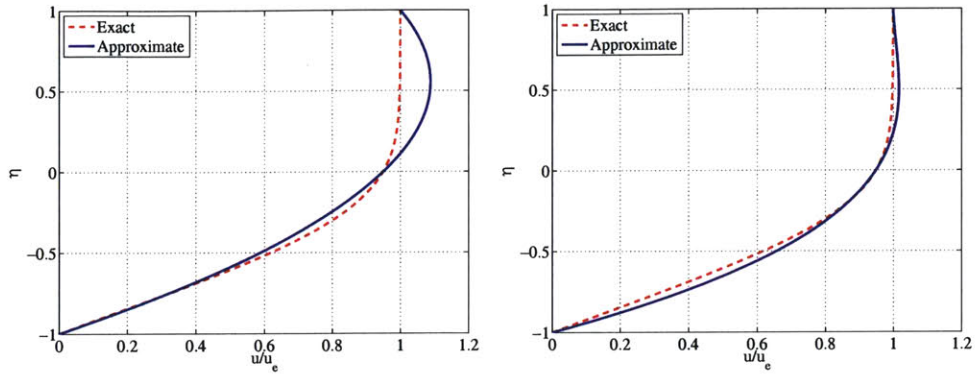

(a) $N = 2$ (b) $N = 3$

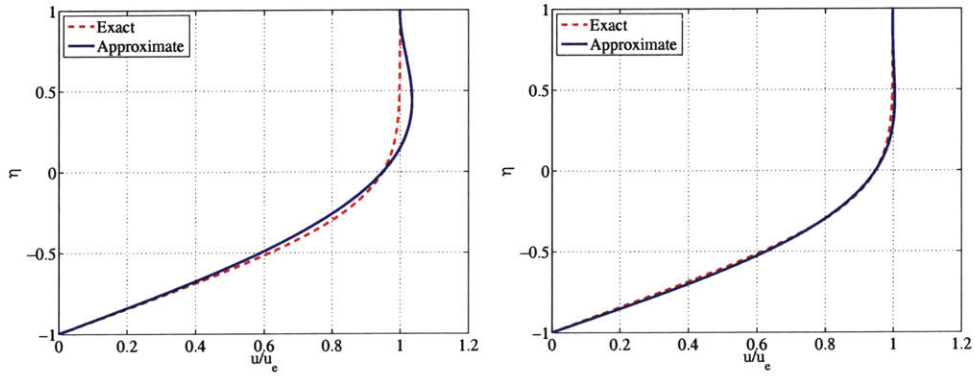

(c) $N = 4$ (d) $N = 5$

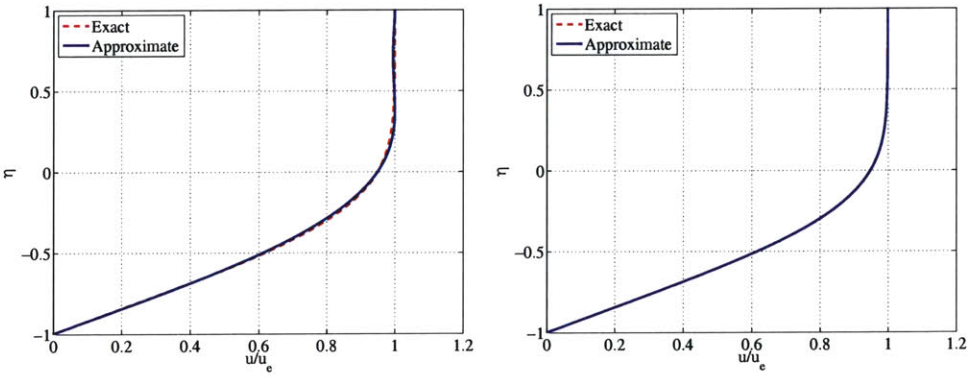

(e) $N = 6$ (f) $N = 10$

Figure 4-1: Laminar flat plate: Modal convergence for u/u_e.

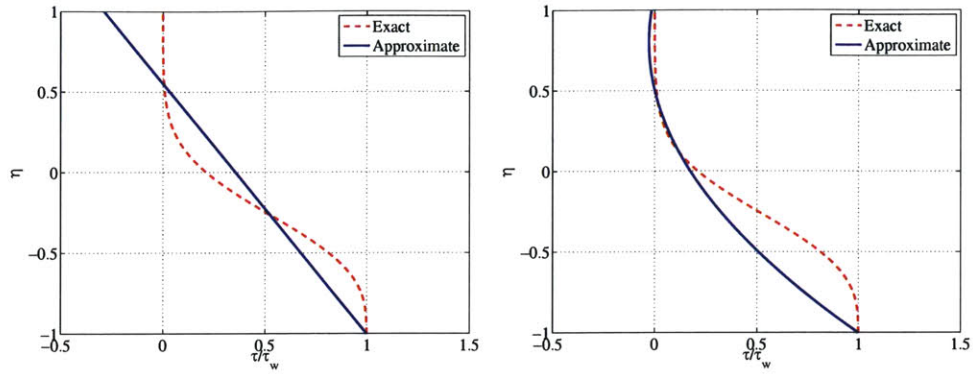

(a) $N = 2$ (b) $N = 3$

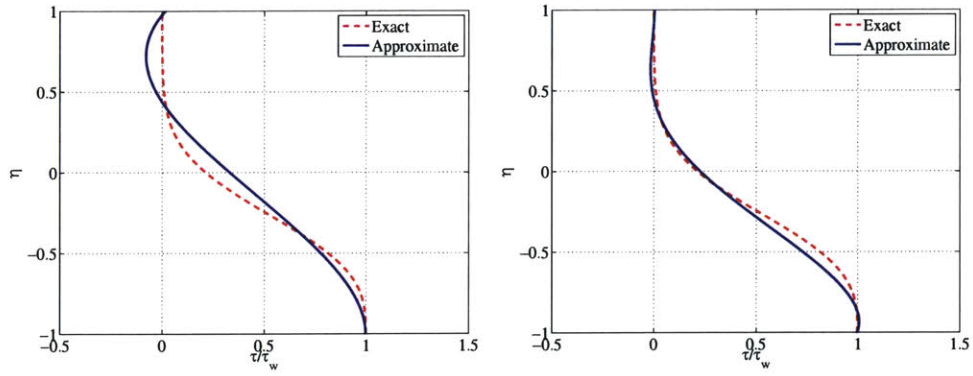

(c) $N = 4$ (d) $N = 5$

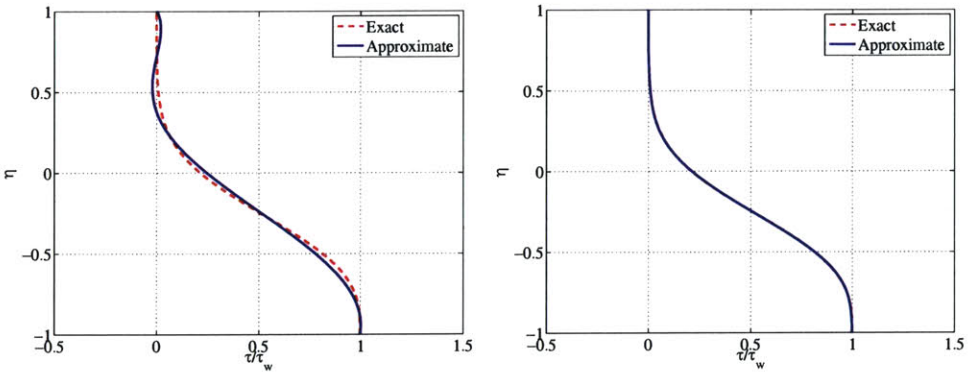

(e) $N = 6$ (f) $N = 10$

Figure 4-2: Laminar flat plate: Modal convergence for τ/τ_w.

4.8 Results

4.8.1 Flat Plate ($\beta_u = 0$)

The quintessential problem in viscous boundary layer flow is that of flow over a flat plate. For the laminar case, Prandtl's first student, H. Blasius [1], derived an ordinary differential equation (ODE) governing the flow based on similarity arguments. The nonlinear Blasius equation (see White [41]) has never yielded to exact analytic solution. Rosenhead [35] has chronicled proposed solution methods to this equation in his text. With the advent of the computer, the equation can now be solved numerically.

Table 4.1: Falkner-Skan and Spectral Method solutions to flat plate flow.

Solution	β_u	$F''(0) \equiv \frac{1}{2} C_f \sqrt{\mathrm{Re}_x}$	$\delta^*_{\mathrm{FS}} \equiv \delta^* \sqrt{u_e/\nu x}$	$\theta_{\mathrm{FS}} \equiv \theta \sqrt{u_e/\nu x}$	H
Falkner-Skan	0	0.33206	1.72080	0.66412	2.591
Spectral Method	0	0.33211	1.72086	0.66401	2.592

In this work, the Falkner-Skan family of boundary layer similarity solutions (see Appendix A), of which the flow over a flat plate is but one special case, will be used for comparison purposes. Table 4.1 shows the close agreement in results between the Falkner-Skan solution and the spectral method. Note that $x = \xi$ in the table. For the spectral method, $N = 10$ based on the modal convergence plots shown in Figures 4-1 and 4-2. Figure 4-3 illustrates the exponential convergence rate (geometric-type) of the series coefficients on a log-linear plot (see Boyd [2]). The flow was solved for $N = 180$ to show the appearance of a Roundoff Plateau (see Boyd [2]) starting at $N \approx 45$. Detailed plots for the spectral solution to the flat plate problem as well as some of the more interesting wedge flows are listed in Appendix A.

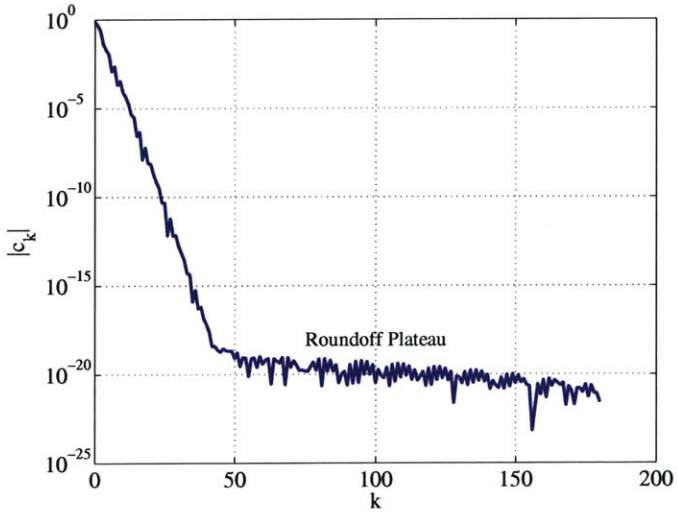

Figure 4-3: Laminar flat plate: $|c_k|$ vs. k.

4.8.2 Flat Plate with Wall Suction or Blowing - Similar Flow

A porous flat plate with nonzero wall velocity, $v_w \ll u_e$, either positive (blowing) or negative (suction), has many applications: mass transfer, drying, ablation, transpiration cooling, and boundary layer control. There is no streamwise wall velocity, u_w, so the no-slip condition is still enforced. For similarity, $v_w(x)$ must vary as $x^{-1/2}$ (see White [41]). The results will differ according to the suction-blowing parameter, v_w^*, defined by

$$v_w^* \equiv \frac{v_w}{u_e}\sqrt{\mathrm{Re}_x}, \tag{4.58}$$

where Re_x is the Reynolds number based on x given by

$$\mathrm{Re}_x = \frac{u_e x}{\nu}. \tag{4.59}$$

Figure 4-4 depicts how strongly the velocity profiles are affected by v_w^*. These are plotted with respect to $\eta^* \equiv y\sqrt{\frac{u_e}{2x\nu}}$ where $x = \xi$ and $y = (\eta + 1)\,\delta/2$. In all cases, $N = 30$. Suction thins the boundary layer and increases the slope at the wall. The suction profiles have strong negative curvature, are very stable, and delay transition to turbulence. Conversely, blowing thickens the boundary layer and makes the profile S-shaped, less stable, and prone to transition to turbulence. The boundary layer is blown off at $v_w^* = 0.619$.

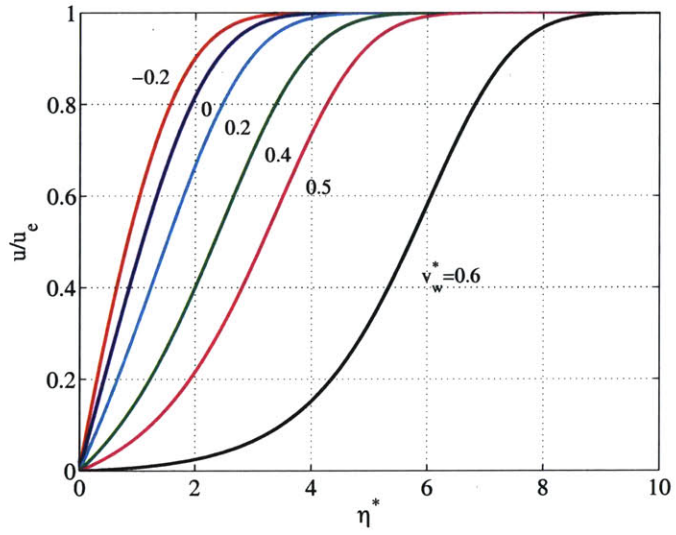

Figure 4-4: Velocity profiles for a flat plate with wall suction or blowing.

4.8.3 Flat Plate with Uniform Wall Suction - Nonsimilar Flow

Iglisch [18] studied the flow past a flat plate with uniform suction (i.e. $v_w = \text{constant} < 0$). Wall suction is an effective means of delaying transition to turbulence, at the expense of increasing the drag. The resulting flow is nonsimilar. The velocity profiles change from the laminar flat plate profile at the leading edge to the asymptotic exponential profile given by

$$u = u_e \left(1 - e^{y v_w/\nu}\right), \tag{4.60}$$

far downstream (see White [41]). The asymptotic condition is reached when $(-v_w/u_e)\sqrt{\mathrm{Re}_x} \approx 2.0$. For a suction rate of $(-v_w/u_e) = 0.01$ with $u_e = 1$ m/s, this corresponds to a distance of $x = 0.6$ m.

For the spectral solution to this problem, $N = 10$. The velocity and shear stress profiles shown in Figure 4-5 exhibit the theoretical exponential shapes, as expected. The detailed spectral solution to this problem shown in Figures 4-6 and 4-7 clearly indicates the asymptotic behavior. Once again, $\xi = x$ and $\eta = 2y/\delta - 1$.

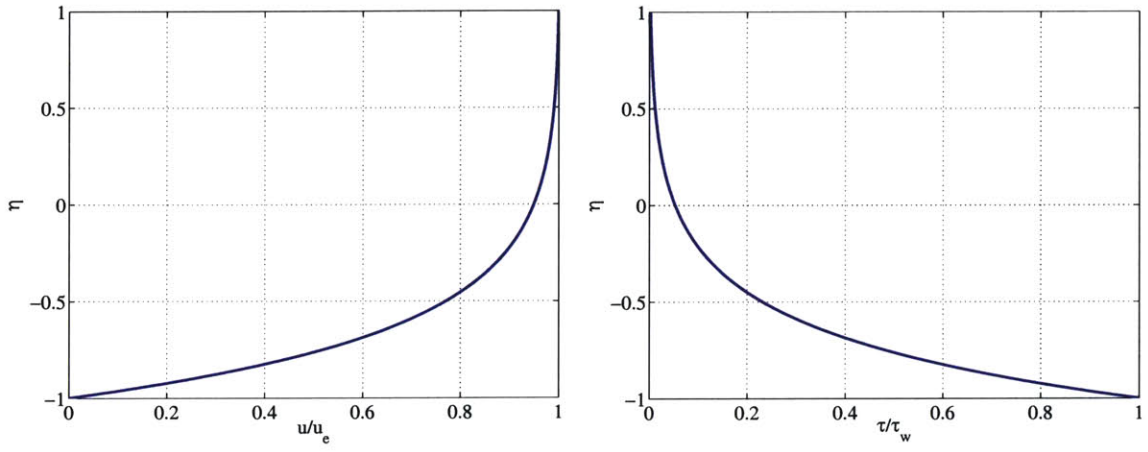

(a) Velocity Profile

(b) Shear Stress Profile

Figure 4-5: Uniform suction: u/u_e and τ/τ_w profiles at $\xi = 1$ m.

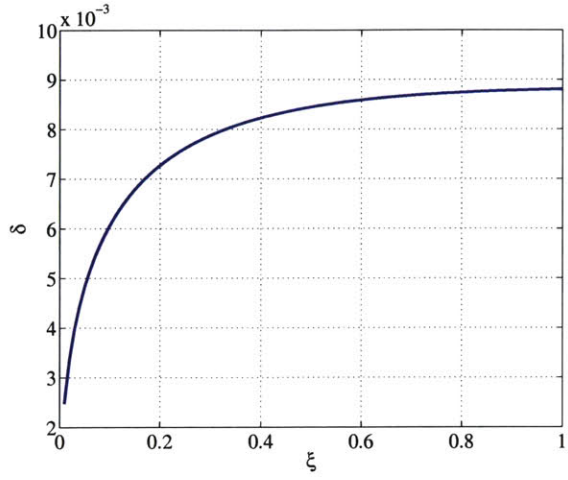

(a) Boundary Layer Thickness

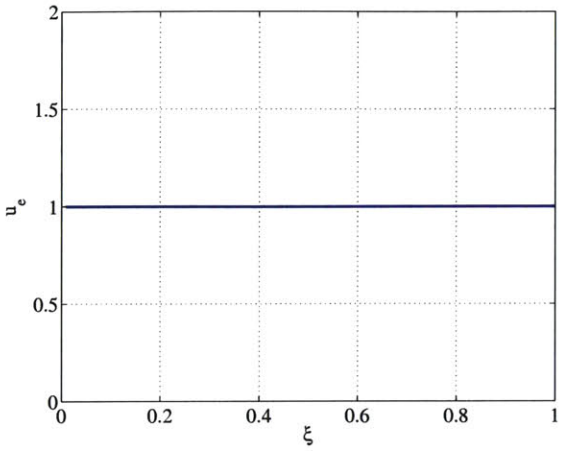

(b) Edge Velocity

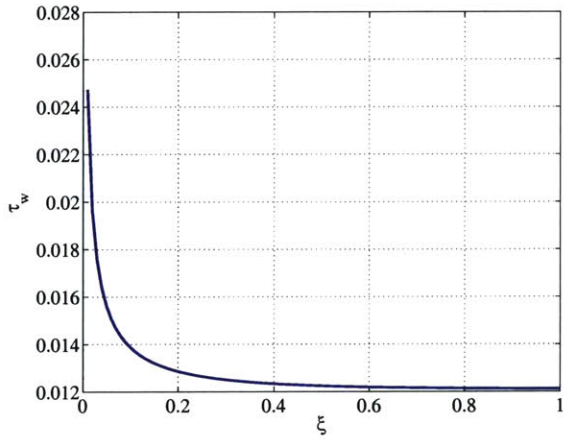

(c) Wall Shear Stress

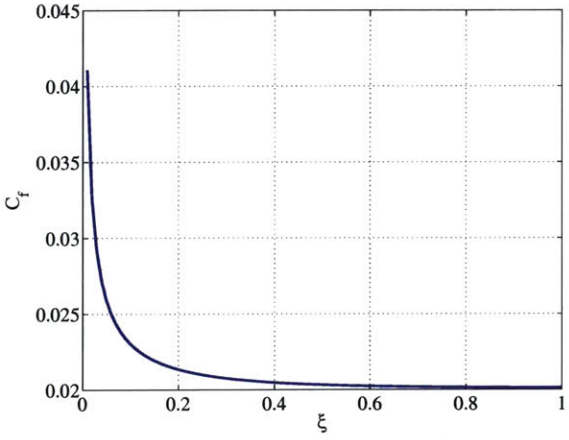

(d) Skin Friction Coefficient

Figure 4-6: Uniform suction: δ, u_e, τ_w, and C_f vs. ξ.

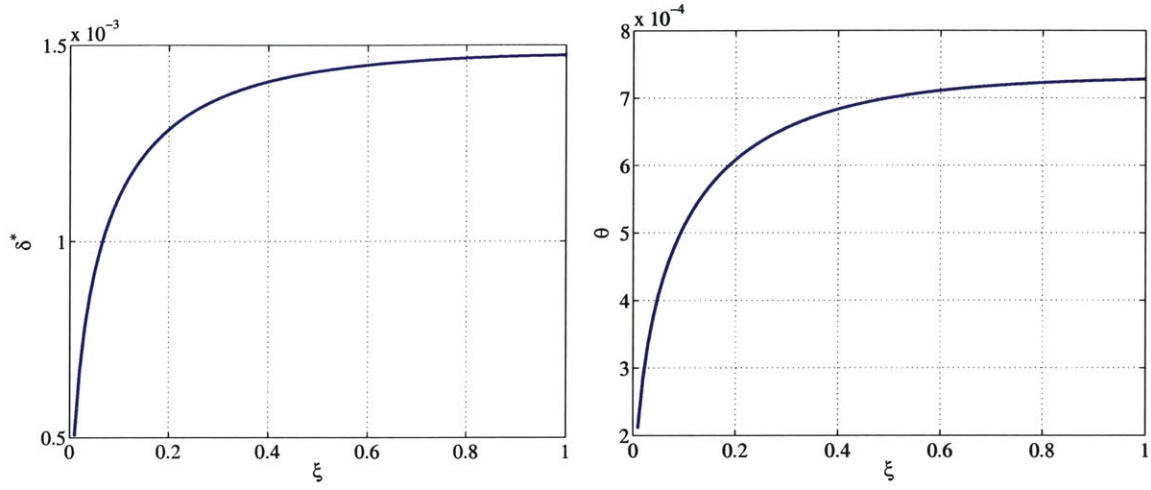

(a) Displacement Thickness

(b) Momentum Thickness

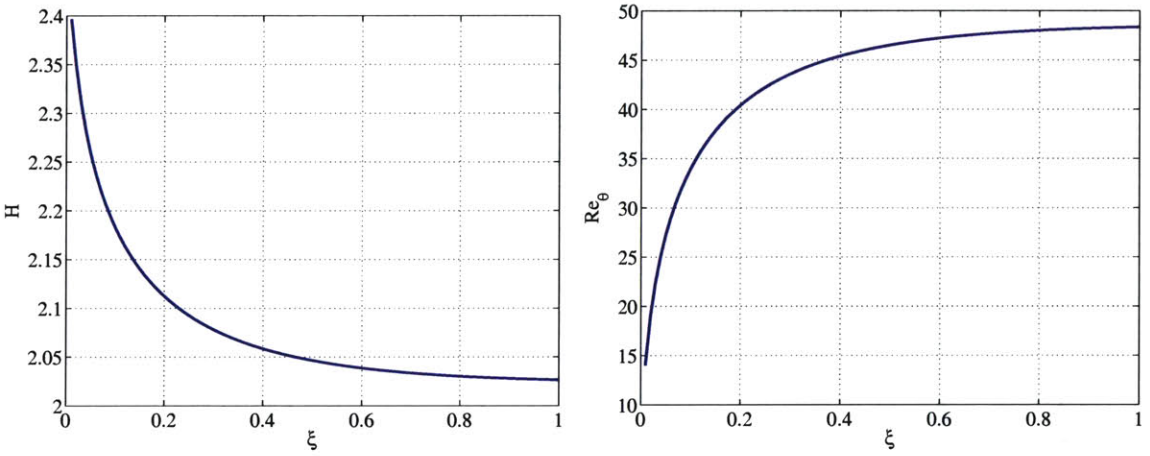

(c) Shape Parameter

(d) Reynolds Number

Figure 4-7: Uniform suction: δ^*, θ, H, and Re_θ vs. ξ.

4.8.4 Laminar Jet

Fluid injection is an effective means of flow control. Consider a flat plate with an inclined slot of length l and width b such that $\sin\alpha = b/l$, where α is the slot angle (see Figure 4-8). For $b = 0.005$ m and $l = 0.05$ m the angle $\alpha \approx 5.74°$. Utilizing a jet strength of $u_\infty/u_{\text{jet}} = 0.38$, with the velocity profile inside the slot modeled as the Poiseuille parabola, the velocity and shear stress profiles are shown in Figure 4-9 where $\eta = 2y/\delta - 1$. The flow evolution is depicted in Figures 4-10 and 4-11 where $\xi = x$. The slot is located at $\xi = 0.65$ m and $N = 30$. The most striking feature out of all these plots is how δ^* and θ become strongly negative demonstrating the fact that the jet causes an excess of mass and momentum in the boundary layer.

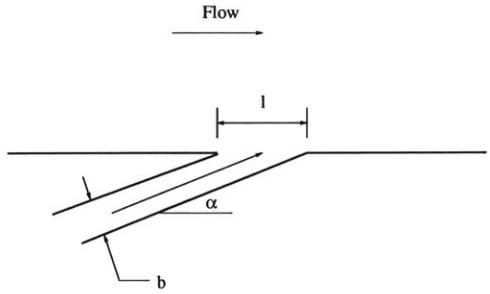

Figure 4-8: Slot geometry.

This case also points out some of the difficulties in treating the blowing problem with traditional integral boundary layer methods. Such methods are typically parameterized by $H \equiv \delta^*/\theta$, which can no longer be used when θ goes through zero downstream of the jet. The closure relations which depend on H and Re_θ cannot be used since H not only blows up but is non-unique. The Reynolds number based on θ is negative whenever $\theta < 0$ so it also cannot be used. Suction problems have no such difficulties.

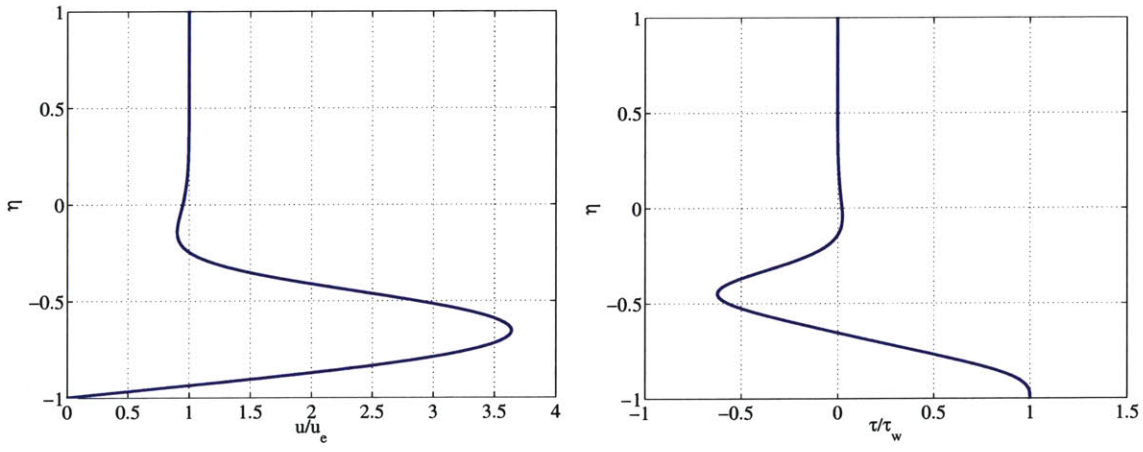

(a) Velocity Profile

(b) Shear Stress Profile

Figure 4-9: Laminar jet: u/u_e and τ/τ_w profiles at $\xi = 1$ m.

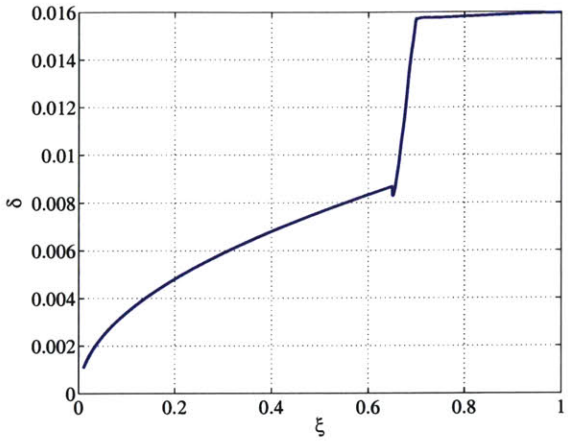

(a) Boundary Layer Thickness

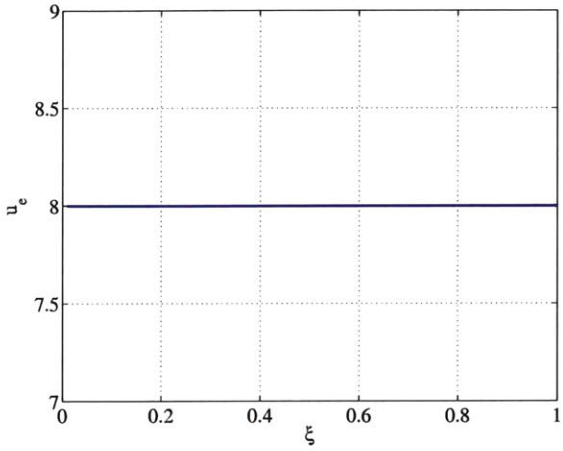

(b) Edge Velocity

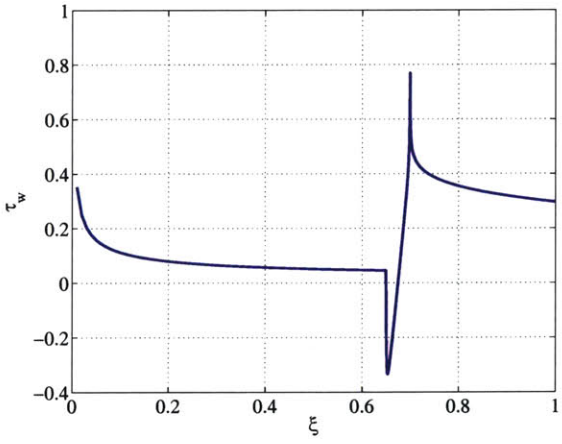

(c) Wall Shear Stress

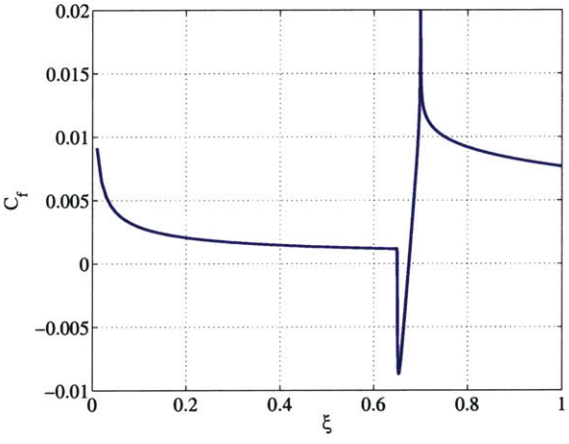

(d) Skin Friction Coefficient

Figure 4-10: Laminar jet: δ, u_e, τ_w, and C_f vs. ξ.

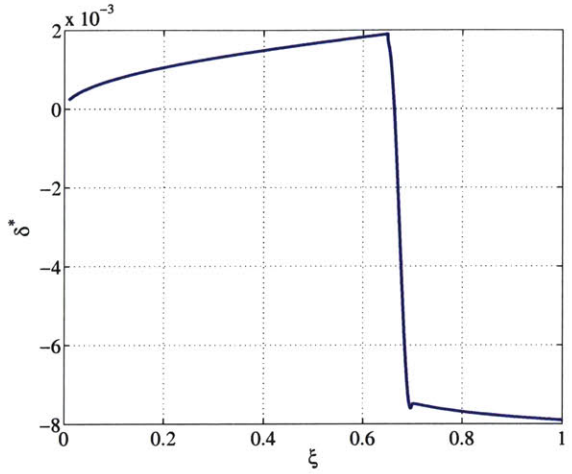

(a) Displacement Thickness

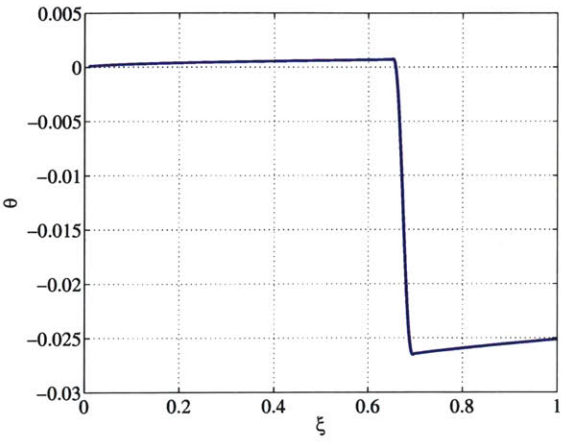

(b) Momentum Thickness

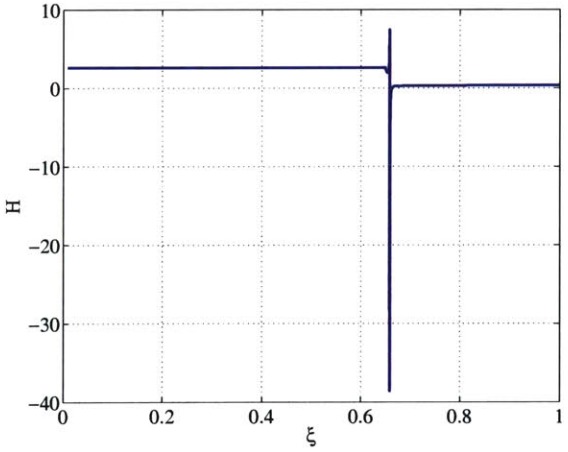

(c) Shape Parameter

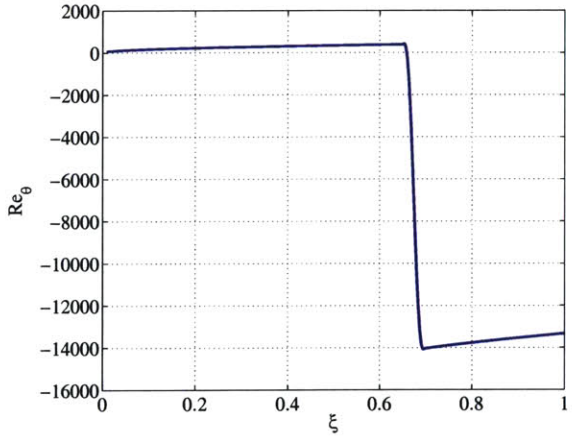

(d) Reynolds Number

Figure 4-11: Laminar jet: δ^*, θ, H, and Re_θ vs. ξ.

Chapter 5

Turbulent Flow

The primary complication in solving the turbulent incompressible boundary layer flow problem is the modeling of the Reynolds stress term in the momentum equation. The spectral method applied to turbulent flow is analogous to the formulation for laminar flow outlined in Chapter 4. The eddy viscosity is modeled using an algebraic turbulence model and the results for the flat plate case are reported. A wall function consistent with the inner layer eddy viscosity model is introduced into the approximation of the streamwise velocity and the flat plate problem is solved once more. An order of magnitude reduction in modes is observed — a major computational advantage. The results for vertical suction/blowing on a flat plate with or without the incorporation of a wall function are reported. The turbulent jet on a flat plate is also simulated.

5.1 Boundary Layer Equations

5.1.1 Real Viscous Flow

The 2-D, steady, incompressible Reynolds-averaged continuity and x-momentum thin shear layer equations governing the real viscous flow (RVF) in the turbulent regime are given by

$$\frac{\partial u}{\partial x} + \frac{\partial v}{\partial y} = 0, \tag{5.1}$$

$$\frac{\partial}{\partial x}\left(u^2\right) + \frac{\partial}{\partial y}\left(uv\right) + \frac{1}{\rho}\frac{\partial p}{\partial x} - \frac{1}{\rho}\frac{\partial \tau}{\partial y} = 0. \tag{5.2}$$

In these expressions, u and v are, respectively, the x- and y-components of the RVF velocity; ρ is the mass density; p is the static pressure and τ is the shear stress given by

$$\tau = \mu\frac{\partial u}{\partial y} - \rho\overline{u'v'}, \tag{5.3}$$

where μ is the dynamic viscosity and $-\rho\overline{u'v'}$ is the turbulent shear (or Reynolds stress).

5.1.2 Equivalent Inviscid Flow

In analogous fashion, the 2-D, steady, incompressible Reynolds-averaged continuity and x-momentum thin shear layer equations governing the equivalent inviscid flow (EIF) in the turbulent regime are given by

$$\frac{\partial u_i}{\partial x} + \frac{\partial v_i}{\partial y} = 0, \tag{5.4}$$

$$\frac{\partial}{\partial x}\left(u_i^2\right) + \frac{\partial}{\partial y}\left(u_i v_i\right) + \frac{1}{\rho_i}\frac{\partial p_i}{\partial x} = 0. \tag{5.5}$$

In these expressions, the subscript i denotes the EIF condition. As such, u_i and v_i are, respectively, the x- and y-components of the EIF velocity; ρ_i is the mass density and p_i is the static pressure.

5.1.3 Defect Form of the Momentum Equation

Subtracting (5.2) from (5.5) gives

$$\frac{\partial}{\partial x}\left(u_i^2 - u^2\right) + \frac{\partial}{\partial y}\left(u_i v_i - uv\right) + \frac{1}{\rho_i}\frac{\partial p_i}{\partial x} - \frac{1}{\rho}\frac{\partial p}{\partial x} + \frac{1}{\rho}\frac{\partial \tau}{\partial y} = 0, \tag{5.6}$$

which can be simplified noting that

$$\rho = \rho_i \qquad \text{and} \qquad p\left(x, y\right) \approx p\left(x\right) = p_i\left(x\right), \tag{5.7}$$

such that

$$\frac{\partial}{\partial x}\left(u_i^2 - u^2\right) + \frac{\partial}{\partial y}\left(u_i v_i - uv\right) + \frac{\partial}{\partial y}\left[\left(\nu + \nu_t\right)\frac{\partial u}{\partial y}\right] = 0. \tag{5.8}$$

This is the defect form of the x-momentum equation. The expression for τ has already been substituted where the kinematic viscosity, ν, is the ratio of the dynamic viscosity μ to the density ρ, or

$$\nu = \frac{\mu}{\rho}. \tag{5.9}$$

The turbulent shear $-\rho\overline{u'v'}$ is replaced by

$$-\rho\overline{u'v'} = \mu_t \frac{\partial u}{\partial y}, \tag{5.10}$$

where μ_t is the so-called eddy viscosity. This follows the modeling assumption first made by J. Boussinesq in 1877. The eddy viscosity μ_t has the same dimensions as μ but it is not a fluid property. It varies with the flow conditions and the geometry of the problem (i.e. it depends on the turbulent eddies). The term ν_t which appears in the defect form of the x-momentum equation is also referred to as the eddy viscosity but it is given by

$$\nu_t = \frac{\mu_t}{\rho}. \tag{5.11}$$

5.1.4 Local Scaling Transformation

Applying the coordinate transformation $(x, y) \rightarrow (\xi, \eta)$ described in Section 4.1.4 to (5.8) gives

$$\frac{\partial}{\partial \xi}\left(u_i^2 - u^2\right) - \frac{(\eta+1)}{\delta}\frac{d\delta}{d\xi}\frac{\partial}{\partial \eta}\left(u_i^2 - u^2\right) + \frac{2}{\delta}\frac{\partial}{\partial \eta}\left(u_i v_i - uv\right) + \frac{4}{\delta^2}\frac{\partial}{\partial \eta}\left[\left(\nu + \nu_t\right)\frac{\partial u}{\partial \eta}\right] = 0, \quad (5.12)$$

which is the PDE of interest.

5.2 Series Expansions

5.2.1 Viscous Streamwise Velocity

The viscous streamwise velocity $u(\xi, \eta)$ defined on $\xi \in (0, \infty)$ and $\eta \in [-1, 1]$ can be approximated by the truncated series expansion given by

$$u(\xi, \eta) \approx u_N(\xi, \eta) = u_e(\xi) \sum_{k=0}^{N} c_k(\xi) T_k(\eta), \quad (5.13)$$

where $u_e(\xi)$ is the edge velocity (streamwise component), $c_k(\xi)$ are the series coefficients, and the chosen basis functions $T_k(\eta)$ are the Chebyshev polynomials.

5.2.2 Viscous Normal Velocity

An expression for the viscous normal velocity $v(\xi, \eta)$ can be obtained by making use of the continuity equation (5.1). The derivation is identical to Section 4.2.2 such that

$$v(\xi, \eta) = v_w(\xi) - \frac{\delta}{2}\int_{-1}^{\eta} \frac{\partial u}{\partial \xi} d\eta + \frac{1}{2}\frac{d\delta}{d\xi}\left[(\eta+1)u - \int_{-1}^{\eta} u d\eta\right], \quad (5.14)$$

where $v_w(\xi) = v(\xi, -1)$ is the wall velocity (or transpiration) which can be positive or negative or zero (solid wall case).

5.2.3 Inviscid Streamwise Velocity

The inviscid streamwise velocity $u_i(\xi, \eta)$ is nothing but the edge velocity $u_e(\xi)$, or

$$u_i(\xi, \eta) = u_i(\xi) = u_e(\xi). \quad (5.15)$$

5.2.4 Inviscid Normal Velocity

The inviscid normal velocity $v_i(\xi, \eta)$ can similarly be derived from its corresponding continuity equation (5.4). Referring to Section 4.2.4 gives

$$v_i(\xi, \eta) = v_i(\xi, 1) + \frac{\delta}{2}(1 - \eta)\frac{du_e}{dx}, \quad (5.16)$$

where $v_i(\xi, 1) = v(\xi, 1) = v_e(\xi)$, the normal component of the edge velocity.

5.3 Eddy Viscosity Model

5.3.1 Inner Layer

The inner layer eddy viscosity model ν_{t_i} is taken from Spalding [39], such that

$$\nu_{t_i} = \nu\kappa e^{-\kappa B}\left[e^{\kappa u_+} - 1 - \kappa u_+ - \frac{(\kappa u_+)^2}{2}\right]. \tag{5.17}$$

The inner-law variable u_+ is defined by

$$u_+ \equiv \frac{u}{u_\tau}, \tag{5.18}$$

where the friction velocity u_τ is given by

$$u_\tau = s\left[\frac{|\tau_w|}{\rho}\right]^{1/2} \tag{5.19}$$

with $s = \text{sgn}(\tau_w)$. The constants

$$\kappa = 0.41 \qquad \text{and} \qquad B = 5.0 \tag{5.20}$$

are taken from Coles and Hirst [7].

5.3.2 Outer Layer

The outer layer eddy viscosity model ν_{t_o} is based on the formulation by Clauser [5], such that

$$\nu_{t_o} = 0.016 u_e \delta^*, \tag{5.21}$$

where u_e is the edge velocity, and δ^* is the displacement thickness defined by

$$\delta^* \equiv \int_0^\delta \left(1 - \frac{u}{u_e}\right) dy = \frac{\delta}{2}\int_{-1}^1 \left(1 - \frac{u}{u_e}\right) d\eta. \tag{5.22}$$

5.3.3 Blending Model

The models for the inner and outer layers are combined into one composite formula for the eddy viscosity ν_t given by

$$\nu_t = \left(\frac{1}{\frac{1}{\nu_{t_i}^a} + \frac{1}{\nu_{t_o}^a}}\right)^{1/a} = \left[\frac{1}{1+\zeta^a}\right]^{1/a} \nu_{t_i}, \tag{5.23}$$

where $\zeta = \nu_{t_i}/\nu_{t_o}$ and $a = 4$. Blending ensures that the derivatives are continuous at the interface between the two layers as shown in Figure 5-1. In the inner layer, the eddy viscosity reduces to the linear relation

$$\nu_t \approx \kappa u_\tau y, \tag{5.24}$$

except in the viscous sublayer where damping reduces ν_t to a cubic function of y. In the outer layer, ν_t is tens or even hundreds of times greater than the molecular viscosity, depending on the local Reynolds number. A turbulent shear layer has a high outer and low inner effective viscosity which is why turbulent velocity profiles are so steep at the wall and so flat further out.

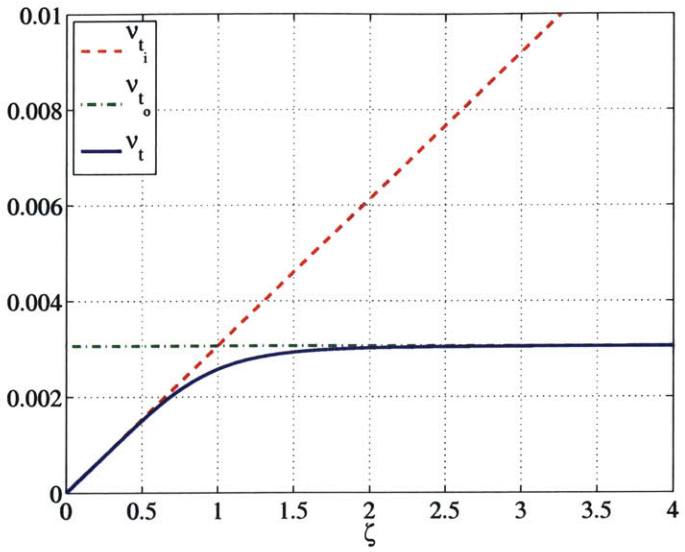

Figure 5-1: Eddy viscosity blending model.

5.4 Weighted Residual Statement

5.4.1 Residual Function

Substituting the expressions for u, v, u_i, v_i, and ν_t into the PDE of interest (5.12) yields the residual function $R(\xi, \eta)$. It has the form

$$\begin{aligned} R(\xi,\eta) = & \frac{\partial}{\partial \xi}\left(u_i^2 - u^2\right) - \frac{(\eta+1)}{\delta}\frac{d\delta}{d\xi}\frac{\partial}{\partial \eta}\left(u_i^2 - u^2\right) \\ & + \frac{2}{\delta}\frac{\partial}{\partial \eta}\left(u_i v_i - uv\right) + \frac{4}{\delta^2}\frac{\partial}{\partial \eta}\left[\left(\nu + \nu_t\right)\frac{\partial u}{\partial \eta}\right]. \end{aligned} \tag{5.25}$$

5.4.2 Galerkin Approach

Applying the MWR (Galerkin-type) gives

$$\left(R, T_j\right)_w = \int_{-1}^{1} R(\xi,\eta)\, T_j(\eta)\, w(\eta)\, d\eta = 0, \tag{5.26}$$

where the weight $w(\eta)$ is chosen to be unity

$$w(\eta) = 1. \tag{5.27}$$

Utilizing the orthogonality weight associated with the Chebyshev polynomials tends to cause the nonlinear system to be more ill-conditioned. Therefore, the weighted residual statement is

$$\int_{-1}^{1} R(\xi,\eta)\, T_j(\eta)\, d\eta = 0. \tag{5.28}$$

Hence, there are $N+1$ Galerkin equations $R_{G_j}(\xi)$ defined by

$$R_{G_j}(\xi) \equiv \int_{-1}^{1} R(\xi,\eta)\, T_j(\eta)\, d\eta = 0. \tag{5.29}$$

Unless otherwise noted, the integration will be performed using the trapezoidal rule. The integration points are chosen using $\eta = -\cos\varphi$ with φ ranging from $[0,\pi]$ in increments of $\pi/180$.

5.5 Boundary Conditions

5.5.1 Tau Method

The tau method is used to impose the same two boundary conditions as in Section 4.4.1. As such, the last two Galerkin equations are replaced by the equations for the boundary conditions denoted by

$$R_{BC_1}(\xi,1) = u(\xi,1) - u_e(\xi) = 0, \tag{5.30}$$

and

$$R_{BC_2}(\xi,-1) = u(\xi,-1) = 0. \tag{5.31}$$

Therefore, $j \in J_N$ has $J_N = \{0,\ldots,N-2\}$.

5.6 Additional Constraints

5.6.1 Boundary Layer Thickness

Referring to Section 4.5.1, the R_δ constraint is

$$R_\delta(\xi,0) = u(\xi,0) - 0.95u_e(\xi) = 0. \tag{5.32}$$

5.6.2 Edge Velocity

Referring to Section 4.5.2, the R_{u_e} constraint is

$$R_{u_e}(\xi) = u_e(\xi) - u_{e_{\text{spec}}}(\xi) = 0. \tag{5.33}$$

5.7 Solver

5.7.1 Newton Method

The system of nonlinear equations is solved by means of the Newton iteration scheme as described in Section 4.6.1.

In the present application the vector of equations $\mathbf{F}$ will consist of the $N-1$ Galerkin equations R_G, the two boundary conditions, R_{BC_1} and R_{BC_2}, as well as the two constraint equations, R_δ and R_{u_e}. The vector of unknowns $\mathbf{U}$ will contain the $N+1$ series coefficients c_k, the boundary layer thickness δ, and the edge velocity u_e. These vectors are given by

$$\mathbf{F} = \begin{bmatrix} R_{G_0} \\ \vdots \\ R_{G_{N-2}} \\ R_{BC_1} \\ R_{BC_2} \\ R_\delta \\ R_{u_e} \end{bmatrix} \quad \text{and} \quad \mathbf{U} = \begin{bmatrix} c_0 \\ \vdots \\ c_{N-2} \\ c_{N-1} \\ c_N \\ \delta \\ u_e \end{bmatrix}. \tag{5.34}$$

The Jacobian matrix $[\partial \mathbf{F}/\partial \mathbf{U}]$ will be an $(N+3) \times (N+3)$ matrix of the form

$$\left[\frac{\partial \mathbf{F}}{\partial \mathbf{U}}\right] = \begin{bmatrix} \frac{\partial R_{G_0}}{\partial c_0} & \cdots & \frac{\partial R_{G_0}}{\partial c_{N-2}} & \frac{\partial R_{G_0}}{\partial c_{N-1}} & \frac{\partial R_{G_0}}{\partial c_N} & \frac{\partial R_{G_0}}{\partial \delta} & \frac{\partial R_{G_0}}{\partial u_e} \\ \vdots & \ddots & \vdots & \vdots & \vdots & \vdots & \vdots \\ \frac{\partial R_{G_{N-2}}}{\partial c_0} & \cdots & \frac{\partial R_{G_{N-2}}}{\partial c_{N-2}} & \frac{\partial R_{G_{N-2}}}{\partial c_{N-1}} & \frac{\partial R_{G_{N-2}}}{\partial c_N} & \frac{\partial R_{G_{N-2}}}{\partial \delta} & \frac{\partial R_{G_{N-2}}}{\partial u_e} \\ \frac{\partial R_{BC_1}}{\partial c_0} & \cdots & \frac{\partial R_{BC_1}}{\partial c_{N-2}} & \frac{\partial R_{BC_1}}{\partial c_{N-1}} & \frac{\partial R_{BC_1}}{\partial c_N} & \frac{\partial R_{BC_1}}{\partial \delta} & \frac{\partial R_{BC_1}}{\partial u_e} \\ \frac{\partial R_{BC_2}}{\partial c_0} & \cdots & \frac{\partial R_{BC_2}}{\partial c_{N-2}} & \frac{\partial R_{BC_2}}{\partial c_{N-1}} & \frac{\partial R_{BC_2}}{\partial c_N} & \frac{\partial R_{BC_2}}{\partial \delta} & \frac{\partial R_{BC_2}}{\partial u_e} \\ \frac{\partial R_\delta}{\partial c_0} & \cdots & \frac{\partial R_\delta}{\partial c_{N-2}} & \frac{\partial R_\delta}{\partial c_{N-1}} & \frac{\partial R_\delta}{\partial c_N} & \frac{\partial R_\delta}{\partial \delta} & \frac{\partial R_\delta}{\partial u_e} \\ \frac{\partial R_{u_e}}{\partial c_0} & \cdots & \frac{\partial R_{u_e}}{\partial c_{N-2}} & \frac{\partial R_{u_e}}{\partial c_{N-1}} & \frac{\partial R_{u_e}}{\partial c_N} & \frac{\partial R_{u_e}}{\partial \delta} & \frac{\partial R_{u_e}}{\partial u_e} \end{bmatrix}. \tag{5.35}$$

5.8 Discretization

5.8.1 Similarity Station

The flow is assumed to be similar from $\xi > 0$ until the first grid point. Setting the first grid point to station 2 and anywhere before this point as station 1 (except at the origin), the required conditions for similarity are listed in Section 4.7.1. Therefore, at station 2 it is possible to deduce

$$\frac{du_i}{d\xi} = \beta_u \frac{u_i}{\xi}, \tag{5.36}$$

$$\frac{du_i^2}{d\xi} = 2\beta_u \frac{u_i^2}{\xi}, \tag{5.37}$$

$$\frac{\partial u}{\partial \xi} = \beta_u \frac{u}{\xi}, \tag{5.38}$$

$$\frac{\partial u^2}{\partial \xi} = 2\beta_u \frac{u^2}{\xi}, \tag{5.39}$$

$$\frac{d\delta}{d\xi} = \left(\frac{1-\beta_u}{2}\right)\frac{\delta}{\xi}. \tag{5.40}$$

5.8.2 Logarithmic Differencing

Outside the similarity station, logarithmic differencing is employed to get

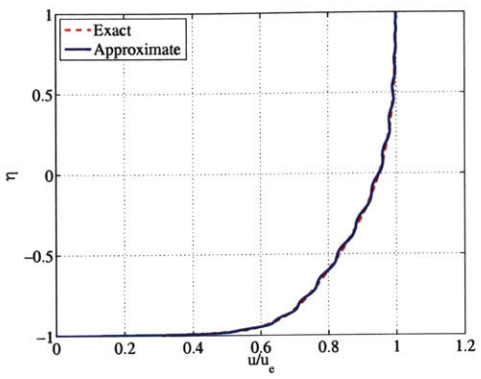

(a) $N = 30$

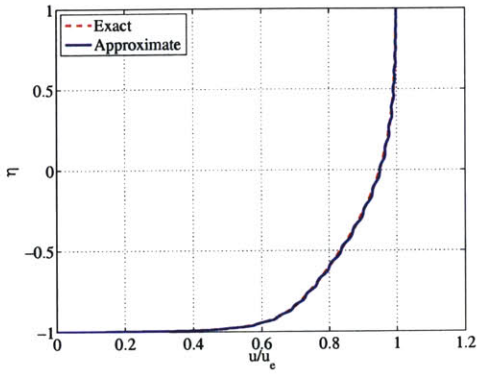

(b) $N = 50$

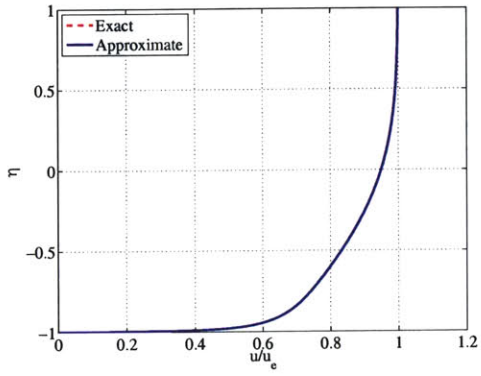

(c) $N = 100$

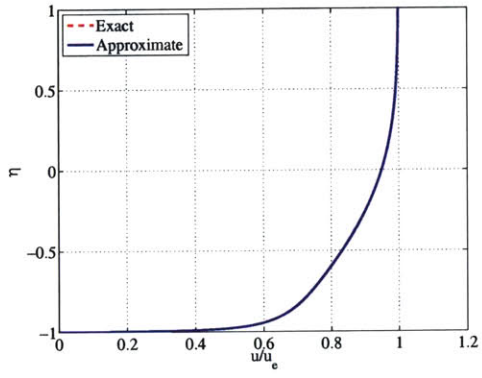

(d) $N = 120$

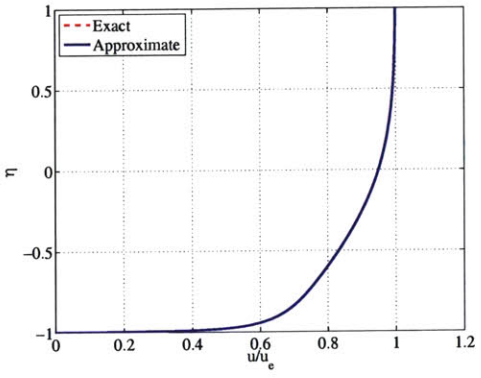

(e) $N = 150$

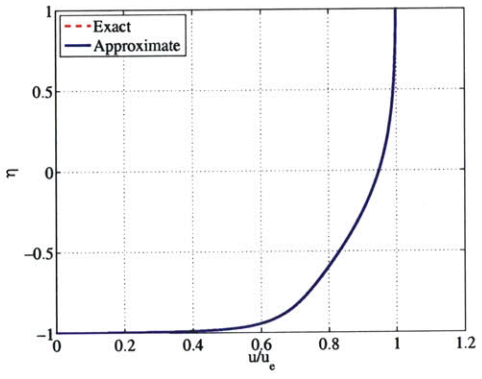

(f) $N = 180$

Figure 5-2: Turbulent flat plate: Modal convergence for u/u_e at $\xi = 1$ m.

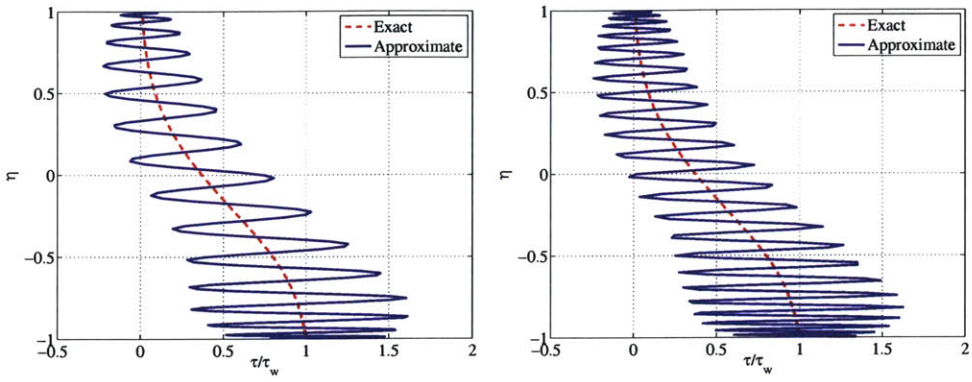

(a) $N = 30$ (b) $N = 50$

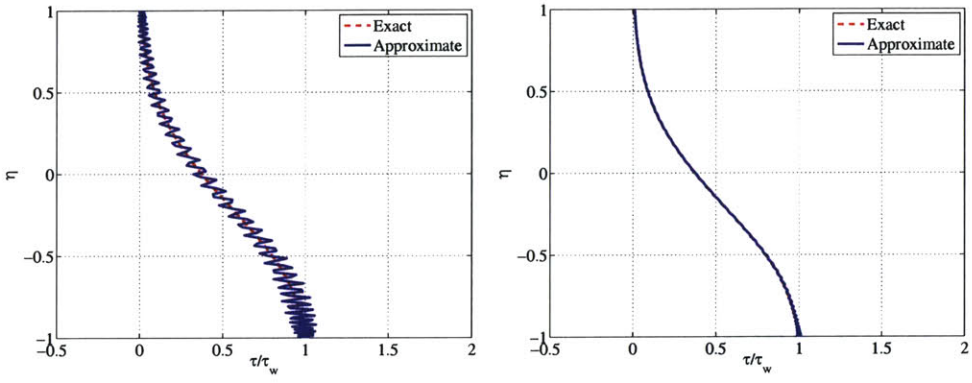

(c) $N = 100$ (d) $N = 120$

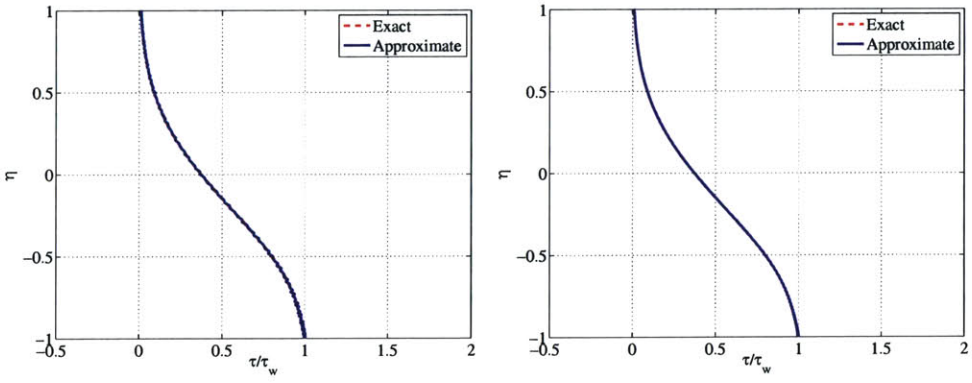

(e) $N = 150$ (f) $N = 180$

Figure 5-3: Turbulent flat plate: Modal convergence for τ/τ_w at $\xi = 1$ m.

$$\frac{du_i}{d\xi} = \frac{u_i}{\xi}\frac{d(\ln u_i)}{d(\ln \xi)} \approx \frac{u_i}{\xi}\frac{\Delta(\ln u_i)}{\Delta(\ln \xi)} = \frac{u_{i_2}}{\xi_2}\frac{\ln u_{i_2} - \ln u_{i_1}}{\ln \xi_2 - \ln \xi_1} = \frac{u_{i_2}}{\xi_2}\frac{\ln\left(\frac{u_{i_2}}{u_{i_1}}\right)}{\ln\left(\frac{\xi_2}{\xi_1}\right)}, \tag{5.41}$$

$$\frac{du_i^2}{d\xi} = 2\frac{u_{i_2}^2}{\xi_2}\frac{\ln\left(\frac{u_{i_2}}{u_{i_1}}\right)}{\ln\left(\frac{\xi_2}{\xi_1}\right)}, \tag{5.42}$$

$$\frac{\partial u}{\partial \xi} = \frac{\partial}{\partial \xi}(U u_i) = u_i\frac{\partial U}{\partial \xi} + U\frac{du_i}{d\xi} \approx u_{i_2}\frac{U_2 - U_1}{\xi_2 - \xi_1} + U_2\frac{u_{i_2}}{\xi_2}\frac{\ln\left(\frac{u_{i_2}}{u_{i_1}}\right)}{\ln\left(\frac{\xi_2}{\xi_1}\right)}, \tag{5.43}$$

$$\frac{\partial u^2}{\partial \xi} = \frac{\partial}{\partial \xi}\left(U^2 u_i^2\right) = u_i^2\frac{\partial U^2}{\partial \xi} + U^2\frac{du_i^2}{d\xi} \approx u_{i_2}^2\frac{U_2^2 - U_1^2}{\xi_2 - \xi_1} + U_2^2 2\frac{u_{i_2}^2}{\xi_2}\frac{\ln\left(\frac{u_{i_2}}{u_{i_1}}\right)}{\ln\left(\frac{\xi_2}{\xi_1}\right)}, \tag{5.44}$$

$$\frac{d\delta}{d\xi} = \frac{\delta}{\xi}\frac{d(\ln \delta)}{d(\ln \xi)} \approx \frac{\delta}{\xi}\frac{\Delta(\ln \delta)}{\Delta(\ln \xi)} = \frac{\delta_2}{\xi_2}\frac{\ln \delta_2 - \ln \delta_1}{\ln \xi_2 - \ln \xi_1} = \frac{\delta_2}{\xi_2}\frac{\ln\left(\frac{\delta_2}{\delta_1}\right)}{\ln\left(\frac{\xi_2}{\xi_1}\right)}. \tag{5.45}$$

Section 4.7.2 describes the advantages of using this form of differencing over other methods.

5.9 Flat Plate

5.9.1 Detailed Plots

The spectral solution to turbulent flow over a flat plate was computed. In this case, $N = 180$ based on the modal convergence plots shown in Figures 5-2 and 5-3 at $\xi = 1$ m. The two-layer structure of the turbulent boundary layer is clearly evident from the velocity profile. The shear stress does not quite go to zero at the edge since the eddy viscosity has a nonzero value in the outer layer. Detailed plots for the flat plate solution are shown in Figures 5-4 and 5-5. The transition location is where the flow first exceeds $\mathrm{Re}_\xi = 500000$. Figure 5-6 illustrates the convergence rate of the series coefficients on a log-linear plot at $\xi = 1$ m. This plot is typical of coefficients which oscillate with N (see Boyd [2]). However, the convergence is not exponential primarily due to a lack of smoothness for u rather than integration error. Recall that the integration points were chosen using $\eta = -\cos\varphi$ with φ ranging from $[0, \pi]$ in increments of $\pi/180$. For smaller increments, i.e. $\pi/360$ and $\pi/1800$, the graph of $|c_k|$ vs. k at $\xi = 1$ m changes very little.

5.9.2 Velocity Comparison

The velocity profile obtained from the spectral method was compared to an accurate representation constructed from Spalding's law of the wall [39] and Coles' law of the wake [6]. The details of the construction now follow.

The inner-law variables u_+ and y_+ are defined by

$$u_+ \equiv \frac{u}{u_\tau} \qquad \text{and} \qquad y_+ \equiv \frac{y}{l_\tau}, \tag{5.46}$$

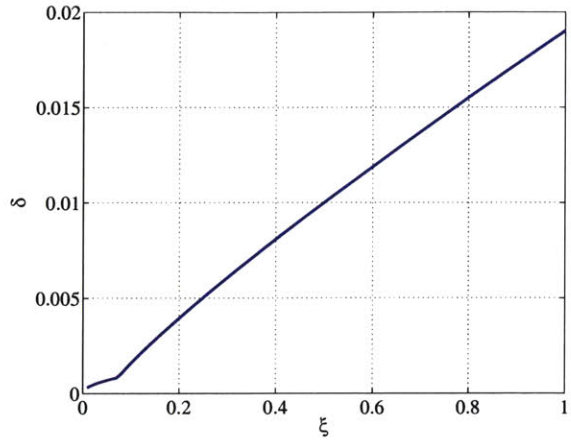

(a) Boundary Layer Thickness

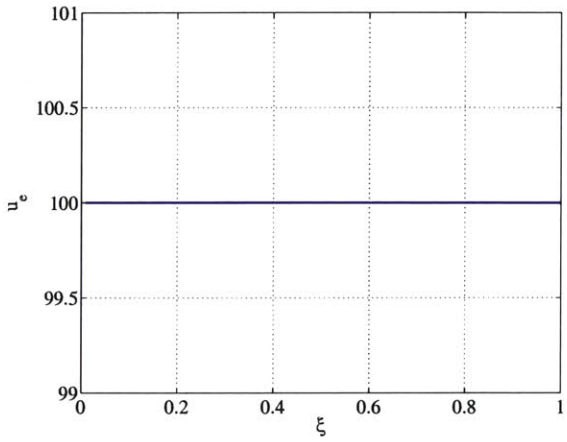

(b) Edge Velocity

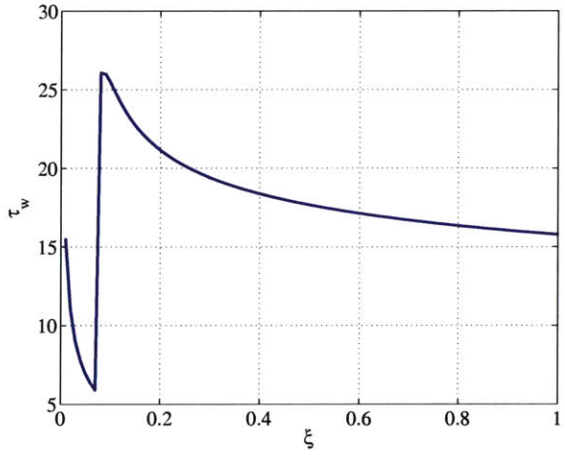

(c) Wall Shear Stress

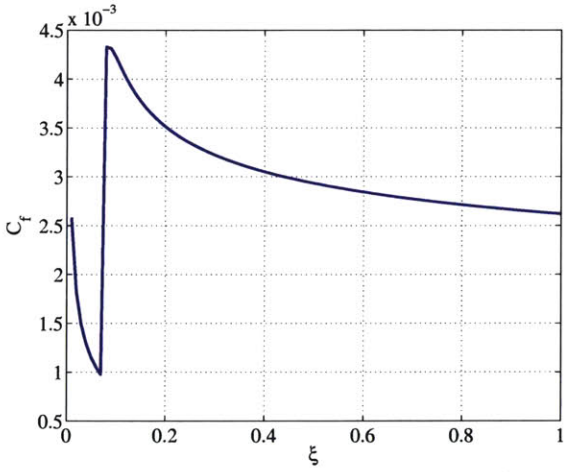

(d) Skin Friction Coefficient

Figure 5-4: Turbulent flat plate: δ, u_e, τ_w, and C_f vs. ξ.

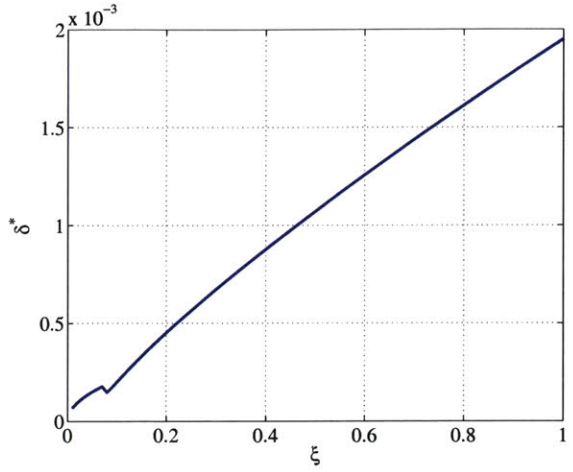

(a) Displacement Thickness

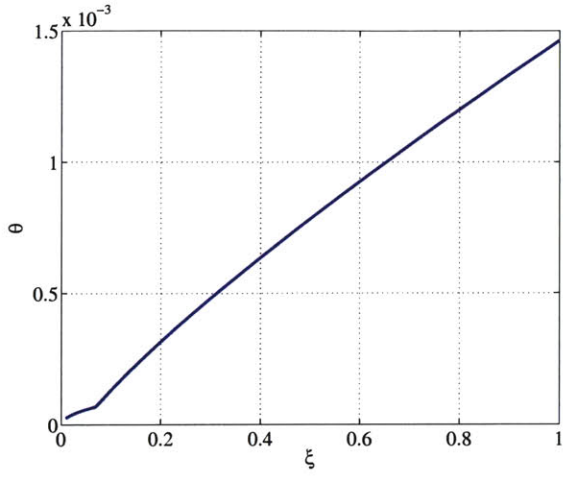

(b) Momentum Thickness

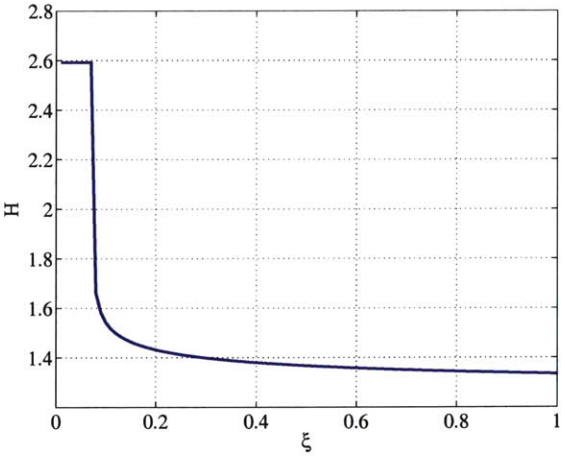

(c) Shape Parameter

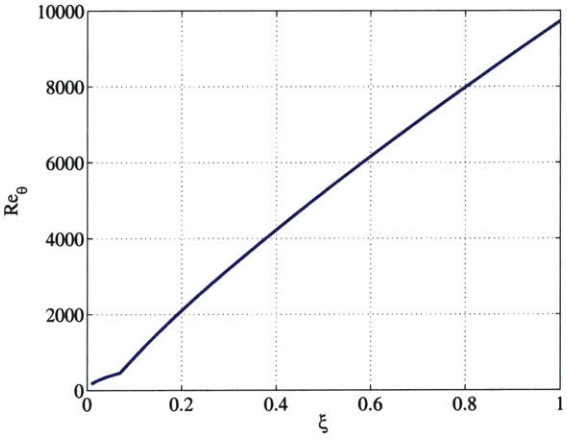

(d) Reynolds Number

Figure 5-5: Turbulent flat plate: δ^*, θ, H, and Re_θ vs. ξ.

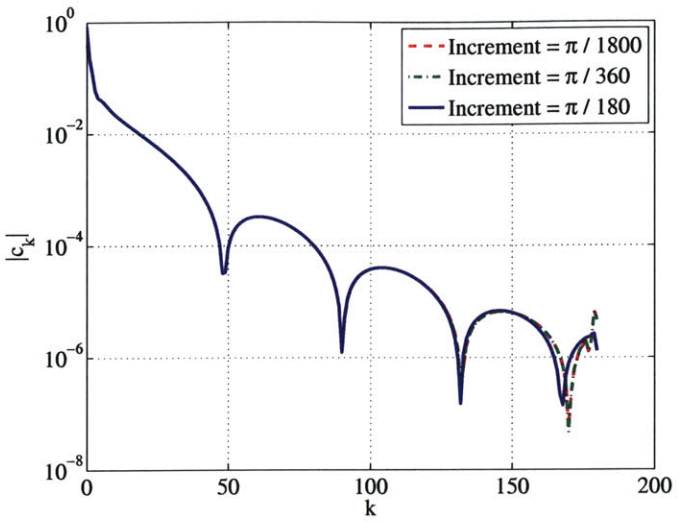

Figure 5-6: Turbulent flat plate: $|c_k|$ vs. k at $\xi = 1$ m.

where u_τ and l_τ are, respectively, the friction velocity and friction length. They are given by

$$u_\tau = s\left[\frac{|\tau_w|}{\rho}\right]^{1/2} \qquad \text{and} \qquad l_\tau = \frac{\nu}{u_\tau}, \tag{5.47}$$

where $s = \text{sgn}(\tau_w)$. The velocity construction takes the form

$$u_+ = u_{+S} + \frac{2\Pi}{\kappa} f\left(\frac{y}{\delta}\right), \tag{5.48}$$

where u_{+S} is governed by Spalding's law of the wall

$$y_+ = u_+ + e^{-\kappa B}\left[e^{\kappa u_+} - 1 - \kappa u_+ - \frac{(\kappa u_+)^2}{2} - \frac{(\kappa u_+)^3}{6}\right]. \tag{5.49}$$

The values of κ and B are those specified in Coles and Hirst [7]. The function

$$f\left(\frac{y}{\delta}\right) \approx \sin^2\left(\frac{\pi}{2}\frac{y}{\delta}\right) \tag{5.50}$$

and the Coles wake parameter $\Pi \approx 0.45$ for a flat plate (see White [41]) since there is a slight wake. Utilizing the skin friction law of Kestin and Persen [21],

$$C_f \approx \frac{0.455}{\ln^2(0.06\text{Re}_x)}, \tag{5.51}$$

u_τ can be calculated at some location on the plate (knowing the freestream velocity) and the profile constructed. Figure 5-7 demonstrates the close agreement in the profiles. Note that the logarithmic law of the wall (or log law),

$$u_+ = \frac{1}{\kappa}\ln y_+ + B, \tag{5.52}$$

has also been plotted for historical reasons.

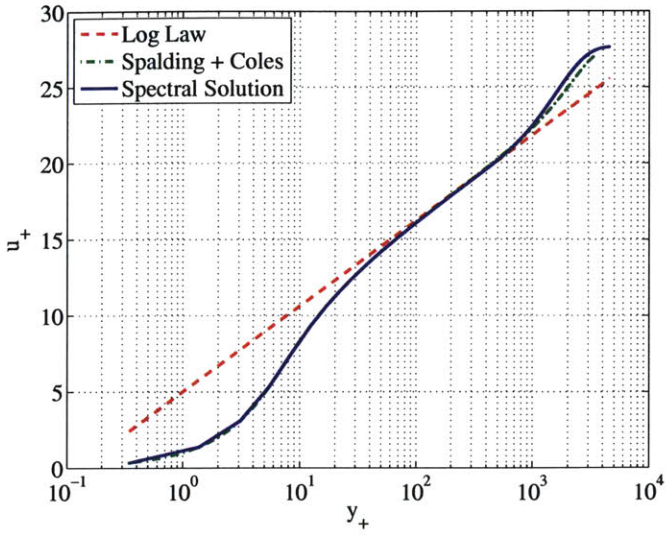

Figure 5-7: Velocity comparison using inner-law variables u_+ and y_+.

5.10 Wall Function

5.10.1 Modified Viscous Streamwise Velocity

The viscous streamwise velocity $u(\xi,\eta)$ defined on $\xi \in (0,\infty)$ and $\eta \in [-1,1]$ is modified by including an inner layer velocity profile, $u_\tau(\xi)\, u_{+S}(y_+)$, or wall function (WF) in its truncated series expansion approximation given by

$$u(\xi,\eta) \approx u_N(\xi,\eta) = u_e(\xi) \sum_{k=0}^{N} c_k(\xi)\, T_k(\eta) + u_\tau(\xi)\, u_{+S}(y_+), \tag{5.53}$$

where $u_e(\xi)$ is the edge velocity (streamwise component), $c_k(\xi)$ are the series coefficients, the chosen basis functions $T_k(\eta)$ are the Chebyshev polynomials, $u_\tau(\xi)$ is the friction velocity, and $u_{+S}(y_+)$ is Spalding's law of the wall [39].

5.10.2 Friction Velocity Constraint

The friction velocity $u_\tau(\xi)$ is a new unknown and it must be constrained accordingly. The residual

$$R_{u_\tau}(x) = \int_0^\delta (u_S - u)\, w_{u_\tau} dy = 0, \tag{5.54}$$

or equivalently,

$$R_{u_\tau}(\xi) = \frac{\delta}{2} \int_{-1}^{1} (u_S - u)\, w_{u_\tau} d\eta = 0, \tag{5.55}$$

ensures that the velocity profile in the inner layer is only approximated by Spalding's law of the wall. Note that $u_S = u_\tau u_{+S}$ and w_{u_τ} is given by

$$w_{u_\tau} = \frac{1}{2}\left\{1 + \tanh\left[K\left(1 - \zeta\right)\right]\right\}, \tag{5.56}$$

where $\zeta = \nu_{t_i}/\nu_{t_o}$ and $K = 40$. Figure 5-8 depicts the variation of w_{u_τ} with ζ. It is unity in the inner layer and zero in the outer layer.

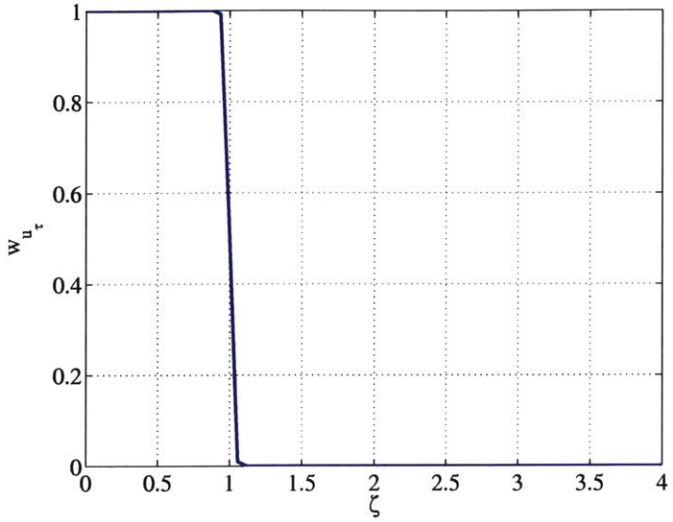

Figure 5-8: Graph of w_{u_τ} vs. ζ.

5.10.3 Modified Newton System

The vector of equations $\mathbf{F}$ will consist of the $N-1$ Galerkin equations R_G, the two boundary conditions, R_{BC_1} and R_{BC_2}, as well as the three constraint equations, R_{u_τ}, R_δ, and R_{u_e}. The vector of unknowns $\mathbf{U}$ will contain the $N+1$ series coefficients c_k, the friction velocity u_τ, the boundary layer thickness δ, and the edge velocity u_e. These vectors are given by

$$\mathbf{F} = \begin{bmatrix} R_{G_0} \\ \vdots \\ R_{G_{N-2}} \\ R_{BC_1} \\ R_{BC_2} \\ R_{u_\tau} \\ R_\delta \\ R_{u_e} \end{bmatrix} \quad \text{and} \quad \mathbf{U} = \begin{bmatrix} c_0 \\ \vdots \\ c_{N-2} \\ c_{N-1} \\ c_N \\ u_\tau \\ \delta \\ u_e \end{bmatrix}. \tag{5.57}$$

The Jacobian matrix $[\partial\mathbf{F}/\partial\mathbf{U}]$ will be an $(N+4) \times (N+4)$ matrix of the form

$$\left[\frac{\partial \mathbf{F}}{\partial \mathbf{U}}\right] = \begin{bmatrix} \frac{\partial R_{G_0}}{\partial c_0} & \cdots & \frac{\partial R_{G_0}}{\partial c_{N-2}} & \frac{\partial R_{G_0}}{\partial c_{N-1}} & \frac{\partial R_{G_0}}{\partial c_N} & \frac{\partial R_{G_0}}{\partial u_\tau} & \frac{\partial R_{G_0}}{\partial \delta} & \frac{\partial R_{G_0}}{\partial u_e} \\ \vdots & \ddots & \vdots & \vdots & \vdots & \vdots & \vdots & \vdots \\ \frac{\partial R_{G_{N-2}}}{\partial c_0} & \cdots & \frac{\partial R_{G_{N-2}}}{\partial c_{N-2}} & \frac{\partial R_{G_{N-2}}}{\partial c_{N-1}} & \frac{\partial R_{G_{N-2}}}{\partial c_N} & \frac{\partial R_{G_{N-2}}}{\partial u_\tau} & \frac{\partial R_{G_{N-2}}}{\partial \delta} & \frac{\partial R_{G_{N-2}}}{\partial u_e} \\ \frac{\partial R_{BC_1}}{\partial c_0} & \cdots & \frac{\partial R_{BC_1}}{\partial c_{N-2}} & \frac{\partial R_{BC_1}}{\partial c_{N-1}} & \frac{\partial R_{BC_1}}{\partial c_N} & \frac{\partial R_{BC_1}}{\partial u_\tau} & \frac{\partial R_{BC_1}}{\partial \delta} & \frac{\partial R_{BC_1}}{\partial u_e} \\ \frac{\partial R_{BC_2}}{\partial c_0} & \cdots & \frac{\partial R_{BC_2}}{\partial c_{N-2}} & \frac{\partial R_{BC_2}}{\partial c_{N-1}} & \frac{\partial R_{BC_2}}{\partial c_N} & \frac{\partial R_{BC_2}}{\partial u_\tau} & \frac{\partial R_{BC_2}}{\partial \delta} & \frac{\partial R_{BC_2}}{\partial u_e} \\ \frac{\partial R_{u_\tau}}{\partial c_0} & \cdots & \frac{\partial R_{u_\tau}}{\partial c_{N-2}} & \frac{\partial R_{u_\tau}}{\partial c_{N-1}} & \frac{\partial R_{u_\tau}}{\partial c_N} & \frac{\partial R_{u_\tau}}{\partial u_\tau} & \frac{\partial R_{u_\tau}}{\partial \delta} & \frac{\partial R_{u_\tau}}{\partial u_e} \\ \frac{\partial R_\delta}{\partial c_0} & \cdots & \frac{\partial R_\delta}{\partial c_{N-2}} & \frac{\partial R_\delta}{\partial c_{N-1}} & \frac{\partial R_\delta}{\partial c_N} & \frac{\partial R_\delta}{\partial u_\tau} & \frac{\partial R_\delta}{\partial \delta} & \frac{\partial R_\delta}{\partial u_e} \\ \frac{\partial R_{u_e}}{\partial c_0} & \cdots & \frac{\partial R_{u_e}}{\partial c_{N-2}} & \frac{\partial R_{u_e}}{\partial c_{N-1}} & \frac{\partial R_{u_e}}{\partial c_N} & \frac{\partial R_{u_e}}{\partial u_\tau} & \frac{\partial R_{u_e}}{\partial \delta} & \frac{\partial R_{u_e}}{\partial u_e} \end{bmatrix}. \quad (5.58)$$

5.11 Flat Plate Revisited

5.11.1 Detailed Plots

The spectral solution to turbulent flow over a flat plate was computed with the incorporation of the wall function. In this case, $N = 4$ based on the modal convergence at $\xi = 1$ m as shown in Figure 5-9. Detailed plots for the flat plate solution are shown in Figures 5-10 and 5-11.

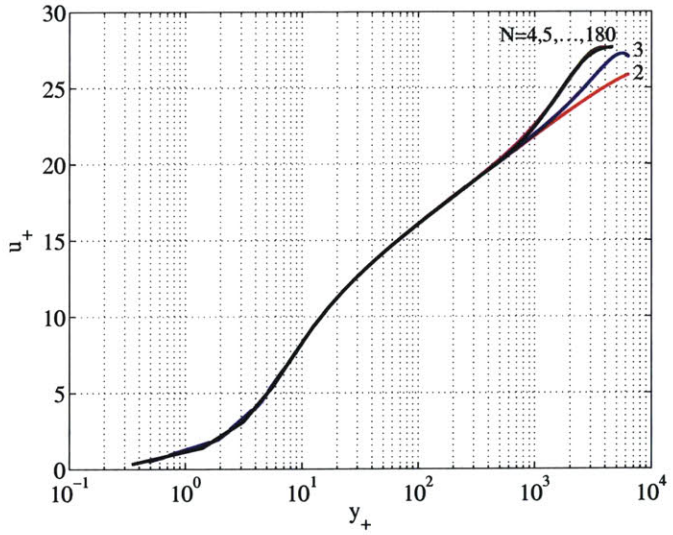

Figure 5-9: Turbulent flat plate (WF): Modal convergence at $\xi = 1$ m.

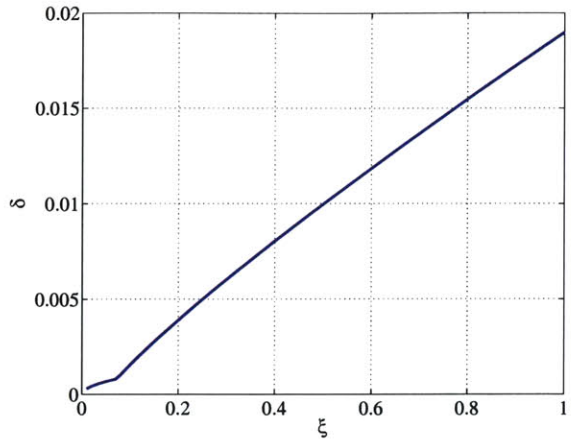

(a) Boundary Layer Thickness

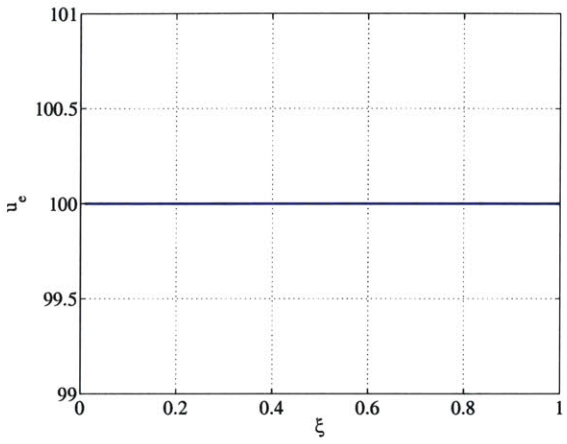

(b) Edge Velocity

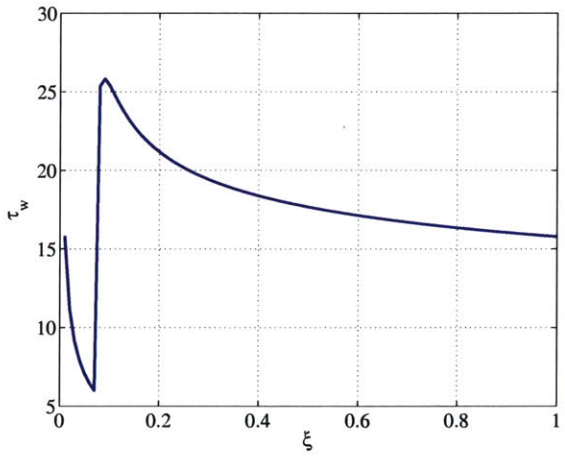

(c) Wall Shear Stress

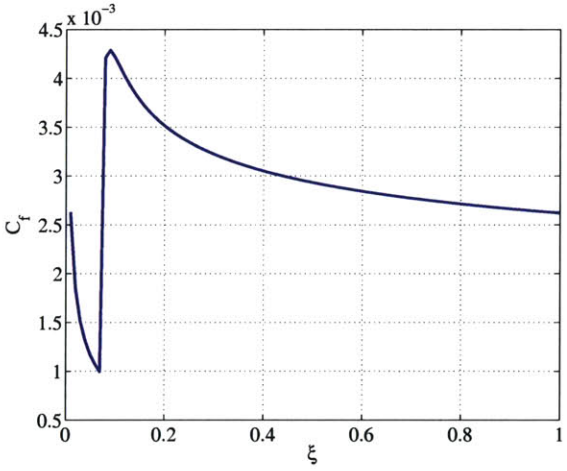

(d) Skin Friction Coefficient

Figure 5-10: Turbulent flat plate (WF): δ, u_e, τ_w, and C_f vs. ξ.

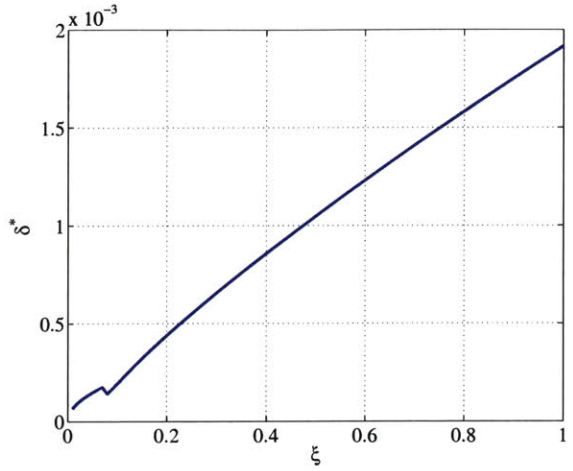

(a) Displacement Thickness

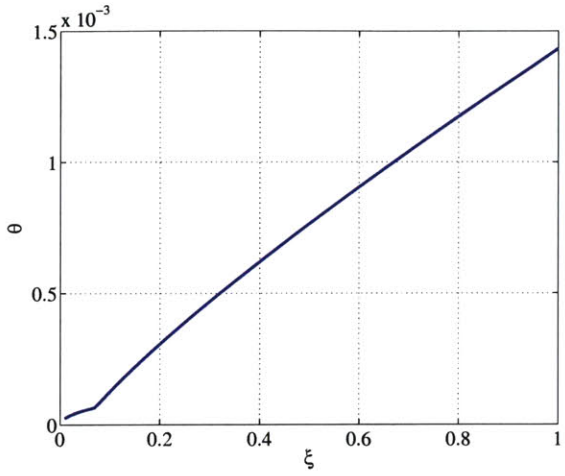

(b) Momentum Thickness

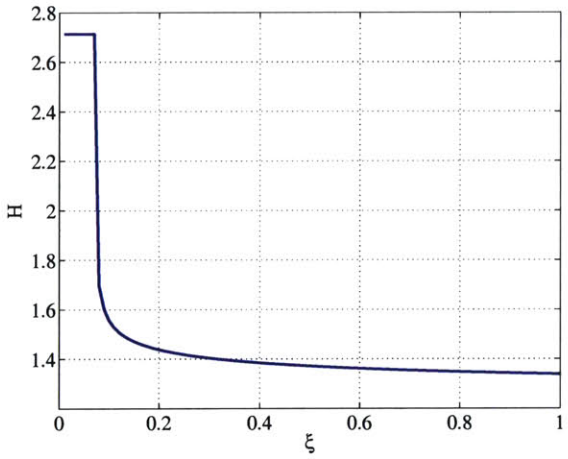

(c) Shape Parameter

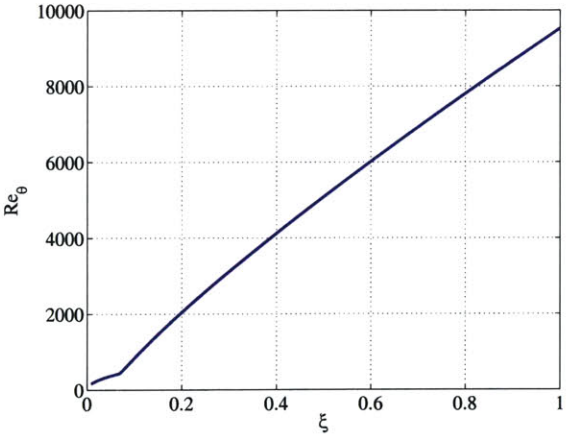

(d) Reynolds Number

Figure 5-11: Turbulent flat plate (WF): δ^*, θ, H, and Re_θ vs. ξ.

5.11.2 Velocity Comparison

The velocity profile obtained from the spectral method with the incorporation of the wall function was compared to the previously described velocity construction using Spalding's law of the wall [39] and Coles' law of the wake [6]. Once again, the agreement is excellent as shown in Figure 5-12. Note that the log law has also been plotted for historical reasons.

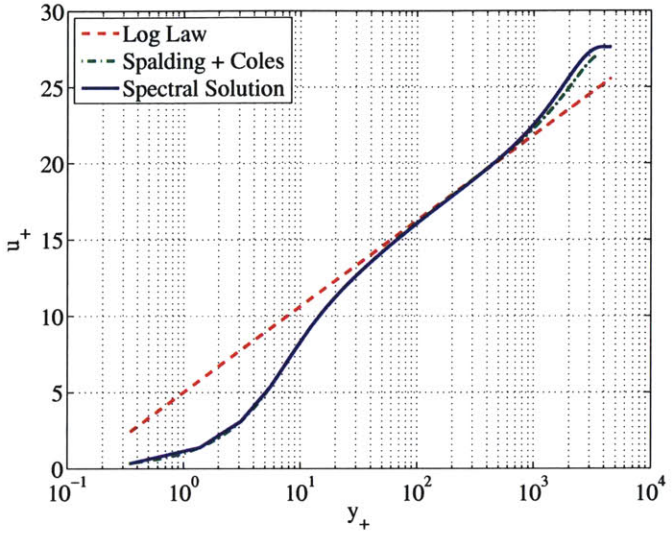

Figure 5-12: Velocity comparison using inner-law variables u_+ and y_+ (WF).

Figure 5-13 breaks down the velocity profile into its two contributions. It is reassuring to observe that the Chebyshev profile is zero (on the average) in the inner layer following the constraint equation R_{u_τ}. This allows the Spalding profile to approximate the velocity near the wall. In the outer layer, the Chebyshev profile corrects the velocity approximation as required to solve the flow.

The velocity gradient and shear stress contributions are depicted in Figures 5-14 and 5-15. The Chebyshev contribution has little effect on the overall $\partial u/\partial \eta$. The laminar component of the shear stress $\tau_l = \mu\,(\partial u/\partial \eta)$ scales the velocity gradient by the dynamic viscosity. Conversely, the turbulent component $\tau_t = \mu_t\,(\partial u/\partial \eta)$ utilizes the eddy viscosity as a scaling factor which varies with the location inside the boundary layer. Since the wall function is consistent with the inner layer eddy viscosity model, the shear stress exhibits a slight oscillation near the wall. At the edge, the shear stress does not go to zero since the eddy viscosity has a nonzero value in the outer layer (i.e. Clauser's formulation). These oscillations can be alleviated with more modes. Nevertheless, the total shear stress profile is fairly accurate for only $N = 4$.

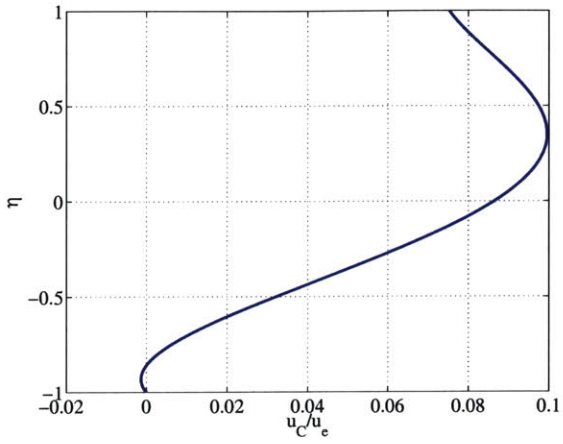

(a) Chebyshev

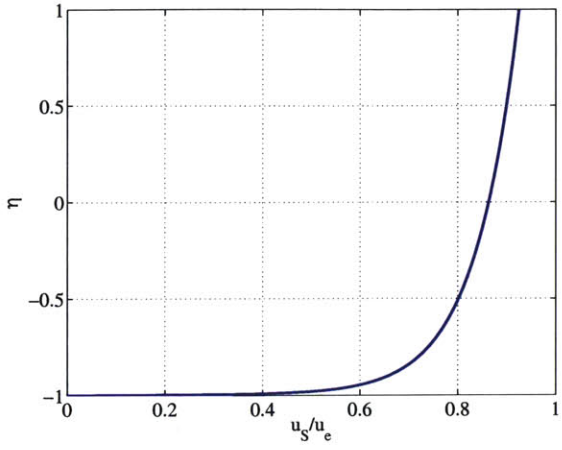

(b) Spalding

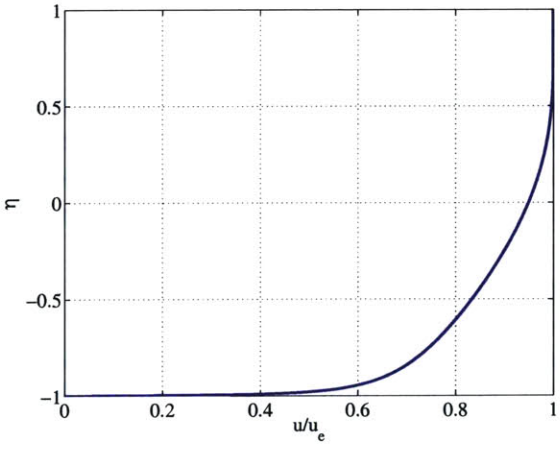

(c) Total

Figure 5-13: Velocity profile contributions (WF).

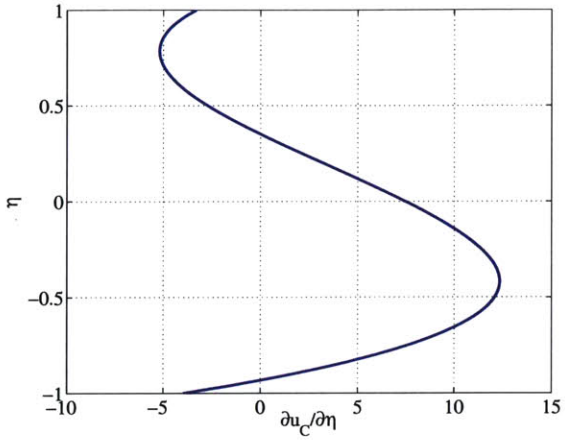

(a) Chebyshev

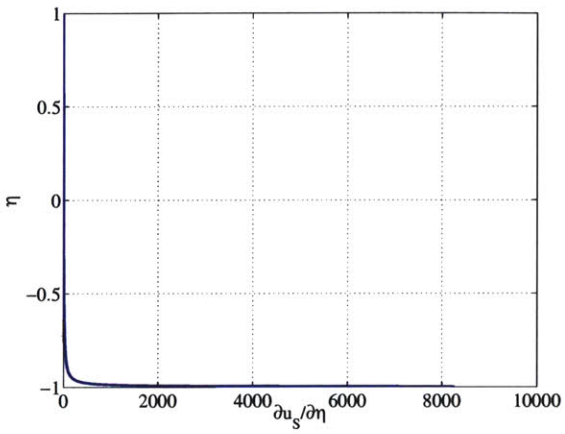

(b) Spalding

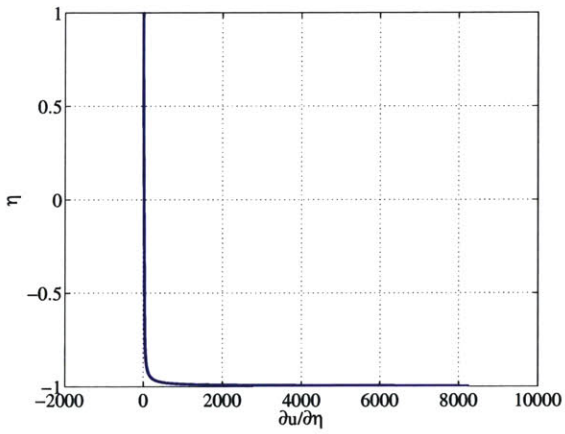

(c) Total

Figure 5-14: Velocity gradient contributions (WF).

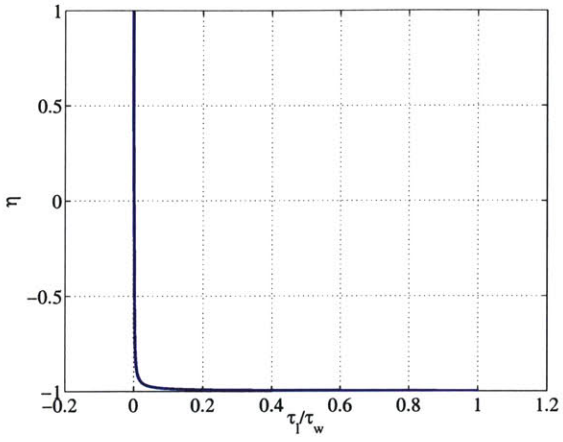

(a) Laminar

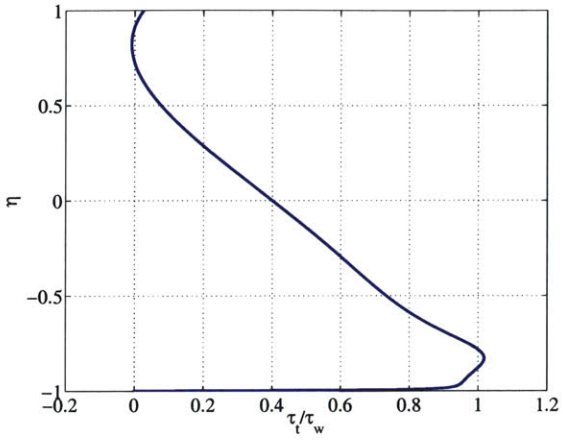

(b) Turbulent

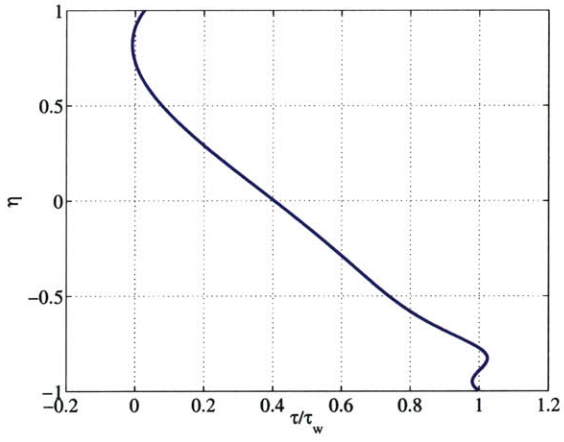

(c) Total

Figure 5-15: Shear stress contributions (WF).

5.12 Flat Plate with Wall Suction or Blowing

5.12.1 Modified Law of the Wall

Wall suction, $v_w < 0$, or blowing, $v_w > 0$, adds a strong streamwise convective acceleration $v_w\,(\partial u/\partial y)$ to the near-wall boundary layer. For the flat plate case where the pressure gradient is zero, the momentum equation very near the wall becomes

$$\rho v_w \frac{\partial u}{\partial y} \approx \frac{\partial \tau}{\partial y} \qquad \text{or} \qquad \tau \approx \tau_w + \rho v_w u. \tag{5.59}$$

Therefore, the wall velocity has a profound effect on the shear distribution. By matching this expression to an eddy viscosity model of turbulent shear, Stevenson [40] derived a modified logarithmic law of the wall with suction or blowing, that is

$$\frac{2}{v_{w_+}}\left[\left(1 + v_{w_+} u_+\right)^{1/2} - 1\right] \approx \frac{1}{\kappa} \ln y_+ + B, \tag{5.60}$$

where $v_{w_+} = v_w/u_\tau$. For $v_w = 0$ this relation reduces to the solid wall case. The typical range of v_{w_+} is ± 0.06. Figure 5-16 illustrates Stevenson's correlation.

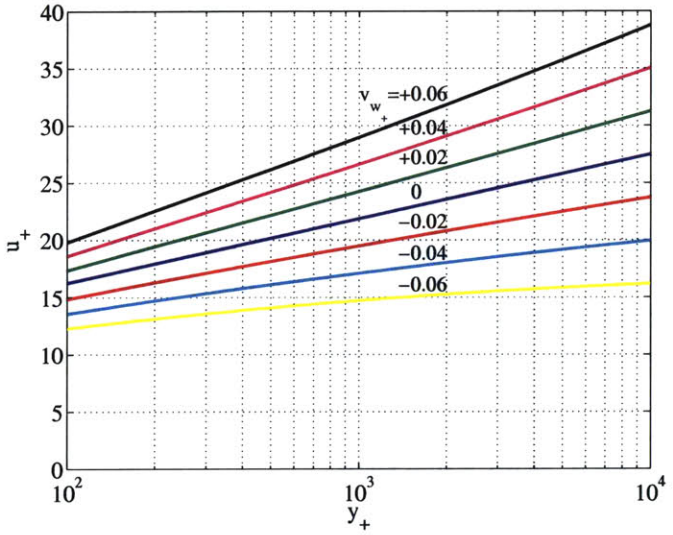

Figure 5-16: Effect of suction and blowing on logarithmic law of the wall.

In this study, the inner layer velocity profile is approximated by Spalding's law of the wall. Hence, it needs to be modified to cope with a nonzero wall velocity v_w. Define a modified inner-law variable, u^*_+, such that

$$u^*_+ \equiv \frac{2}{v_{w_+}}\left[\left(1 + v_{w_+} u_+\right)^{1/2} - 1\right], \tag{5.61}$$

and demand that the following conditions be met

$$\begin{aligned} u_+ &\to 0 \quad ; \quad y_+ \to u_+, \\ u_+ &\to \infty \quad ; \quad y_+ \to e^{-\kappa B} e^{\kappa u^*_+}. \end{aligned} \tag{5.62}$$

This suggests

$$y_+ = u_+ + e^{-\kappa B}\left[e^{\kappa u_+^*} - 1 - \kappa u_+^* - \frac{\left(\kappa u_+^*\right)^2}{2} - \frac{\left(\kappa u_+^*\right)^3}{6}\right], \tag{5.63}$$

from which $u_{+_S}(y_+)$ will be governed.

5.12.2 Modified Inner Layer Eddy Viscosity

By matching

$$\left(\mu + \mu_{t_i}\right)\frac{\partial u}{\partial y} = \tau_w + \rho v_w u, \tag{5.64}$$

the above can be simplified to

$$1 + \frac{\mu_{t_i}}{\mu} = \frac{dy_+}{du_+}\left(\frac{1}{\left.\frac{dy_+}{du_+}\right|_{u_+=0}} + v_{w_+}u_+\right). \tag{5.65}$$

Substituting the expression for y_+ and noting that $\left.\frac{dy_+}{du_+}\right|_{u_+=0} = 1$ the modified ν_{t_i} will be

$$\nu_{t_i} \approx \left(1 + v_{w_+}u_+\right)\frac{\nu\kappa e^{-\kappa B}}{\left(1 + v_{w_+}u_+\right)^{1/2}}\left[e^{\kappa u_+^*} - 1 - \kappa u_+^* - \frac{\left(\kappa u_+^*\right)^2}{2}\right]. \tag{5.66}$$

5.12.3 Results without Wall Function

The spectral solution to turbulent flow over a flat plate with wall suction or blowing was computed with $N = 180$. The length of the plate was doubled with the second half having flow control applied to it. Figure 5-17 depicts the effect on the law of the wall at $\xi = 2$ m. Comparison with Stevenson's correlation is shown in Figure 5-18. The agreement is excellent.

5.12.4 Results with Wall Function

The spectral solution to turbulent flow over a flat plate with wall suction or blowing was computed with the incorporation of the wall function. Once again, the length of the plate was doubled with the second half having flow control applied to it. Figure 5-19 depicts the effect on the law of the wall at $\xi = 2$ m. Comparison with Stevenson's correlation is shown in Figure 5-20. The agreement is excellent. In this case, $N = 4$ and as N is increased the solution exists and the oscillations are reduced, just as in the flat plate case with no flow control.

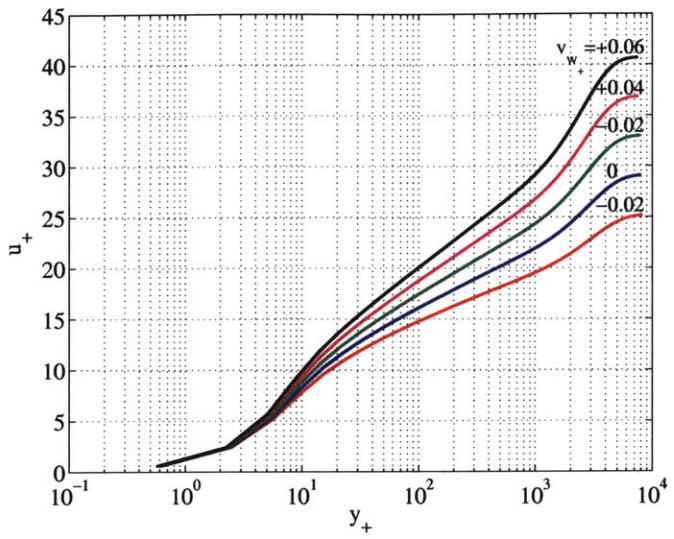

Figure 5-17: Suction/blowing effect on a flat plate: u_+ vs. y_+.

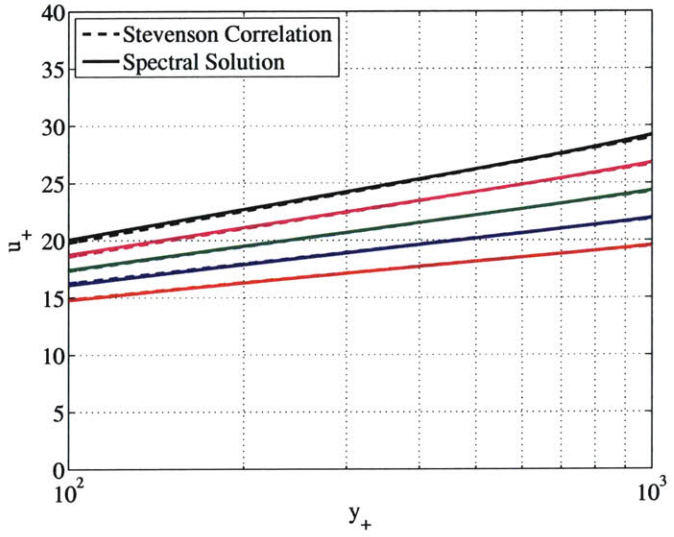

Figure 5-18: Comparison with Stevenson correlation: u_+ vs. y_+.

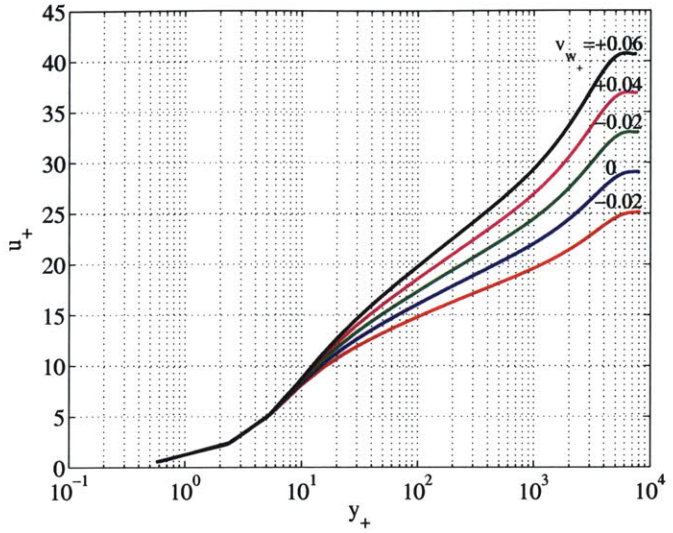

Figure 5-19: Suction/blowing effect on a flat plate (WF): u_+ vs. y_+.

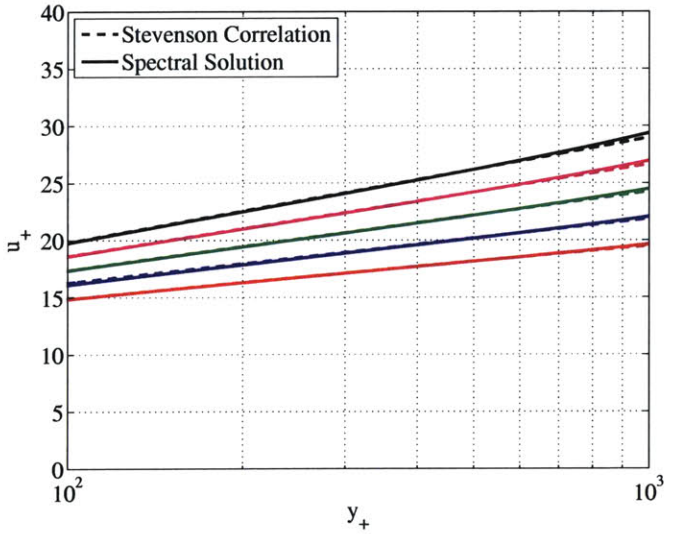

Figure 5-20: Comparison with Stevenson correlation (WF): u_+ vs. y_+.

5.13 Turbulent Jet

5.13.1 Modified Outer Layer Eddy Viscosity

Clauser's eddy viscosity has the form

$$\nu_{t_o} \sim (\text{velocity across layer}) \times (\text{thickness of layer}) \sim u_e \delta^*, \tag{5.67}$$

which can be viewed as a dimensional argument. Hence, the outer layer eddy viscosity model ν_{t_o} was altered to

$$\nu_{t_o} = C\overline{\Delta u}\delta, \tag{5.68}$$

where $C = 0.0001$, δ is the boundary layer thickness, and $\overline{\Delta u}$ is a root-mean-square velocity jump measure given by

$$\overline{\Delta u} = \left[\delta \int_0^\delta \left(\frac{\partial u}{\partial y}\right)^2 dy\right]^{1/2} = \left[2 \int_{-1}^1 \left(\frac{\partial u}{\partial \eta}\right)^2 d\eta\right]^{1/2}. \tag{5.69}$$

For the jet, utilizing Clauser's formulation would be out of the question since δ^* can become negative for a strong enough jet.

5.13.2 Modified w_{u_τ}

In order to make sure the inner layer eddy viscosity ν_{t_i} is applied below the maximum jet velocity, the function w_{u_τ} was modified to be

$$w_{u_\tau} = \frac{1}{2}\left\{1 - \tanh\left[K\left(\frac{y}{\delta} - \frac{y^*}{\delta}\right)\right]\right\}, \tag{5.70}$$

where $K = 1000$. The term y^* is the percentage of the boundary layer thickness below the maximum jet velocity. Noting that $\eta = 2y/\delta - 1$ and $\eta^* = 2y^*/\delta - 1$ the expression can be simplified to

$$w_{u_\tau} = \frac{1}{2}\left\{1 - \tanh\left[\frac{K}{2}(\eta - \eta^*)\right]\right\}. \tag{5.71}$$

5.13.3 Results without Wall Function

The spectral solution to the turbulent jet case was computed with $N = 180$. The setup was identical to the laminar jet but the flow was tripped to become turbulent five slot lengths downstream of the slot. Figure 5-21 depicts the velocity and shear stress profiles. Figure 5-22 illustrates the convergence rate of the series coefficients on a log-linear plot at $\xi = 1$ m. Although this plot is typical of coefficients which oscillate with N (see Boyd [2]) the convergence is not exponential just like the turbulent flat plate case. This is primarily due to a lack of smoothness for u rather than integration error.

5.13.4 Results with Wall Function

The spectral solution to the turbulent jet case was computed with the incorporation of the wall function. To achieve an almost identical match to the case without a wall function,

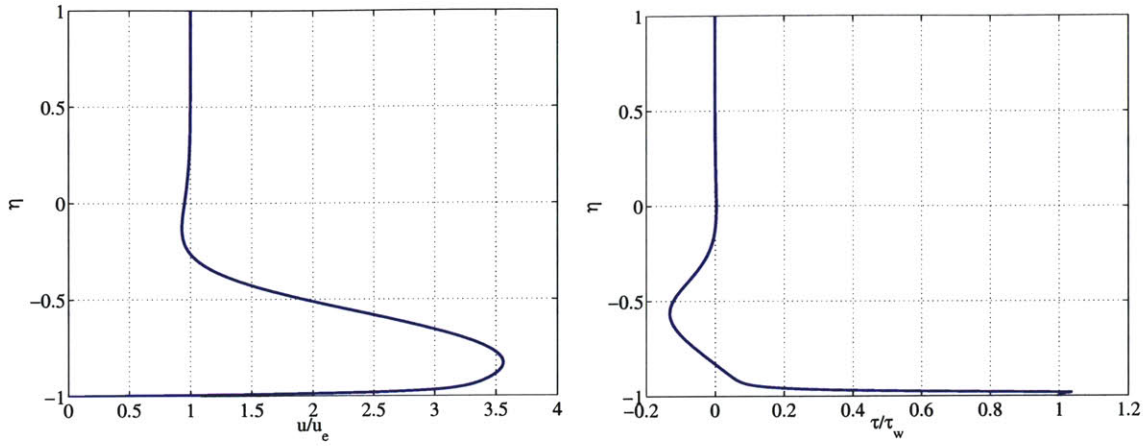

(a) Velocity Profile

(b) Shear Stress Profile

Figure 5-21: Turbulent jet: u/u_e and τ/τ_w profiles at $\xi = 1$ m.

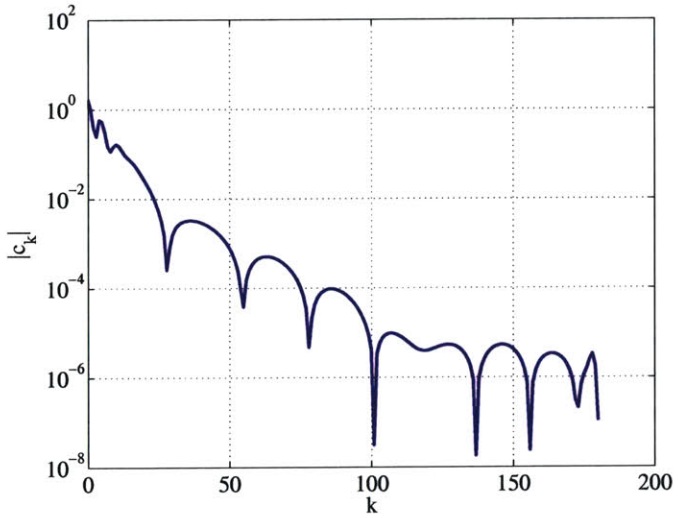

Figure 5-22: Turbulent jet: $|c_k|$ vs. k at $\xi = 1$ m.

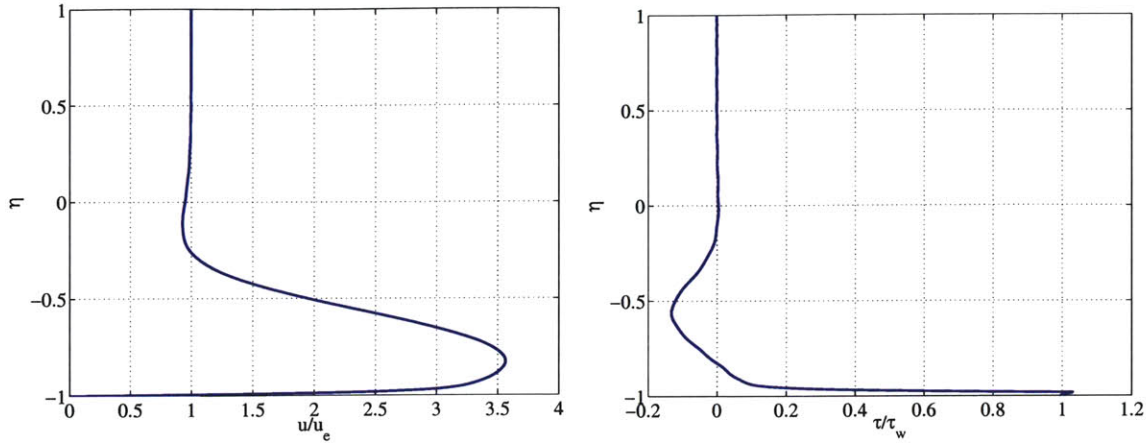

(a) Velocity Profile

(b) Shear Stress Profile

Figure 5-23: Turbulent jet (WF): u/u_e and τ/τ_w profiles at $\xi = 1$ m.

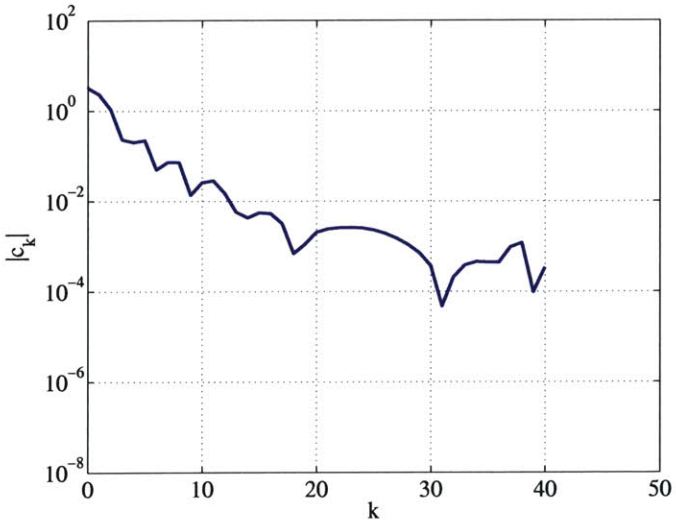

Figure 5-24: Turbulent jet (WF): $|c_k|$ vs. k at $\xi = 1$ m.

$N = 40$ although $N = 20$ or $N = 30$ would give workable solutions. Figure 5-23 depicts the velocity and shear stress profiles. Figure 5-24 illustrates the convergence rate of the series coefficients on a log-linear plot at $\xi = 1$ m. Once again, the convergence is not exponential primarily due to a lack of smoothness for u rather than integration error.

Chapter 6

Spalart-Allmaras One-Equation Turbulence Model

The Spalart-Allmaras turbulence model [38] is a one-equation model assembled using empiricism and arguments of dimensional analysis, Galilean invariance, and selective dependence on the molecular viscosity. It computes the turbulent shear (or Reynolds stress) $-\rho\overline{u'v'}$ from a transport equation for the rate of change of stress. The spectral method is applied in solving this equation which is coupled to the defect form of the 2-D, steady, incompressible viscous momentum equation through the eddy viscosity. The Newton iteration scheme is applied to the entire system of nonlinear equations. Results for the flat plate case are reported. A wall function is introduced into the approximation of the streamwise velocity and the flat plate problem is solved once more. The inconsistency between the wall function and the turbulence model within the inner layer produces an erroneous shear stress.

6.1 Reynolds Stress Transport Equation

The eddy viscosity ν_t is given by

$$\nu_t = \tilde{\nu} f_{v1}, \qquad f_{v1} = \frac{\chi^3}{\chi^3 + c_{v1}^3}, \qquad \chi \equiv \frac{\tilde{\nu}}{\nu}, \tag{6.1}$$

where ν is the kinematic (or molecular) viscosity. The working variable $\tilde{\nu}$ obeys the transport equation

$$\frac{\partial}{\partial x}\left(u\tilde{\nu}\right) + \frac{\partial}{\partial y}\left(v\tilde{\nu}\right) = c_{b1}\tilde{S}\tilde{\nu} + \frac{1}{\sigma}\left\{\frac{\partial}{\partial y}\left[\left(\nu + \tilde{\nu}\right)\frac{\partial \tilde{\nu}}{\partial y}\right] + c_{b2}\left(\frac{\partial \tilde{\nu}}{\partial y}\right)^2\right\} - c_{w1} f_w \left(\frac{\tilde{\nu}}{y}\right)^2. \tag{6.2}$$

Here S is the magnitude of the vorticity,

$$S = \left|\frac{\partial u}{\partial y}\right|, \qquad \tilde{S} \equiv S + \frac{\tilde{\nu}}{\kappa^2 y^2} f_{v2}, \qquad f_{v2} = 1 - \frac{\chi}{1 + \chi f_{v1}}, \tag{6.3}$$

and y is the perpendicular distance from the wall. The function f_w is

$$f_w = g\left[\frac{1 + c_{w3}^6}{g^6 + c_{w3}^6}\right]^{1/6}, \qquad g = r + c_{w2}\left(r^6 - r\right), \qquad r \equiv \frac{\tilde{\nu}}{\tilde{S}\kappa^2 y^2}. \tag{6.4}$$

The list of constants are $c_{b1} = 0.1355$, $\sigma = 2/3$, $c_{b2} = 0.622$, $\kappa = 0.41$, $c_{w1} = c_{b1}/\kappa^2 + (1 + c_{b2})/\sigma$, $c_{w2} = 0.3$, $c_{w3} = 2$, and $c_{v1} = 7.1$.

6.2 Local Scaling Transformation

Applying the coordinate transformation $(x, y) \rightarrow (\xi, \eta)$ described in Section 4.1.4 to (6.2) gives

$$\begin{aligned} &\frac{\partial}{\partial \xi}(u\tilde{\nu}) - \frac{(\eta+1)}{\delta}\frac{d\delta}{d\xi}\frac{\partial}{\partial \eta}(u\tilde{\nu}) + \frac{2}{\delta}\frac{\partial}{\partial \eta}(v\tilde{\nu}) - c_{b1}\tilde{S}\tilde{\nu} \\ &\quad - \frac{1}{\sigma}\frac{4}{\delta^2}\left\{\frac{\partial}{\partial \eta}\left[(\nu+\tilde{\nu})\frac{\partial \tilde{\nu}}{\partial \eta}\right] + c_{b2}\left(\frac{\partial \tilde{\nu}}{\partial \eta}\right)^2\right\} + c_{w1}f_w\frac{4}{\delta^2}\left(\frac{\tilde{\nu}}{\eta+1}\right)^2 = 0, \end{aligned} \tag{6.5}$$

which is the PDE of interest.

6.3 Series Approximation to Working Variable

The working variable $\tilde{\nu}(\xi, \eta)$ defined on $\xi \in (0, \infty)$ and $\eta \in [-1, 1]$ can be approximated by the truncated series expansion given by

$$\tilde{\nu}(\xi, \eta) \approx \tilde{\nu}_{\tilde{N}}(\xi, \eta) = \nu \sum_{k=0}^{\tilde{N}} d_k(\xi) T_k(\eta), \tag{6.6}$$

where ν is the kinematic viscosity, $d_k(\xi)$ are the series coefficients, and the chosen basis functions $T_k(\eta)$ are the Chebyshev polynomials.

6.4 Weighted Residual Statement

Substituting the expression for $\tilde{\nu}$ into the PDE of interest (6.5) yields the residual function $\tilde{R}(\xi, \eta)$. It has the form

$$\begin{aligned} \tilde{R}(\xi, \eta) = &\frac{\partial}{\partial \xi}(u\tilde{\nu}) - \frac{(\eta+1)}{\delta}\frac{d\delta}{d\xi}\frac{\partial}{\partial \eta}(u\tilde{\nu}) + \frac{2}{\delta}\frac{\partial}{\partial \eta}(v\tilde{\nu}) - c_{b1}\tilde{S}\tilde{\nu} \\ &- \frac{1}{\sigma}\frac{4}{\delta^2}\left\{\frac{\partial}{\partial \eta}\left[(\nu+\tilde{\nu})\frac{\partial \tilde{\nu}}{\partial \eta}\right] + c_{b2}\left(\frac{\partial \tilde{\nu}}{\partial \eta}\right)^2\right\} + c_{w1}f_w\frac{4}{\delta^2}\left(\frac{\tilde{\nu}}{\eta+1}\right)^2. \end{aligned} \tag{6.7}$$

Applying the MWR (Galerkin-type) gives

$$\left(\tilde{R}, T_j\right)_w = \int_{-1}^{1} \tilde{R}(\xi, \eta) T_j(\eta) w(\eta) d\eta = 0, \tag{6.8}$$

where the weight $w(\eta)$ is chosen to be unity

$$w(\eta) = 1. \tag{6.9}$$

Utilizing the orthogonality weight associated with the Chebyshev polynomials tends to cause the nonlinear system to be more ill-conditioned. Therefore, the weighted residual statement is

$$\int_{-1}^{1} \tilde{R}(\xi,\eta)\, T_j(\eta)\, d\eta = 0. \tag{6.10}$$

Hence, there are $\tilde{N}+1$ Galerkin equations $\tilde{R}_{G_j}(\xi)$ defined by

$$\tilde{R}_{G_j}(\xi) \equiv \int_{-1}^{1} \tilde{R}(\xi,\eta)\, T_j(\eta)\, d\eta = 0. \tag{6.11}$$

Unless otherwise noted, the integration will be performed using the trapezoidal rule. The integration points are chosen using $\eta = -\cos\varphi$ with φ ranging from $[0,\pi]$ in increments of $\pi/180$.

6.5 Boundary Conditions

At the edge of the boundary layer

$$\tilde{\nu}(x,\delta) = 0 \qquad \text{or} \qquad \tilde{\nu}(\xi,1) = 0, \tag{6.12}$$

and at the wall

$$\tilde{\nu}(x,0) = 0 \qquad \text{or} \qquad \tilde{\nu}(\xi,-1) = 0. \tag{6.13}$$

The tau method is used to impose these two boundary conditions. As such, the last two Galerkin equations are replaced by the equations for the boundary conditions denoted by

$$\tilde{R}_{BC_1}(x,\delta) = \tilde{\nu}(x,\delta) = 0 \qquad \text{or} \qquad \tilde{R}_{BC_1}(\xi,1) = \tilde{\nu}(\xi,1) = 0, \tag{6.14}$$

and

$$\tilde{R}_{BC_2}(x,0) = \tilde{\nu}(x,0) = 0 \qquad \text{or} \qquad \tilde{R}_{BC_2}(\xi,-1) = \tilde{\nu}(\xi,-1) = 0. \tag{6.15}$$

Therefore, $j \in J_{\tilde{N}}$ has $J_{\tilde{N}} = \left\{0,\ldots,\tilde{N}-2\right\}$.

6.6 Newton Solver

The system of nonlinear equations is solved by means of the Newton iteration scheme as described in Section 4.6.1.

In the present application the vector of equations $\mathbf{F}$ will consist of the $N-1$ Galerkin equations R_G, the two boundary conditions, R_{BC_1} and R_{BC_2}, the two constraint equations, R_δ and R_{u_e}, the $\tilde{N}-1$ Galerkin equations $\tilde{R}_G$, and the two boundary conditions, $\tilde{R}_{BC_1}$ and $\tilde{R}_{BC_2}$. The vector of unknowns $\mathbf{U}$ will contain the $N+1$ series coefficients c_k, the boundary layer thickness δ, the edge velocity u_e, and the $\tilde{N}+1$ series coefficients d_k. These vectors are given by

$$\mathbf{F} = \begin{bmatrix} R_{G_0} \\ \vdots \\ R_{G_{N-2}} \\ R_{BC_1} \\ R_{BC_2} \\ R_\delta \\ R_{u_e} \\ \tilde{R}_{G_0} \\ \vdots \\ \tilde{R}_{G_{\tilde{N}-2}} \\ \tilde{R}_{BC_1} \\ \tilde{R}_{BC_2} \end{bmatrix} \quad \text{and} \quad \mathbf{U} = \begin{bmatrix} c_0 \\ \vdots \\ c_{N-2} \\ c_{N-1} \\ c_N \\ \delta \\ u_e \\ d_0 \\ \vdots \\ d_{\tilde{N}-2} \\ d_{\tilde{N}-1} \\ d_{\tilde{N}} \end{bmatrix}. \tag{6.16}$$

The Jacobian matrix $[\partial\mathbf{F}/\partial\mathbf{U}]$ will be an $\left(N+\tilde{N}+4\right) \times \left(N+\tilde{N}+4\right)$ matrix of the form

$$\begin{bmatrix} \dfrac{\partial \mathbf{F}}{\partial \mathbf{U}} \end{bmatrix} = \begin{bmatrix} \mathbf{A} & \mathbf{B} \\ \mathbf{C} & \mathbf{D} \end{bmatrix}, \tag{6.17}$$

where the matrices **A**, **B**, **C**, and **D** are given by

$$\mathbf{A} = \begin{bmatrix} \frac{\partial R_{G_0}}{\partial c_0} & \cdots & \frac{\partial R_{G_0}}{\partial c_{N-2}} & \frac{\partial R_{G_0}}{\partial c_{N-1}} & \frac{\partial R_{G_0}}{\partial c_N} & \frac{\partial R_{G_0}}{\partial \delta} & \frac{\partial R_{G_0}}{\partial u_e} \\ \vdots & \ddots & \vdots & \vdots & \vdots & \vdots & \vdots \\ \frac{\partial R_{G_{N-2}}}{\partial c_0} & \cdots & \frac{\partial R_{G_{N-2}}}{\partial c_{N-2}} & \frac{\partial R_{G_{N-2}}}{\partial c_{N-1}} & \frac{\partial R_{G_{N-2}}}{\partial c_N} & \frac{\partial R_{G_{N-2}}}{\partial \delta} & \frac{\partial R_{G_{N-2}}}{\partial u_e} \\ \frac{\partial R_{BC_1}}{\partial c_0} & \cdots & \frac{\partial R_{BC_1}}{\partial c_{N-2}} & \frac{\partial R_{BC_1}}{\partial c_{N-1}} & \frac{\partial R_{BC_1}}{\partial c_N} & \frac{\partial R_{BC_1}}{\partial \delta} & \frac{\partial R_{BC_1}}{\partial u_e} \\ \frac{\partial R_{BC_2}}{\partial c_0} & \cdots & \frac{\partial R_{BC_2}}{\partial c_{N-2}} & \frac{\partial R_{BC_2}}{\partial c_{N-1}} & \frac{\partial R_{BC_2}}{\partial c_N} & \frac{\partial R_{BC_2}}{\partial \delta} & \frac{\partial R_{BC_2}}{\partial u_e} \\ \frac{\partial R_\delta}{\partial c_0} & \cdots & \frac{\partial R_\delta}{\partial c_{N-2}} & \frac{\partial R_\delta}{\partial c_{N-1}} & \frac{\partial R_\delta}{\partial c_N} & \frac{\partial R_\delta}{\partial \delta} & \frac{\partial R_\delta}{\partial u_e} \\ \frac{\partial R_{u_e}}{\partial c_0} & \cdots & \frac{\partial R_{u_e}}{\partial c_{N-2}} & \frac{\partial R_{u_e}}{\partial c_{N-1}} & \frac{\partial R_{u_e}}{\partial c_N} & \frac{\partial R_{u_e}}{\partial \delta} & \frac{\partial R_{u_e}}{\partial u_e} \end{bmatrix}, \tag{6.18}$$

$$\mathbf{B} = \begin{bmatrix} \frac{\partial R_{G_0}}{\partial d_0} & \cdots & \frac{\partial R_{G_0}}{\partial d_{\tilde{N}-2}} & \frac{\partial R_{G_0}}{\partial d_{\tilde{N}-1}} & \frac{\partial R_{G_0}}{\partial d_{\tilde{N}}} \\ \vdots & \ddots & \vdots & \vdots & \vdots \\ \frac{\partial R_{G_{N-2}}}{\partial d_0} & \cdots & \frac{\partial R_{G_{N-2}}}{\partial d_{\tilde{N}-2}} & \frac{\partial R_{G_{N-2}}}{\partial d_{\tilde{N}-1}} & \frac{\partial R_{G_{N-2}}}{\partial d_{\tilde{N}}} \\ \frac{\partial R_{BC_1}}{\partial d_0} & \cdots & \frac{\partial R_{BC_1}}{\partial d_{\tilde{N}-2}} & \frac{\partial R_{BC_1}}{\partial d_{\tilde{N}-1}} & \frac{\partial R_{BC_1}}{\partial d_{\tilde{N}}} \\ \frac{\partial R_{BC_2}}{\partial d_0} & \cdots & \frac{\partial R_{BC_2}}{\partial d_{\tilde{N}-2}} & \frac{\partial R_{BC_2}}{\partial d_{\tilde{N}-1}} & \frac{\partial R_{BC_2}}{\partial d_{\tilde{N}}} \\ \frac{\partial R_\delta}{\partial d_0} & \cdots & \frac{\partial R_\delta}{\partial d_{\tilde{N}-2}} & \frac{\partial R_\delta}{\partial d_{\tilde{N}-1}} & \frac{\partial R_\delta}{\partial d_{\tilde{N}}} \\ \frac{\partial R_{u_e}}{\partial d_0} & \cdots & \frac{\partial R_{u_e}}{\partial d_{\tilde{N}-2}} & \frac{\partial R_{u_e}}{\partial d_{\tilde{N}-1}} & \frac{\partial R_{u_e}}{\partial d_{\tilde{N}}} \end{bmatrix}, \tag{6.19}$$

$$\mathbf{C} = \begin{bmatrix} \frac{\partial \tilde{R}_{G_0}}{\partial c_0} & \cdots & \frac{\partial \tilde{R}_{G_0}}{\partial c_{N-2}} & \frac{\partial \tilde{R}_{G_0}}{\partial c_{N-1}} & \frac{\partial \tilde{R}_{G_0}}{\partial c_N} & \frac{\partial \tilde{R}_{G_0}}{\partial \delta} & \frac{\partial \tilde{R}_{G_0}}{\partial u_e} \\ \vdots & \ddots & \vdots & \vdots & \vdots & \vdots & \vdots \\ \frac{\partial \tilde{R}_{G_{\tilde{N}-2}}}{\partial c_0} & \cdots & \frac{\partial \tilde{R}_{G_{\tilde{N}-2}}}{\partial c_{N-2}} & \frac{\partial \tilde{R}_{G_{\tilde{N}-2}}}{\partial c_{N-1}} & \frac{\partial \tilde{R}_{G_{\tilde{N}-2}}}{\partial c_N} & \frac{\partial \tilde{R}_{G_{\tilde{N}-2}}}{\partial \delta} & \frac{\partial \tilde{R}_{G_{\tilde{N}-2}}}{\partial u_e} \\ \frac{\partial \tilde{R}_{BC_1}}{\partial c_0} & \cdots & \frac{\partial \tilde{R}_{BC_1}}{\partial c_{N-2}} & \frac{\partial \tilde{R}_{BC_1}}{\partial c_{N-1}} & \frac{\partial \tilde{R}_{BC_1}}{\partial c_N} & \frac{\partial \tilde{R}_{BC_1}}{\partial \delta} & \frac{\partial \tilde{R}_{BC_1}}{\partial u_e} \\ \frac{\partial \tilde{R}_{BC_2}}{\partial c_0} & \cdots & \frac{\partial \tilde{R}_{BC_2}}{\partial c_{N-2}} & \frac{\partial \tilde{R}_{BC_2}}{\partial c_{N-1}} & \frac{\partial \tilde{R}_{BC_2}}{\partial c_N} & \frac{\partial \tilde{R}_{BC_2}}{\partial \delta} & \frac{\partial \tilde{R}_{BC_2}}{\partial u_e} \end{bmatrix}, \tag{6.20}$$

$$\mathbf{D} = \begin{bmatrix} \frac{\partial \tilde{R}_{G_0}}{\partial d_0} & \cdots & \frac{\partial \tilde{R}_{G_0}}{\partial d_{\tilde{N}-2}} & \frac{\partial \tilde{R}_{G_0}}{\partial d_{\tilde{N}-1}} & \frac{\partial \tilde{R}_{G_0}}{\partial d_{\tilde{N}}} \\ \vdots & \ddots & \vdots & \vdots & \vdots \\ \frac{\partial \tilde{R}_{G_{\tilde{N}-2}}}{\partial d_0} & \cdots & \frac{\partial \tilde{R}_{G_{\tilde{N}-2}}}{\partial d_{\tilde{N}-2}} & \frac{\partial \tilde{R}_{G_{\tilde{N}-2}}}{\partial d_{\tilde{N}-1}} & \frac{\partial \tilde{R}_{G_{\tilde{N}-2}}}{\partial d_{\tilde{N}}} \\ \frac{\partial \tilde{R}_{BC_1}}{\partial d_0} & \cdots & \frac{\partial \tilde{R}_{BC_1}}{\partial d_{\tilde{N}-2}} & \frac{\partial \tilde{R}_{BC_1}}{\partial d_{\tilde{N}-1}} & \frac{\partial \tilde{R}_{BC_1}}{\partial d_{\tilde{N}}} \\ \frac{\partial \tilde{R}_{BC_2}}{\partial d_0} & \cdots & \frac{\partial \tilde{R}_{BC_2}}{\partial d_{\tilde{N}-2}} & \frac{\partial \tilde{R}_{BC_2}}{\partial d_{\tilde{N}-1}} & \frac{\partial \tilde{R}_{BC_2}}{\partial d_{\tilde{N}}} \end{bmatrix}. \tag{6.21}$$

6.7 Discretization

The only term that needs to be discretized is

$$\frac{\partial}{\partial \xi}(u\tilde{\nu}) = \frac{\partial}{\partial \xi}(U u_i \tilde{\nu}) = u_i \frac{\partial}{\partial \xi}(U\tilde{\nu}) + U\tilde{\nu}\frac{du_i}{d\xi} \approx u_{i_2}\frac{U_2\tilde{\nu}_2 - U_1\tilde{\nu}_1}{\xi_2 - \xi_1} + U_2\tilde{\nu}_2\frac{u_{i_2}}{\xi_2}\frac{\ln\left(\frac{u_{i_2}}{u_{i_1}}\right)}{\ln\left(\frac{\xi_2}{\xi_1}\right)}, \tag{6.22}$$

which makes use of the logarithmic differencing technique. For the similarity station this term is set to zero.

6.8 Flat Plate

The spectral solution to turbulent flow over a flat plate was computed. The setup was identical to that reported in Chapter 5. In this case, $N = 180$ and $\tilde{N} = 10$.

Figure 6-1 depicts the velocity, eddy viscosity, and shear stress profiles at $\xi = 1$ m which corresponds to $\mathrm{Re}_\theta \approx 10^4$. Note that u has been normalized with u_e, ν_t with $0.025 u_e \delta^*$, and τ with τ_w. The main feature of this plot is the abruptness with which the eddy viscosity goes to zero near the edge of the boundary layer. This makes it difficult to resolve the working variable $\tilde{\nu}$.

Figure 6-2 compares the velocity profile to the velocity construction using Spalding's law of the wall [39] and Coles' law of the wake [6]. The log law has also been plotted for historical reasons. Despite the spectral solution being slightly higher in the buffer region (due to arguments in the modeling of the eddy viscosity), the comparison is quite good.

Figure 6-3 illustrates the eddy viscosity budget in the boundary layer. All the plots were normalized with $0.1\tau_w$. The production, diffusion, and destruction are defined by

$$\text{Production} \equiv c_{b1}\tilde{S}\tilde{\nu}, \tag{6.23a}$$

$$\text{Diffusion} \equiv \frac{1}{\sigma}\frac{4}{\delta^2}\left\{\frac{\partial}{\partial\eta}\left[(\nu+\tilde{\nu})\frac{\partial\tilde{\nu}}{\partial\eta}\right]+c_{b2}\left(\frac{\partial\tilde{\nu}}{\partial\eta}\right)^2\right\}, \tag{6.23b}$$

$$\text{Destruction} \equiv -c_{w1}f_w\frac{4}{\delta^2}\left(\frac{\tilde{\nu}}{\eta+1}\right)^2, \tag{6.23c}$$

where the sum is simply the addition of these terms (or the convection terms in the transport equation). Notice that the oscillation present in the diffusion term is due to the difficulty in resolving $\tilde{\nu}$, as described previously.

Figure 6-4 illustrates the convergence rate of the series coefficients on a log-linear plot at $\xi = 1$ m. This plot is typical of coefficients which oscillate with N (see Boyd [2]). However, the convergence is not exponential primarily due to a lack of smoothness for u rather than integration error.

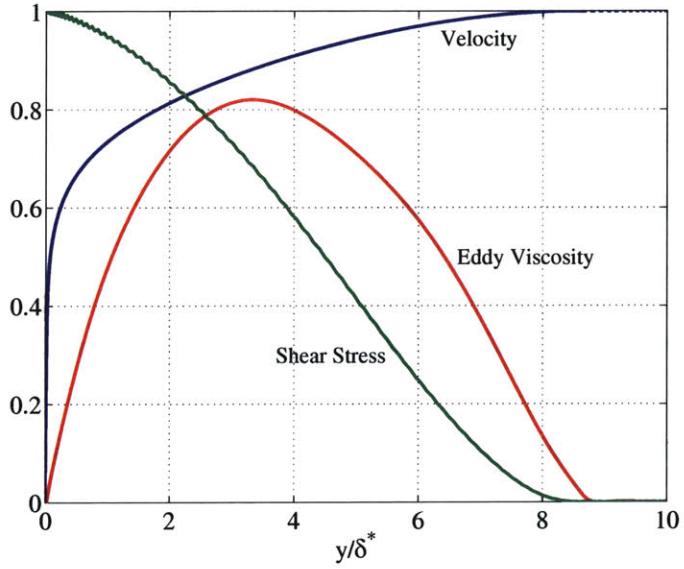

Figure 6-1: Turbulent flat plate: Various profiles at $\mathrm{Re}_\theta \approx 10^4$.

6.9 Wall Function

6.9.1 Modified Viscous Streamwise Velocity

The viscous streamwise velocity $u(\xi,\eta)$ defined on $\xi \in (0,\infty)$ and $\eta \in [-1,1]$ is modified by including an inner layer velocity profile, $u_\tau(\xi)\,u_{+S}(y_+)$, or wall function (WF) in its truncated series expansion approximation given by

$$u(\xi,\eta) \approx u_N(\xi,\eta) = u_e(\xi)\sum_{k=0}^{N} c_k(\xi)\,T_k(\eta) + u_\tau(\xi)\,u_{+S}(y_+), \tag{6.24}$$

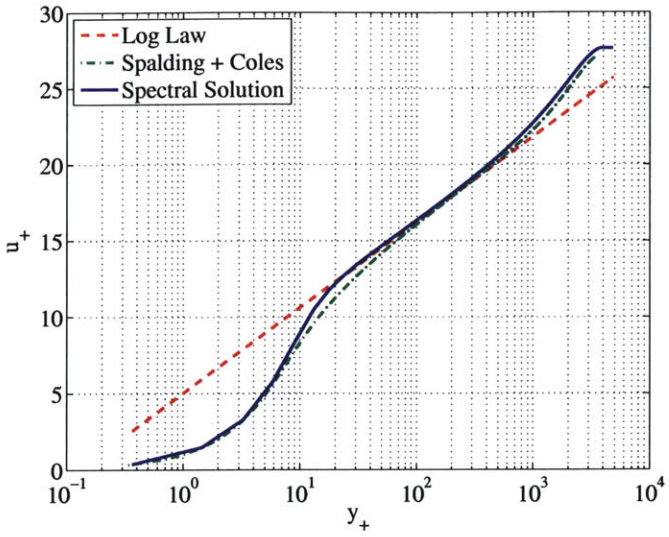

Figure 6-2: Turbulent flat plate: u_+ vs. y_+ at $\mathrm{Re}_\theta \approx 10^4$.

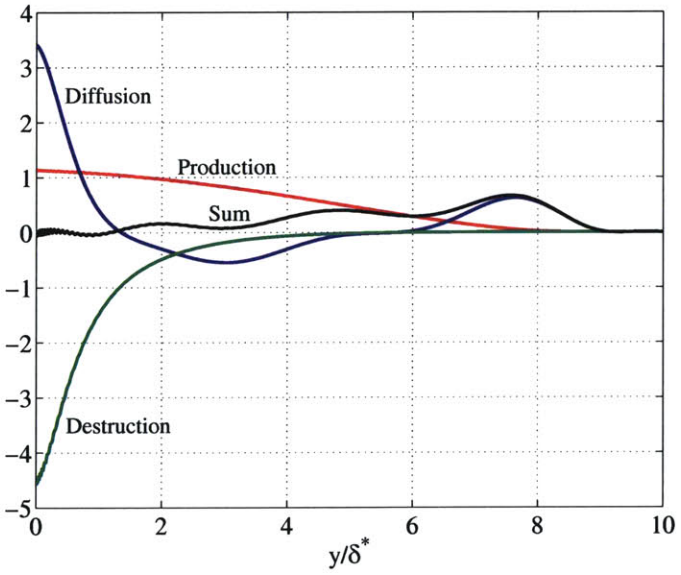

Figure 6-3: Turbulent flat plate: Eddy viscosity budget at $\mathrm{Re}_\theta \approx 10^4$.

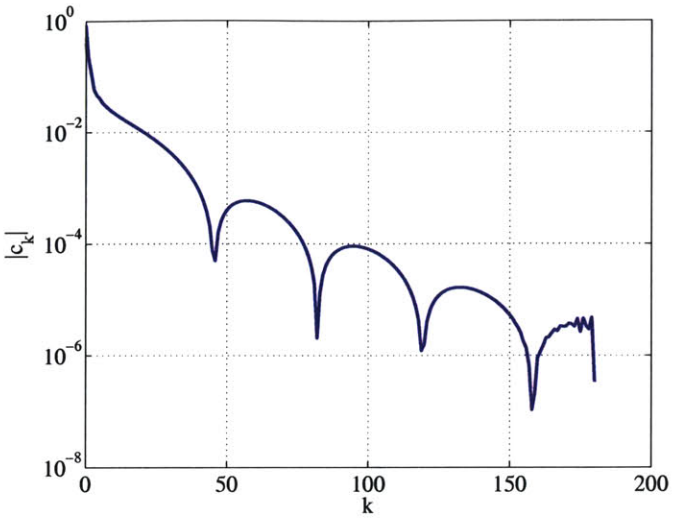

Figure 6-4: Turbulent flat plate: $|c_k|$ vs. k at $\xi = 1$ m.

where $u_e(\xi)$ is the edge velocity (streamwise component), $c_k(\xi)$ are the series coefficients, the chosen basis functions $T_k(\eta)$ are the Chebyshev polynomials, $u_\tau(\xi)$ is the friction velocity, and $u_{+_S}(y_+)$ is Spalding's law of the wall [39].

6.9.2 Friction Velocity Constraint

The friction velocity $u_\tau(\xi)$ is a new unknown and it must be constrained accordingly. The residual

$$R_{u_\tau}(x) = \int_0^\delta (u_S - u)\, w_{u_\tau} dy = 0, \tag{6.25}$$

or equivalently,

$$R_{u_\tau}(\xi) = \frac{\delta}{2} \int_{-1}^{1} (u_S - u)\, w_{u_\tau} d\eta = 0, \tag{6.26}$$

ensures that the velocity profile in the inner layer is only approximated by Spalding's law of the wall. Note that $u_S = u_\tau u_{+_S}$ and w_{u_τ} is given by

$$\ln w_{u_\tau} = -\left[\frac{K\Delta\nu_t}{u_e\delta}\right]^2 \qquad \text{with} \qquad \Delta\nu_t = \nu_{t_i} - \nu_t. \tag{6.27}$$

The constant $K = 1000$, ν_{t_i} is the inner layer eddy viscosity model based on Spalding's law of the wall [39], ν_t is the eddy viscosity computed from the Spalart-Allmaras model, u_e is the edge velocity, and δ is the boundary layer thickness. Figure 6-5 plots ν_{t_i} and ν_t depicting the region near the wall where they are almost equivalent. Figure 6-6 demonstrates the expected Gaussian behavior of w_{u_τ}.

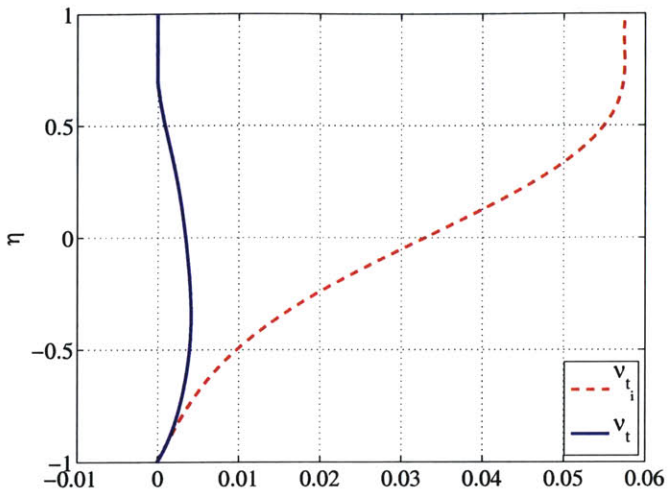

Figure 6-5: Graph of ν_{t_i} and ν_t.

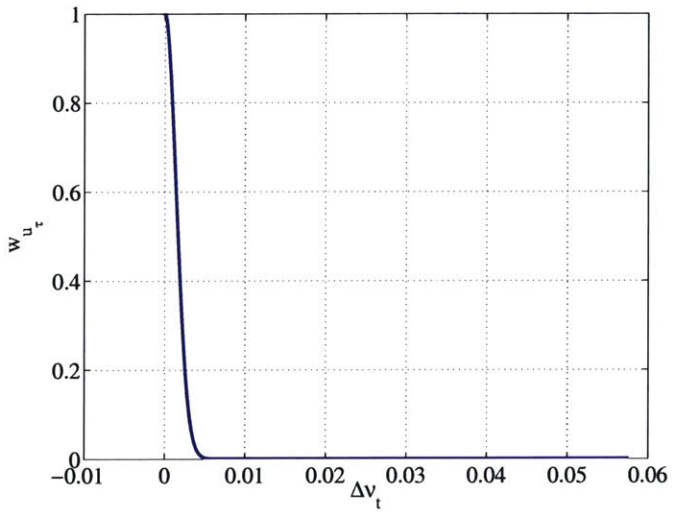

Figure 6-6: Graph of w_{u_τ} vs. $\Delta\nu_t$.

6.9.3 Modified Newton System

The vector of equations $\mathbf{F}$ will consist of the $N-1$ Galerkin equations R_G, the two boundary conditions, R_{BC_1} and R_{BC_2}, the three constraint equations, R_{u_τ}, R_δ, and R_{u_e}, the $\tilde{N}-1$ Galerkin equations $\tilde{R}_G$, and the two boundary conditions, $\tilde{R}_{BC_1}$ and $\tilde{R}_{BC_2}$. The vector of unknowns $\mathbf{U}$ will contain the $N+1$ series coefficients c_k, the friction velocity u_τ, the boundary layer thickness δ, the edge velocity u_e, and the $\tilde{N}+1$ series coefficients d_k. These vectors are given by

$$\mathbf{F} = \begin{bmatrix} R_{G_0} \\ \vdots \\ R_{G_{N-2}} \\ R_{BC_1} \\ R_{BC_2} \\ R_{u_\tau} \\ R_\delta \\ R_{u_e} \\ \tilde{R}_{G_0} \\ \vdots \\ \tilde{R}_{G_{\tilde{N}-2}} \\ \tilde{R}_{BC_1} \\ \tilde{R}_{BC_2} \end{bmatrix} \quad \text{and} \quad \mathbf{U} = \begin{bmatrix} c_0 \\ \vdots \\ c_{N-2} \\ c_{N-1} \\ c_N \\ u_\tau \\ \delta \\ u_e \\ d_0 \\ \vdots \\ d_{\tilde{N}-2} \\ d_{\tilde{N}-1} \\ d_{\tilde{N}} \end{bmatrix}. \tag{6.28}$$

The Jacobian matrix $[\partial\mathbf{F}/\partial\mathbf{U}]$ will be an $\left(N+\tilde{N}+5\right) \times \left(N+\tilde{N}+5\right)$ matrix of the form

$$\left[\frac{\partial \mathbf{F}}{\partial \mathbf{U}}\right] = \begin{bmatrix} \mathbf{A} & \mathbf{B} \\ \mathbf{C} & \mathbf{D} \end{bmatrix}, \tag{6.29}$$

where the matrices $\mathbf{A}$, $\mathbf{B}$, $\mathbf{C}$, and $\mathbf{D}$ are given by

$$\mathbf{A} = \begin{bmatrix} \frac{\partial R_{G_0}}{\partial c_0} & \cdots & \frac{\partial R_{G_0}}{\partial c_{N-2}} & \frac{\partial R_{G_0}}{\partial c_{N-1}} & \frac{\partial R_{G_0}}{\partial c_N} & \frac{\partial R_{G_0}}{\partial u_\tau} & \frac{\partial R_{G_0}}{\partial \delta} & \frac{\partial R_{G_0}}{\partial u_e} \\ \vdots & \ddots & \vdots & \vdots & \vdots & \vdots & \vdots & \vdots \\ \frac{\partial R_{G_{N-2}}}{\partial c_0} & \cdots & \frac{\partial R_{G_{N-2}}}{\partial c_{N-2}} & \frac{\partial R_{G_{N-2}}}{\partial c_{N-1}} & \frac{\partial R_{G_{N-2}}}{\partial c_N} & \frac{\partial R_{G_{N-2}}}{\partial u_\tau} & \frac{\partial R_{G_{N-2}}}{\partial \delta} & \frac{\partial R_{G_{N-2}}}{\partial u_e} \\ \frac{\partial R_{BC_1}}{\partial c_0} & \cdots & \frac{\partial R_{BC_1}}{\partial c_{N-2}} & \frac{\partial R_{BC_1}}{\partial c_{N-1}} & \frac{\partial R_{BC_1}}{\partial c_N} & \frac{\partial R_{BC_1}}{\partial u_\tau} & \frac{\partial R_{BC_1}}{\partial \delta} & \frac{\partial R_{BC_1}}{\partial u_e} \\ \frac{\partial R_{BC_2}}{\partial c_0} & \cdots & \frac{\partial R_{BC_2}}{\partial c_{N-2}} & \frac{\partial R_{BC_2}}{\partial c_{N-1}} & \frac{\partial R_{BC_2}}{\partial c_N} & \frac{\partial R_{BC_2}}{\partial u_\tau} & \frac{\partial R_{BC_2}}{\partial \delta} & \frac{\partial R_{BC_2}}{\partial u_e} \\ \frac{\partial R_{u_\tau}}{\partial c_0} & \cdots & \frac{\partial R_{u_\tau}}{\partial c_{N-2}} & \frac{\partial R_{u_\tau}}{\partial c_{N-1}} & \frac{\partial R_{u_\tau}}{\partial c_N} & \frac{\partial R_{u_\tau}}{\partial u_\tau} & \frac{\partial R_{u_\tau}}{\partial \delta} & \frac{\partial R_{u_\tau}}{\partial u_e} \\ \frac{\partial R_\delta}{\partial c_0} & \cdots & \frac{\partial R_\delta}{\partial c_{N-2}} & \frac{\partial R_\delta}{\partial c_{N-1}} & \frac{\partial R_\delta}{\partial c_N} & \frac{\partial R_\delta}{\partial u_\tau} & \frac{\partial R_\delta}{\partial \delta} & \frac{\partial R_\delta}{\partial u_e} \\ \frac{\partial R_{u_e}}{\partial c_0} & \cdots & \frac{\partial R_{u_e}}{\partial c_{N-2}} & \frac{\partial R_{u_e}}{\partial c_{N-1}} & \frac{\partial R_{u_e}}{\partial c_N} & \frac{\partial R_{u_e}}{\partial u_\tau} & \frac{\partial R_{u_e}}{\partial \delta} & \frac{\partial R_{u_e}}{\partial u_e} \end{bmatrix}, \tag{6.30}$$

$$\mathbf{B} = \begin{bmatrix} \frac{\partial R_{G_0}}{\partial d_0} & \cdots & \frac{\partial R_{G_0}}{\partial d_{\tilde{N}-2}} & \frac{\partial R_{G_0}}{\partial d_{\tilde{N}-1}} & \frac{\partial R_{G_0}}{\partial d_{\tilde{N}}} \\ \vdots & \ddots & \vdots & \vdots & \vdots \\ \frac{\partial R_{G_{N-2}}}{\partial d_0} & \cdots & \frac{\partial R_{G_{N-2}}}{\partial d_{\tilde{N}-2}} & \frac{\partial R_{G_{N-2}}}{\partial d_{\tilde{N}-1}} & \frac{\partial R_{G_{N-2}}}{\partial d_{\tilde{N}}} \\ \frac{\partial R_{BC_1}}{\partial d_0} & \cdots & \frac{\partial R_{BC_1}}{\partial d_{\tilde{N}-2}} & \frac{\partial R_{BC_1}}{\partial d_{\tilde{N}-1}} & \frac{\partial R_{BC_1}}{\partial d_{\tilde{N}}} \\ \frac{\partial R_{BC_2}}{\partial d_0} & \cdots & \frac{\partial R_{BC_2}}{\partial d_{\tilde{N}-2}} & \frac{\partial R_{BC_2}}{\partial d_{\tilde{N}-1}} & \frac{\partial R_{BC_2}}{\partial d_{\tilde{N}}} \\ \frac{\partial R_{u_\tau}}{\partial d_0} & \cdots & \frac{\partial R_{u_\tau}}{\partial d_{\tilde{N}-2}} & \frac{\partial R_{u_\tau}}{\partial d_{\tilde{N}-1}} & \frac{\partial R_{u_\tau}}{\partial d_{\tilde{N}}} \\ \frac{\partial R_\delta}{\partial d_0} & \cdots & \frac{\partial R_\delta}{\partial d_{\tilde{N}-2}} & \frac{\partial R_\delta}{\partial d_{\tilde{N}-1}} & \frac{\partial R_\delta}{\partial d_{\tilde{N}}} \\ \frac{\partial R_{u_e}}{\partial d_0} & \cdots & \frac{\partial R_{u_e}}{\partial d_{\tilde{N}-2}} & \frac{\partial R_{u_e}}{\partial d_{\tilde{N}-1}} & \frac{\partial R_{u_e}}{\partial d_{\tilde{N}}} \end{bmatrix}, \tag{6.31}$$

$$\mathbf{C} = \begin{bmatrix} \frac{\partial \tilde{R}_{G_0}}{\partial c_0} & \cdots & \frac{\partial \tilde{R}_{G_0}}{\partial c_{N-2}} & \frac{\partial \tilde{R}_{G_0}}{\partial c_{N-1}} & \frac{\partial \tilde{R}_{G_0}}{\partial c_N} & \frac{\partial \tilde{R}_{G_0}}{\partial u_\tau} & \frac{\partial \tilde{R}_{G_0}}{\partial \delta} & \frac{\partial \tilde{R}_{G_0}}{\partial u_e} \\ \vdots & \ddots & \vdots & \vdots & \vdots & \vdots & \vdots & \vdots \\ \frac{\partial \tilde{R}_{G_{\tilde{N}-2}}}{\partial c_0} & \cdots & \frac{\partial \tilde{R}_{G_{\tilde{N}-2}}}{\partial c_{N-2}} & \frac{\partial \tilde{R}_{G_{\tilde{N}-2}}}{\partial c_{N-1}} & \frac{\partial \tilde{R}_{G_{\tilde{N}-2}}}{\partial c_N} & \frac{\partial \tilde{R}_{G_{N-2}}}{\partial u_\tau} & \frac{\partial \tilde{R}_{G_{\tilde{N}-2}}}{\partial \delta} & \frac{\partial \tilde{R}_{G_{\tilde{N}-2}}}{\partial u_e} \\ \frac{\partial \tilde{R}_{BC_1}}{\partial c_0} & \cdots & \frac{\partial \tilde{R}_{BC_1}}{\partial c_{N-2}} & \frac{\partial \tilde{R}_{BC_1}}{\partial c_{N-1}} & \frac{\partial \tilde{R}_{BC_1}}{\partial c_N} & \frac{\partial \tilde{R}_{BC_1}}{\partial u_\tau} & \frac{\partial \tilde{R}_{BC_1}}{\partial \delta} & \frac{\partial \tilde{R}_{BC_1}}{\partial u_e} \\ \frac{\partial \tilde{R}_{BC_2}}{\partial c_0} & \cdots & \frac{\partial \tilde{R}_{BC_2}}{\partial c_{N-2}} & \frac{\partial \tilde{R}_{BC_2}}{\partial c_{N-1}} & \frac{\partial \tilde{R}_{BC_2}}{\partial c_N} & \frac{\partial \tilde{R}_{BC_2}}{\partial u_\tau} & \frac{\partial \tilde{R}_{BC_2}}{\partial \delta} & \frac{\partial \tilde{R}_{BC_2}}{\partial u_e} \end{bmatrix}, \tag{6.32}$$

$$\mathbf{D} = \begin{bmatrix} \frac{\partial \tilde{R}_{G_0}}{\partial d_0} & \cdots & \frac{\partial \tilde{R}_{G_0}}{\partial d_{\tilde{N}-2}} & \frac{\partial \tilde{R}_{G_0}}{\partial d_{\tilde{N}-1}} & \frac{\partial \tilde{R}_{G_0}}{\partial d_{\tilde{N}}} \\ \vdots & \ddots & \vdots & \vdots & \vdots \\ \frac{\partial \tilde{R}_{G_{\tilde{N}-2}}}{\partial d_0} & \cdots & \frac{\partial \tilde{R}_{G_{\tilde{N}-2}}}{\partial d_{\tilde{N}-2}} & \frac{\partial \tilde{R}_{G_{\tilde{N}-2}}}{\partial d_{\tilde{N}-1}} & \frac{\partial \tilde{R}_{G_{\tilde{N}-2}}}{\partial d_{\tilde{N}}} \\ \frac{\partial \tilde{R}_{BC_1}}{\partial d_0} & \cdots & \frac{\partial \tilde{R}_{BC_1}}{\partial d_{\tilde{N}-2}} & \frac{\partial \tilde{R}_{BC_1}}{\partial d_{\tilde{N}-1}} & \frac{\partial \tilde{R}_{BC_1}}{\partial d_{\tilde{N}}} \\ \frac{\partial \tilde{R}_{BC_2}}{\partial d_0} & \cdots & \frac{\partial \tilde{R}_{BC_2}}{\partial d_{\tilde{N}-2}} & \frac{\partial \tilde{R}_{BC_2}}{\partial d_{\tilde{N}-1}} & \frac{\partial \tilde{R}_{BC_2}}{\partial d_{\tilde{N}}} \end{bmatrix}. \tag{6.33}$$

6.10 Flat Plate Revisited

The spectral solution to turbulent flow over a flat plate was computed with the incorporation of the wall function. The setup was identical to that reported in Chapter 5. In this case, $N = 4$ and $\tilde{N} = 10$.

Figure 6-7 depicts the velocity, eddy viscosity, and shear stress profiles at $\xi = 1$ m which corresponds to $\mathrm{Re}_\theta \approx 10^4$. Once again, u has been normalized with u_e, ν_t with $0.025 u_e \delta^*$, and τ with τ_w. The two main features of this plot are the abruptness with which the eddy viscosity goes to zero near the edge of the boundary layer and the overshoot in the shear stress near the wall. The former feature has already been discussed whereas the latter is due to the inconsistency between the wall function and the turbulence model within the inner layer.

Figure 6-8 compares the velocity profile to the velocity construction using Spalding's law of the wall [39] and Coles' law of the wake [6]. The log law has also been plotted for historical reasons. The spectral solution matches up perfectly since the velocity was constrained to equal Spalding's law of the wall in the inner layer. The fact that the wake also matches up very well is mere coincidence.

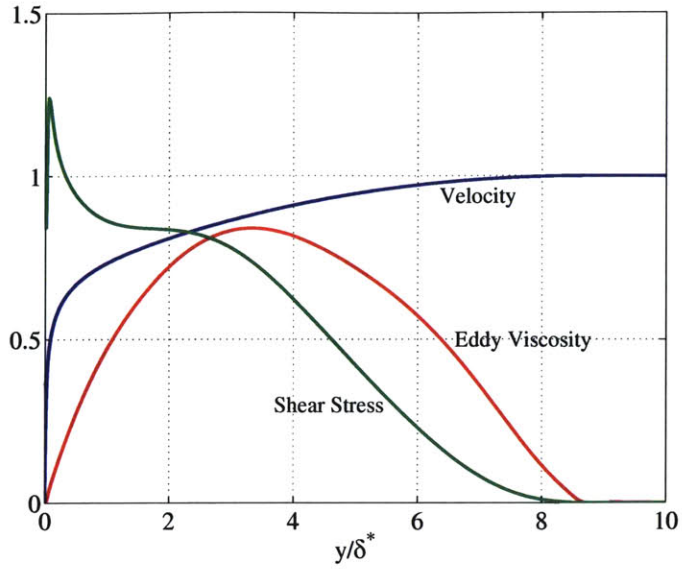

Figure 6-7: Turbulent flat plate (WF): Various profiles at $\mathrm{Re}_\theta \approx 10^4$.

Figure 6-9 illustrates the eddy viscosity budget in the boundary layer. All the plots were normalized with $0.1\tau_w$. The production, diffusion, and destruction terms have already been defined where the sum is simply the addition of these terms (or the convection terms in the transport equation). Again, the oscillation present in the diffusion term is due to the difficulty in resolving $\tilde{\nu}$. The production and destruction terms are erroneous near the wall since they both depend on the velocity gradient (i.e. S).

Figure 6-10 breaks down the velocity profile into its two contributions. In these plots, $\eta = 2y/\delta - 1$. It is reassuring to observe that the Chebyshev profile is zero (on the average) in the inner layer following the constraint equation R_{u_τ}. This allows the Spalding profile to approximate the velocity near the wall. In the outer layer, the Chebyshev profile corrects the velocity approximation as required to solve the flow.

The velocity gradient and shear stress contributions are depicted in Figures 6-11 and 6-12. Once again, $\eta = 2y/\delta - 1$. The Chebyshev contribution has little effect on the overall $\partial u/\partial \eta$. The laminar component of the shear stress $\tau_l = \mu\,(\partial u/\partial \eta)$ scales the velocity gradient by the dynamic viscosity. Conversely, the turbulent component $\tau_t = \mu_t\,(\partial u/\partial \eta)$ utilizes the eddy viscosity as a scaling factor which varies with the location inside the boundary layer. Since the wall function is not consistent with the inner layer eddy viscosity model, the shear stress exhibits a large oscillation near the wall. The shear stress at the edge approaches zero smoothly as reflected by the eddy viscosity behavior at this location.

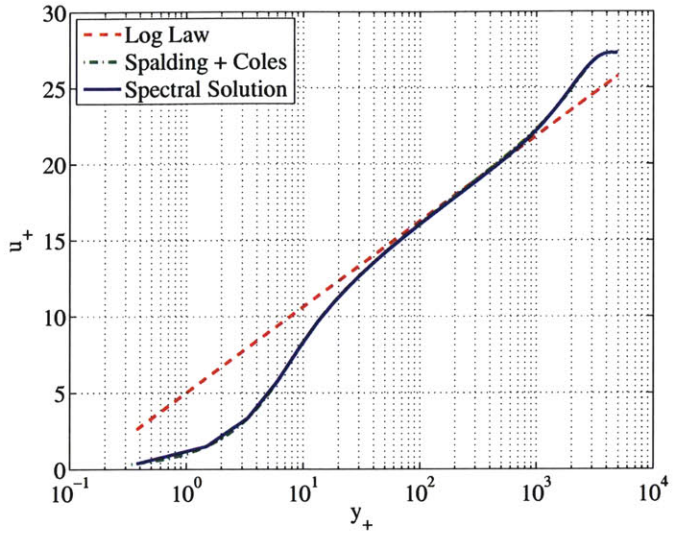

Figure 6-8: Turbulent flat plate (WF): u_+ vs. y_+ at $\mathrm{Re}_\theta \approx 10^4$.

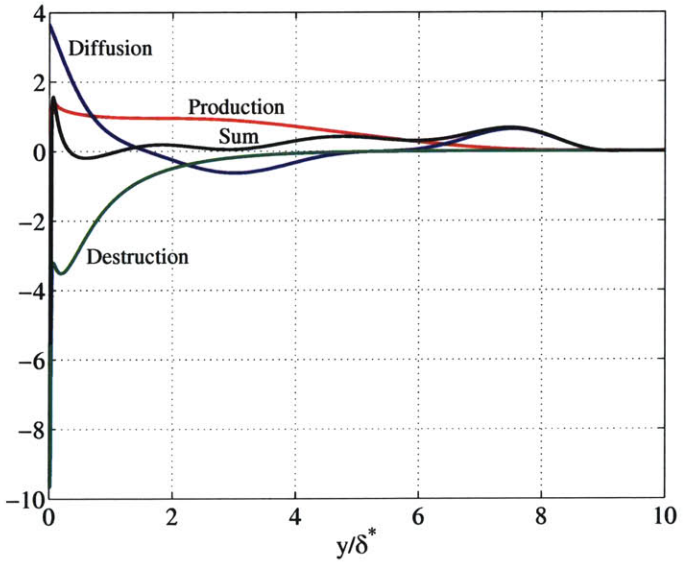

Figure 6-9: Turbulent flat plate (WF): Eddy viscosity budget at $\mathrm{Re}_\theta \approx 10^4$.

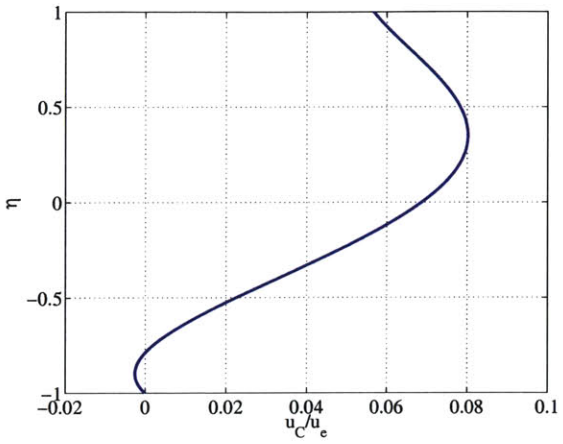

(a) Chebyshev

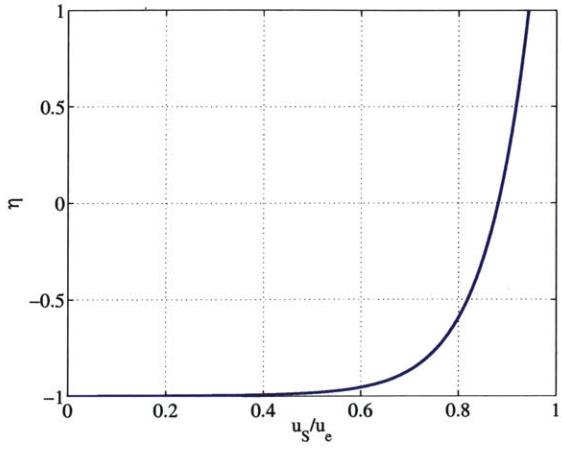

(b) Spalding

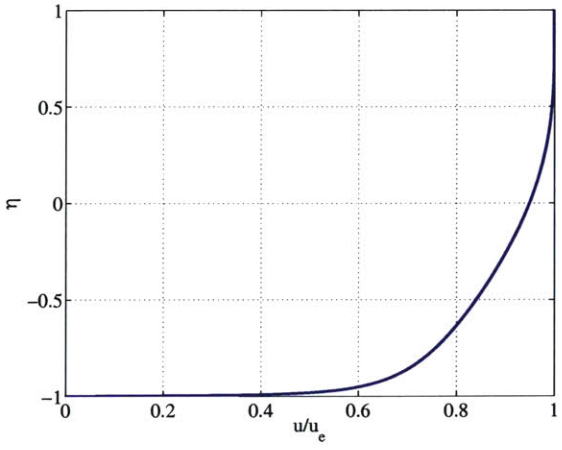

(c) Total

Figure 6-10: Velocity profile contributions (WF).

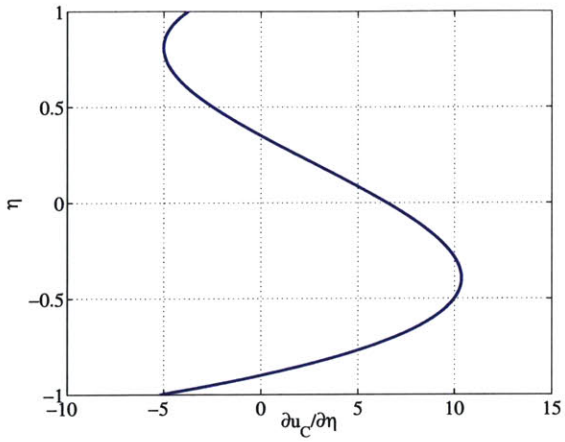

(a) Chebyshev

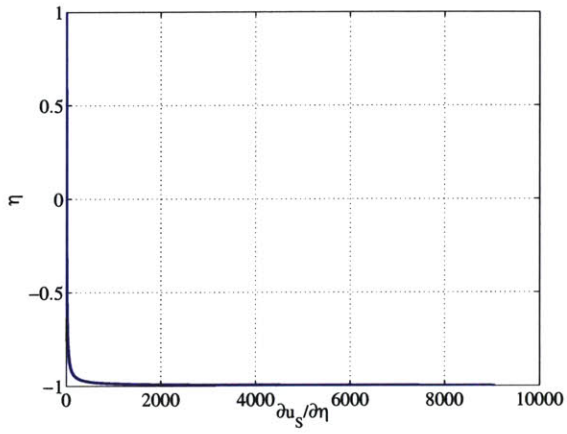

(b) Spalding

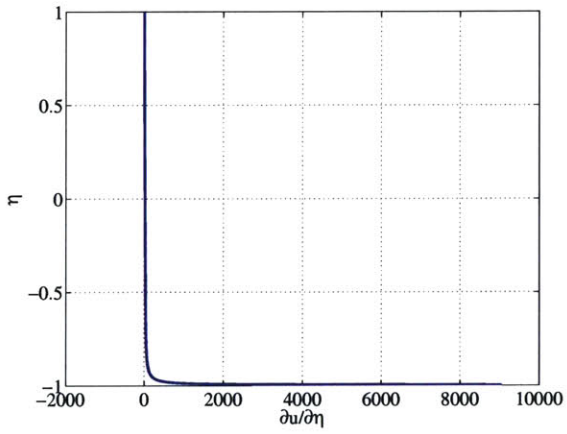

(c) Total

Figure 6-11: Velocity gradient contributions (WF).

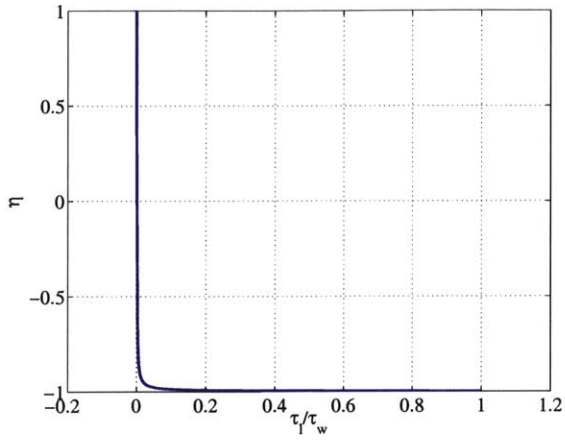

(a) Laminar

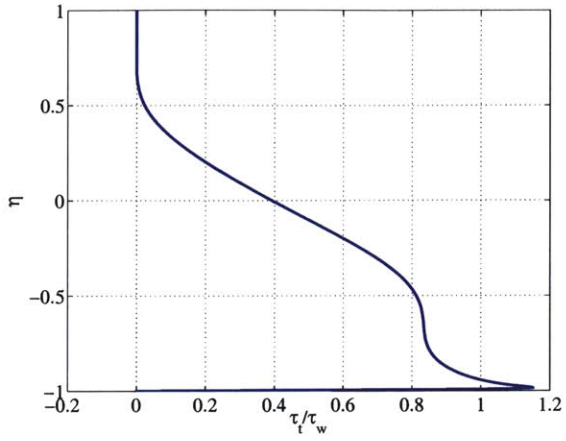

(b) Turbulent

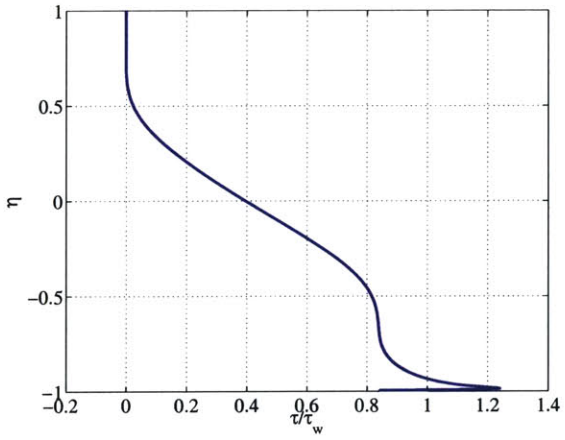

(c) Total

Figure 6-12: Shear stress contributions (WF).

Chapter 7

Conclusion

7.1 Summary

Due to the current inability of the MISES quasi 3-D design/analysis code to handle the the boundary layer problem with flow control via blowing, two alternate approaches were proposed. First, a two-equation integral method parameterized with the profile parameters of a multi-deck representation of a turbulent jet based on Coles' law of the wake was formulated. The appearance of spurious singularities in the Jacobian matrices associated with the system of equations and the vector of unknowns prevented this method from being implemented. Second, a Chebyshev spectral method using the wall function technique was applied to the defect form of the incompressible viscous momentum equation. A turbulent jet profile was computed with $N = 40$ modes, a number low enough to allow the method's implementation into the MISES framework.

The following summarizes the main points of the thesis.

- An integral method parameterized with the profile parameters of a multi-deck representation of a turbulent jet based on Coles' law of the wake was proposed. The blowing model does a fairly good job in approximating experimental jet profile data. Consequently, the dimensionless form of both the von Kármán integral momentum equation and the integral Kinetic Energy (KE) equation were derived for each layer with the closure relations modeled in terms of the profile parameters. It was discovered that the Jacobian matrices associated with the system of equations and the vector of unknowns have spurious singularities. Conversely, applying the model to a wake profile and using the integral approach yields a well-constrained system. Therefore, the application of the integral boundary layer method to compute a multi-deck representation of a turbulent jet profile is inherently difficult.

- The Galerkin form of the Chebyshev spectral method was presented and applied to curve-fit experimental jet profiles. It was found that the outer layer in these profiles could be approximated with $N = 20$ modes. The near-wall region, in which high velocity gradients exist, could potentially be resolved using an appropriate wall function.

- The spectral method formulated with the defect form of the incompressible viscous momentum equation was developed to solve laminar flow over a flat plate with boundary layer control via suction or blowing.

- For the case of no flow control, the Falkner-Skan family of boundary layer similarity solutions, of which the flow over a flat plate is but one special case, were used for comparison purposes. With $N = 10$, the spectral method was in close agreement with the Falkner-Skan solution. The exponential convergence rate of the series coefficients was shown on a log-linear plot.
- Similar flow can also be maintained on a porous flat plate with vertical suction/blowing if the wall velocity varies as the inverse of the square root of the distance along the wall. The no-slip condition is still enforced and the results differ according to the suction-blowing parameter. Suction thins the boundary layer and increases the slope at the wall. Conversely, blowing thickens the boundary layer and makes the profile S-shaped. In all case, $N = 30$.
- Uniform suction results in the flow being nonsimilar changing from the laminar flat plate profile at the leading edge to the asymptotic exponential profile far downstream. The velocity and shear stress profiles obtained from the spectral method exhibit the theoretical exponential shapes and the flow evolution clearly indicates the asymptotic behavior. In this case, $N = 10$.
- The laminar jet was setup on a flat plate with an inclined slot. The jet angle is deduced from the slot geometry. Utilizing a jet strength of 0.38, with the velocity profile inside the slot modeled as the Poiseuille parabola, the resulting velocity and shear stress profiles were indicative of fluid injection. In this case, $N = 30$. The displacement and momentum thicknesses demonstrated the excess mass and momentum in the boundary layer due to fluid injection. This case also points out some of the difficulties in treating the blowing problem with traditional integral boundary layer methods.

- The spectral method applied to turbulent flow is analogous to the formulation for laminar flow with the only complication being the modeling of the Reynolds stress in the momentum equation. An algebraic model for the eddy viscosity based on Spalding's law of the wall for the inner layer and Clauser's outer layer formulation was implemented in the spectral method.

  - The spectral solution to turbulent flow over a flat plate with no flow control was computed. Due to the two-layer structure of the boundary layer, the number of modes needed to be increased to $N = 180$. The velocity profile was in close agreement with an accurate representation constructed from Spalding's law of the wall and Coles' law of the wake. The shear stress does not quite go to zero at the edge since the eddy viscosity has a nonzero value in the outer layer. The convergence rate of the series coefficients is not exponential primarily due to a lack of smoothness in the velocity approximation rather than integration error.
  - The incorporation of a wall function, consistent with the inner layer eddy viscosity model, into the approximation of the streamwise velocity reduced the number of modes to $N = 4$. Comparison of the turbulent flat plate results with and without the wall function are almost identical.
  - For a flat plate with wall suction or blowing the inner eddy viscosity model was modified due to the profound effect that the wall velocity has on the shear distribution. The spectral solution was computed with $N = 180$ and compared to the Stevenson correlation. The agreement was excellent. The wall function was

then modified to match the new eddy viscosity model in the inner layer. Using $N = 4$ the resulting solution compared favorably to the Stevenson correlation.

  - The turbulent jet problem required a modification to the outer layer eddy viscosity model because Clauser's formulation uses the displacement thickness which can become negative for a strong enough jet. The setup was identical to the laminar jet but the flow was tripped to become turbulent five slot lengths downstream of the slot. Once again. $N = 180$. The convergence rate of the series coefficients is not exponential for the same reasons as in the flat plate case. Incorporating a wall function reduces the number of modes to $N = 40$ to obtain a close a match to the velocity and shear stress profiles for $N = 180$.

- The turbulent flow over a flat plate was also solved using the Spalart-Allmaras turbulence model. For the working variable in this model, $\tilde{N} = 10$. The resulting velocity profile compares favorably to the accurate representation constructed from Spalding's law of the wall and Coles' law of the wake with $N = 180$. The convergence rate of the series coefficients is not exponential primarily due to a lack of smoothness in the velocity approximation rather than integration error. Incorporating the wall function based on Spalding's law of the wall and computing the solution with $N = 4$ yields an erroneous shear stress near the wall due to the small inconsistency between the Spalding velocity and the Spalart-Allmaras eddy viscosity.

7.2 Recommendations for Future Work

The following are suggestions for improvements based on some shortcomings encountered in the methodology:

- A more accurate integration scheme should be employed when higher resolution is required. A Gauss-Legendre quadrature scheme is suggested since it is the most accurate. The only difficulty is in the evaluation of integrals whose limits change, such as in the viscous normal velocity component.

- The constraint on the boundary layer thickness should be replaced with a differential equation based on the local velocity profile. This would avoid situations in which the velocity profile is forced to zero over a large percentage of the boundary layer. The effect would be a substantial reduction in the number of required modes.

- The Spalart-Allmaras turbulence model for the eddy viscosity should be modified to match the inner layer eddy viscosity model based on Spalding's law of the wall. This would require replacing the functional weight on the working variable.

Appendix A

Falkner-Skan Wedge Flows

The most celebrated family of similarity solutions for boundary layer flow was discovered by Falkner and Skan [13] and later computed numerically by Hartree [16]. This class of solutions have the property that the velocity profiles, u, at different streamwise locations, x, can be made congruent with suitable scaling factors for u and y (the normal flow coordinate). The partial differential equations (PDEs) governing the flow reduce to one simple ordinary differential equation (ODE). This appendix derives the ODE and presents the numerical results for a range of wedge flows. In addition, the spectral solution to some of the more interesting wedge flows are listed.

A.1 Boundary Layer Equations in Streamfunction Variables

The 2-D, steady, incompressible continuity and x-momentum thin shear layer equations governing the real viscous flow (RVF) in the laminar regime are given by

$$\frac{\partial u}{\partial x} + \frac{\partial v}{\partial y} = 0, \tag{A.1}$$

$$\frac{\partial}{\partial x}\left(u^2\right) + \frac{\partial}{\partial y}\left(uv\right) + \frac{1}{\rho}\frac{\partial p}{\partial x} - \frac{1}{\rho}\frac{\partial \tau}{\partial y} = 0. \tag{A.2}$$

In these expressions, u and v are, respectively, the x- and y-components of the RVF velocity; ρ is the mass density; p is the static pressure and τ is the shear stress given by

$$\tau = \mu\frac{\partial u}{\partial y}, \tag{A.3}$$

where μ is the dynamic viscosity. Defining a streamfunction variable, ψ, such that

$$u = \frac{\partial \psi}{\partial y} \qquad \text{and} \qquad \frac{\tau}{\rho} = \nu\frac{\partial u}{\partial y}, \tag{A.4}$$

where the kinematic viscosity $\nu = \mu/\rho$, the RVF x-momentum equation reduces to

$$\frac{\partial \psi}{\partial y}\frac{\partial u}{\partial x} - \frac{\partial \psi}{\partial x}\frac{\partial u}{\partial y} = u_e\frac{du_e}{dx} + \frac{\partial\left(\tau/\rho\right)}{\partial y}. \tag{A.5}$$

The pressure gradient term has been written in terms of the edge velocity u_e (streamwise component). This comes from the assumption that in a boundary layer

$$p(x,y) \approx p(x) = p_e(x), \tag{A.6}$$

where $p_e(x)$ is the static pressure at the edge and using Bernoulli, it can be shown that

$$\frac{dp_e}{dx} = -\rho_e u_e \frac{du_e}{dx}. \tag{A.7}$$

The edge density $\rho_e = \rho$ since the flow is incompressible. The boundary conditions at $y = 0$ are

$$\psi = 0 \qquad \text{and} \qquad u = 0, \tag{A.8}$$

whereas at $y = y_e$,

$$u = u_e, \tag{A.9}$$

where y_e denotes the edge location.

A.2 Coordinate Transformation

The coordinate transformation $(x, y) \rightarrow (\xi, \eta)$ is given by

$$\xi = x, \tag{A.10}$$

$$\eta = \frac{y}{\Delta(x)}, \tag{A.11}$$

where $\Delta(x)$ is an appropriate length scale for the thickness of the boundary layer. The partial derivatives transform to

$$\frac{\partial}{\partial x} = \frac{\partial}{\partial \xi} - \frac{\eta}{\Delta}\frac{d\Delta}{d\xi}\frac{\partial}{\partial \eta}, \tag{A.12}$$

$$\frac{\partial}{\partial y} = \frac{1}{\Delta}\frac{\partial}{\partial \eta}. \tag{A.13}$$

Noting that

$$u\Delta = \frac{\partial \psi}{\partial \eta} \qquad \text{and} \qquad \frac{\tau}{\rho}\Delta = \nu\frac{\partial u}{\partial \eta}, \tag{A.14}$$

the RVF x-momentum equation becomes

$$\frac{\partial \psi}{\partial \eta}\frac{\partial u}{\partial \xi} - \frac{\partial \psi}{\partial \xi}\frac{\partial u}{\partial \eta} = u_e \Delta \frac{du_e}{d\xi} + \frac{\partial(\tau/\rho)}{\partial \eta}. \tag{A.15}$$

A.3 Variable Transformation

The variable transformation $(\psi, u, \tau) \rightarrow (F, U, S)$ is given by

$$\psi = mF, \qquad u = u_e U, \qquad \text{and} \qquad \frac{\tau}{\rho} = \frac{m u_e}{\xi} S. \tag{A.16}$$

Defining

$$m(\xi) \equiv u_e(\xi)\,\Delta(\xi), \qquad \beta_m \equiv \frac{\xi}{m}\frac{dm}{d\xi}, \qquad \text{and} \qquad \beta_u \equiv \frac{\xi}{u_e}\frac{du_e}{d\xi}, \tag{A.17}$$

and noting that

$$U = \frac{\partial F}{\partial \eta} \qquad \text{and} \qquad S = \frac{\nu \xi u_e}{m^2}\frac{\partial U}{\partial \eta} = \frac{\nu \xi}{u_e \Delta^2}\frac{\partial U}{\partial \eta}, \tag{A.18}$$

the RVF x-momentum equation becomes

$$\frac{\partial S}{\partial \eta} + \beta_m F \frac{\partial U}{\partial \eta} + \beta_u \left(1 - U\frac{\partial F}{\partial \eta}\right) = \xi\left(\frac{\partial F}{\partial \eta}\frac{\partial U}{\partial \xi} - \frac{\partial F}{\partial \xi}\frac{\partial U}{\partial \eta}\right). \tag{A.19}$$

The boundary conditions at $\eta = 0$ are

$$F = 0 \qquad \text{and} \qquad U = 0, \tag{A.20}$$

whereas at $\eta = \eta_e$,

$$U = 1, \tag{A.21}$$

where η_e denotes the edge location in transformed coordinates.

A.4 Requirements for Similarity

For similar flow ($\partial/\partial\xi = 0$), the following conditions must hold:

$$\text{1. } \beta_m, \beta_u = \text{constant in } \xi. \quad \text{2. } \frac{\nu \xi u_e}{m^2} = \text{constant in } \xi. \quad \text{3. BCs} = \text{constant in } \xi. \tag{A.22}$$

The first condition is satisfied if

$$u_e(\xi) = C_e \xi^{\beta_u}, \qquad m(\xi) = C_m \xi^{\beta_m}, \qquad \text{and} \qquad \Delta(\xi) = C_\Delta \xi^{\beta_\Delta}, \tag{A.23}$$

where C_e, C_m, and C_Δ are constants. The second condition will yield the relationship between β_m and β_u, that is

$$\beta_m = \frac{1 + \beta_u}{2}. \tag{A.24}$$

Noting that $m(\xi) \equiv u_e(\xi)\,\Delta(\xi)$, it is a simple matter to deduce

$$\beta_m = \beta_u + \beta_\Delta. \tag{A.25}$$

The third condition is satisfied outright from the previously stated boundary conditions.

A.5 Falkner-Skan Transformation

Falkner and Skan chose the combination

$$\frac{\nu \xi}{u_e \Delta^2} = 1, \tag{A.26}$$

from which the Falkner-Skan length scale, Δ_{FS}, could be defined as

$$\Delta_{\mathrm{FS}} \equiv \Delta(x) = \sqrt{\frac{\nu x}{u_e(x)}}. \tag{A.27}$$

As a result, the RVF x-momentum equation reduces to the ODE

$$\frac{d^3F}{d\eta^3} + \left(\frac{1+\beta_u}{2}\right) F\frac{d^2F}{d\eta^2} + \beta_u\left[1 - \left(\frac{dF}{d\eta}\right)^2\right] = 0. \tag{A.28}$$

The boundary conditions at $\eta = 0$ are

$$F = 0 \qquad \text{and} \qquad \frac{dF}{d\eta} = 0, \tag{A.29}$$

whereas at $\eta \to \infty$,

$$\frac{dF}{d\eta} = 1. \tag{A.30}$$

A.6 Integral Thickness Definitions and Shape Parameter

The displacement and momentum thicknesses, δ^* and θ, are defined as

$$\delta^* \equiv \int_0^\infty \left(1 - \frac{u}{u_e}\right) dy \qquad \text{and} \qquad \theta \equiv \int_0^\infty \left(1 - \frac{u}{u_e}\right)\frac{u}{u_e} dy. \tag{A.31}$$

Applying the Falkner-Skan transformation yields the modified thicknesses

$$\delta^*_{\mathrm{FS}} \equiv \frac{\delta^*}{\Delta_{\mathrm{FS}}} = \int_0^\infty \left(1 - \frac{dF}{d\eta}\right) d\eta \qquad \text{and} \qquad \theta_{\mathrm{FS}} \equiv \frac{\theta}{\Delta_{\mathrm{FS}}} = \int_0^\infty \left(1 - \frac{dF}{d\eta}\right)\frac{dF}{d\eta} d\eta, \tag{A.32}$$

where the subscript FS is used to differentiate between the actual and transformed quantities. The shape parameter, H, defined by

$$H \equiv \frac{\delta^*}{\theta} = \frac{\delta^*_{\mathrm{FS}}}{\theta_{\mathrm{FS}}}, \tag{A.33}$$

indicates the state of the boundary layer. For a favourable pressure gradient, $\beta_u > 0$ and H is small. Conversely, in an adverse pressure gradient, $\beta_u < 0$ and H is large.

A.7 Skin Friction Coefficient

The skin friction is defined by

$$C_f \equiv \frac{\tau_w}{\frac{1}{2}\rho_e u_e^2}, \tag{A.34}$$

where τ_w is the shear stress at the wall, or

$$\tau_w = \mu \left.\frac{\partial u}{\partial y}\right|_{y=0}. \tag{A.35}$$

In Falkner-Skan variables the skin friction is obtained from

$$\left.\frac{d^2F}{d\eta^2}\right|_{\eta=0} = S|_{\eta=0} = \frac{\tau_w}{\rho_e u_e^2}\frac{\xi}{\Delta_{\mathrm{FS}}} = \frac{1}{2}C_f\sqrt{\mathrm{Re}_x}, \tag{A.36}$$

where ξ was replaced by x in the final expression.

A.8 Numerical Solution

The Falkner-Skan ODE can be solved by discretizing the equation with finite differences and implementing a Newton iteration scheme to solve the corresponding set of nonlinear equations. The results have been summarized in Table A.1 and the corresponding velocity profiles are depicted in Figure A-1.

Table A.1: Solutions of the Falkner-Skan equation for various values of β_u.

β_u	$F''(0) \equiv \frac{1}{2}C_f\sqrt{\mathrm{Re}_x}$	$\delta^*_{\mathrm{FS}} \equiv \delta^*\sqrt{u_e/\nu x}$	$\theta_{\mathrm{FS}} \equiv \theta\sqrt{u_e/\nu x}$	H
1	1.23258	0.64791	0.29235	2.216
1/3	0.75745	0.98538	0.42900	2.297
0.1	0.49657	1.34787	0.55660	2.422
0	0.33206	1.72080	0.66412	2.591
-0.01	0.31147	1.78005	0.67892	2.622
-0.05	0.21348	2.11775	0.75147	2.818
-0.0904	0.00478	3.44593	0.86798	3.970

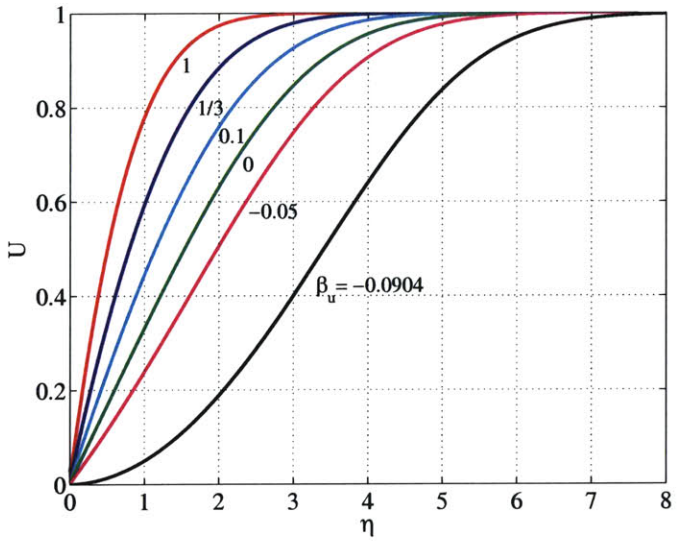

Figure A-1: Falkner-Skan velocity profiles for various values of β_u.

A.9 Spectral Method Results for Wedge Flows

The spectral solution to some of the more interesting wedge flows are listed in Table A.2. In all cases, $N = 10$. For $\beta_u = \{1, 1/3, 0, -0.05, -0.088\}$, the velocity and shear stress profiles as well as detailed flow evolution plots are listed on subsequent pages. In these plots, $\xi = x$ and $\eta = 2y/\delta - 1$.

Table A.2: Spectral solution to wedge flows for various values of β_u.

β_u	$F''(0) \equiv \frac{1}{2}C_f\sqrt{\mathrm{Re}_x}$	$\delta^*_{\mathrm{FS}} \equiv \delta^*\sqrt{u_e/\nu x}$	$\theta_{\mathrm{FS}} \equiv \theta\sqrt{u_e/\nu x}$	H
1	1.23262	0.64751	0.29191	2.218
1/3	0.75746	0.98516	0.42871	2.298
0.1	0.49659	1.34784	0.55646	2.422
0	0.33211	1.72086	0.66401	2.592
-0.01	0.31153	1.78011	0.67881	2.622
-0.05	0.21360	2.11780	0.75130	2.819
-0.088	0.04682	3.05947	0.85775	3.567

A.9.1 Stagnation Flow ($\beta_u = 1$)

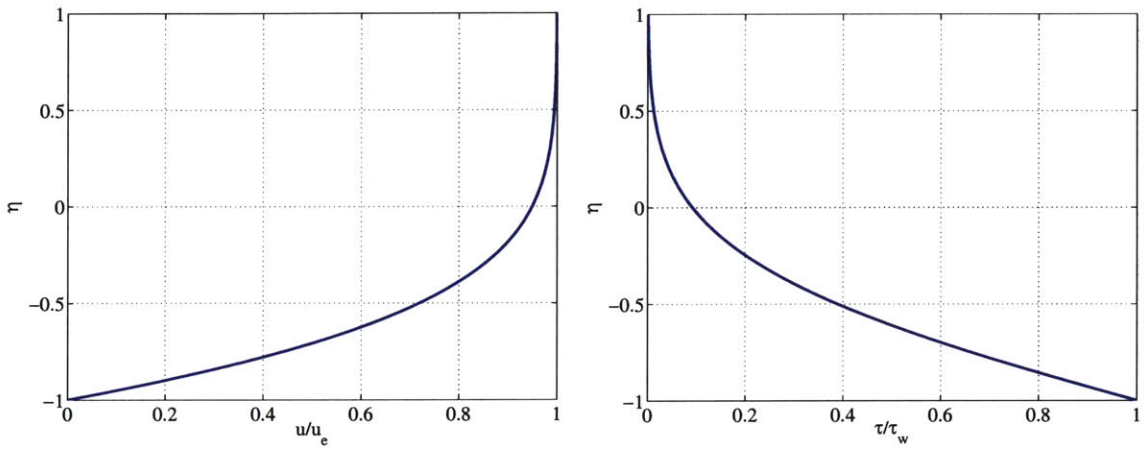

(a) Velocity Profile

(b) Shear Stress Profile

Figure A-2: Stagnation flow: u/u_e and τ/τ_w profiles.

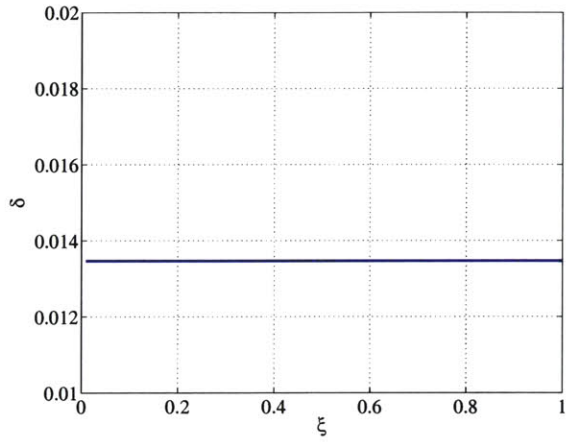

(a) Boundary Layer Thickness

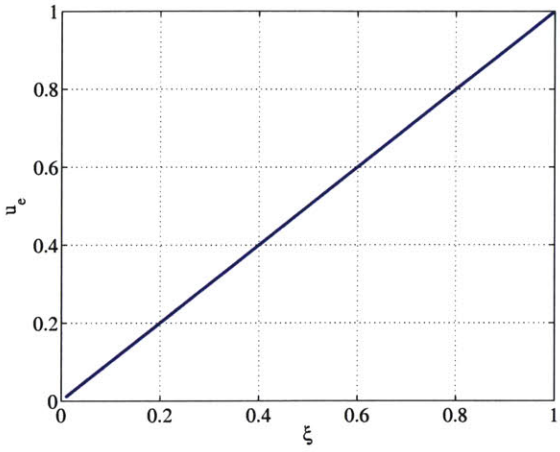

(b) Edge Velocity

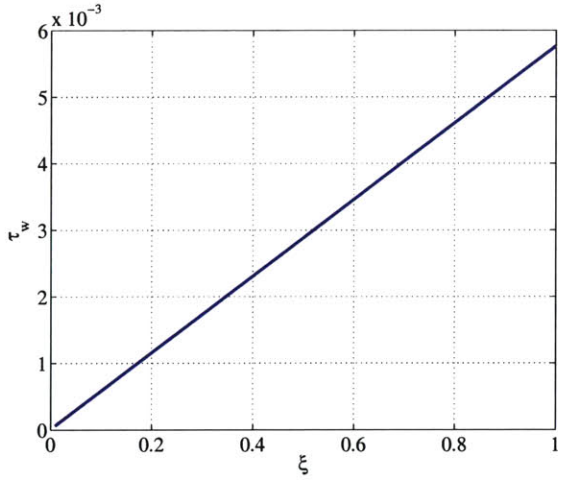

(c) Wall Shear Stress

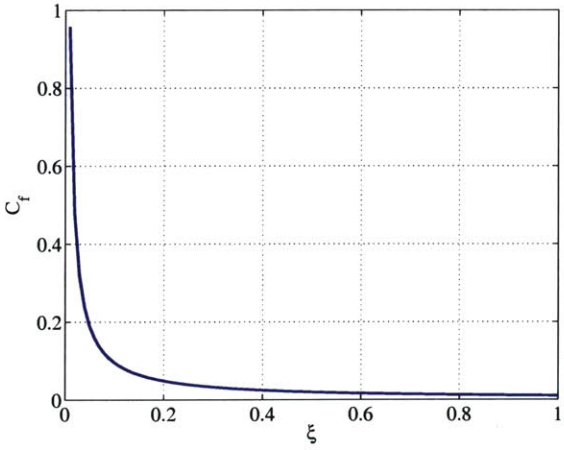

(d) Skin Friction Coefficient

Figure A-3: Stagnation flow: δ, u_e, τ_w, and C_f vs. ξ.

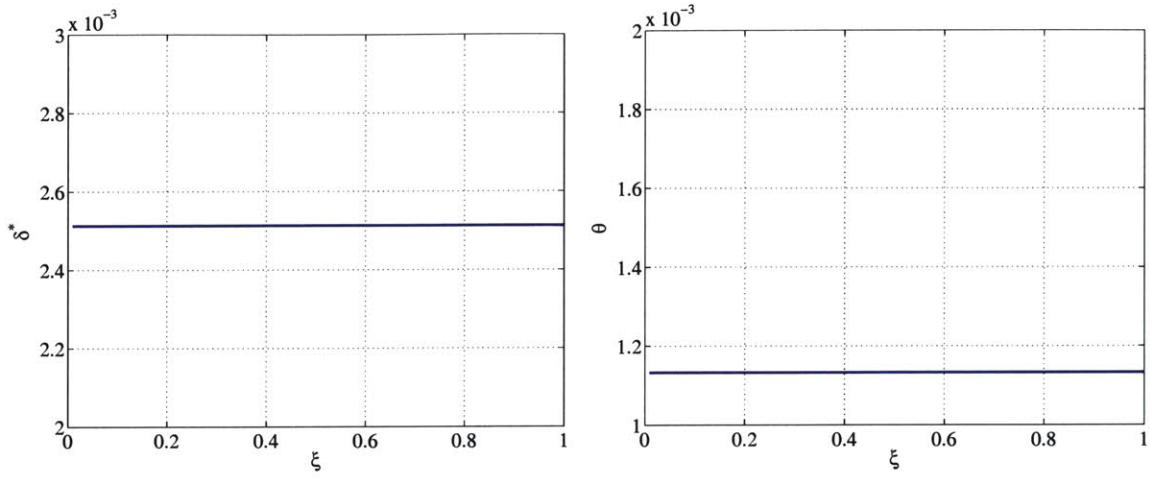

(a) Displacement Thickness

(b) Momentum Thickness

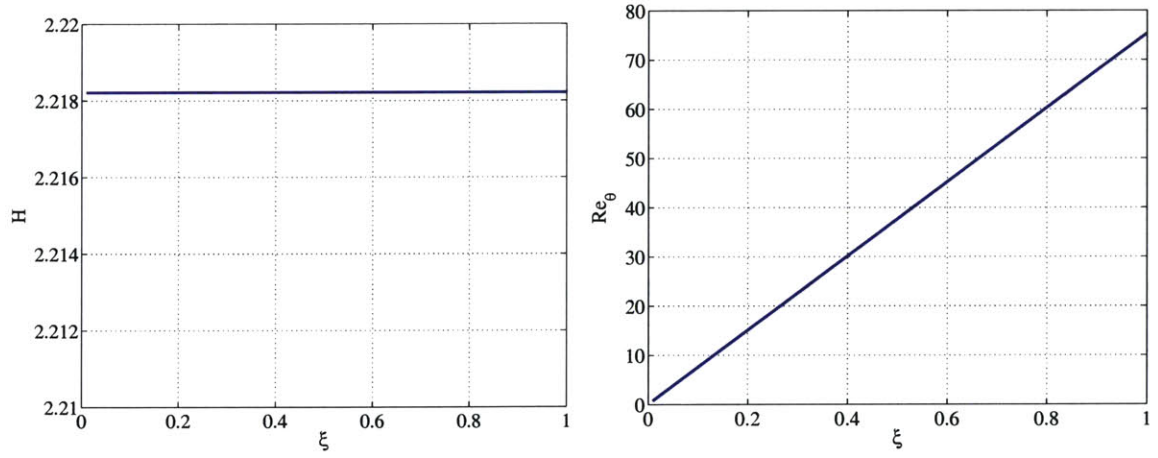

(c) Shape Parameter

(d) Reynolds Number

Figure A-4: Stagnation flow: δ^*, θ, H, and Re_θ vs. ξ.

A.9.2 Constant τ_w ($\beta_u = 1/3$)

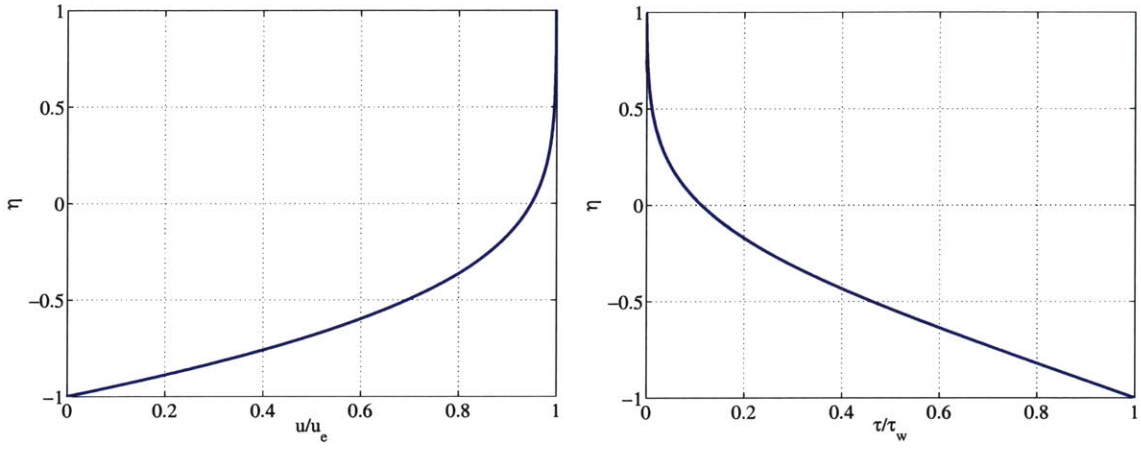

(a) Velocity Profile

(b) Shear Stress Profile

Figure A-5: Constant τ_w: u/u_e and τ/τ_w profiles.

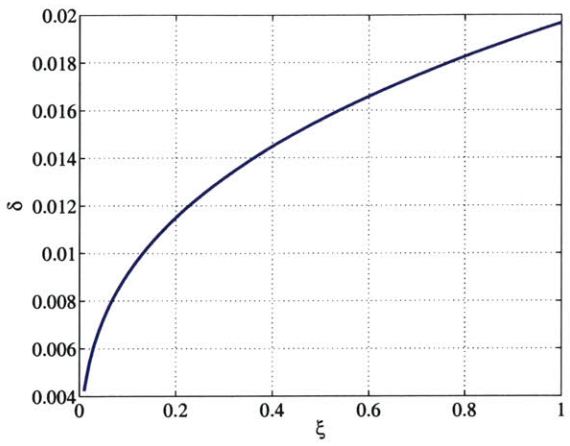

(a) Boundary Layer Thickness

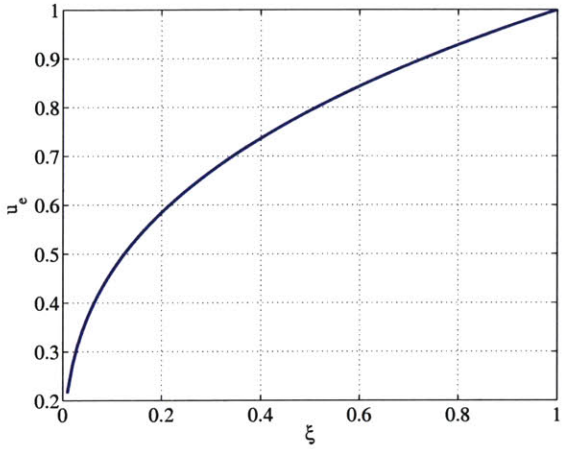

(b) Edge Velocity

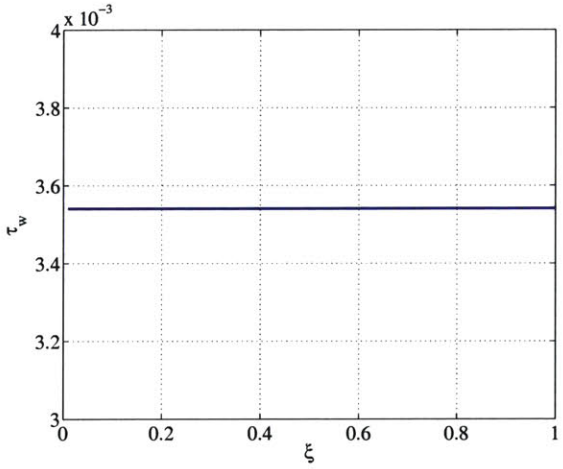

(c) Wall Shear Stress

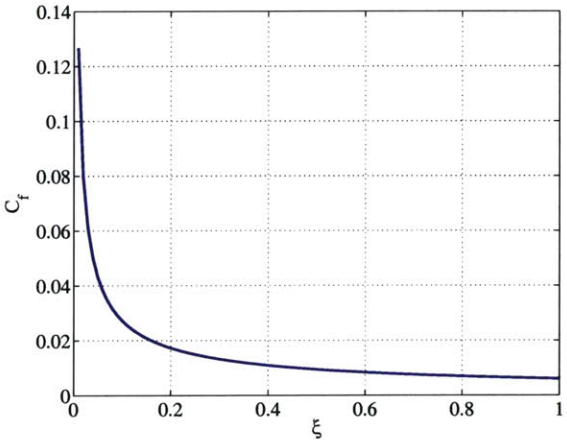

(d) Skin Friction Coefficient

Figure A-6: Constant τ_w: δ, u_e, τ_w, and C_f vs. ξ.

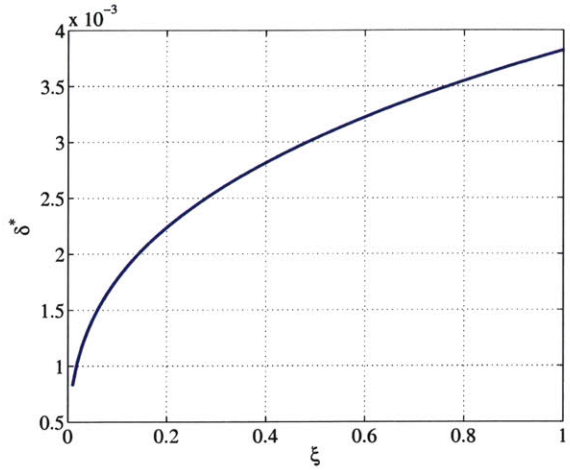

(a) Displacement Thickness

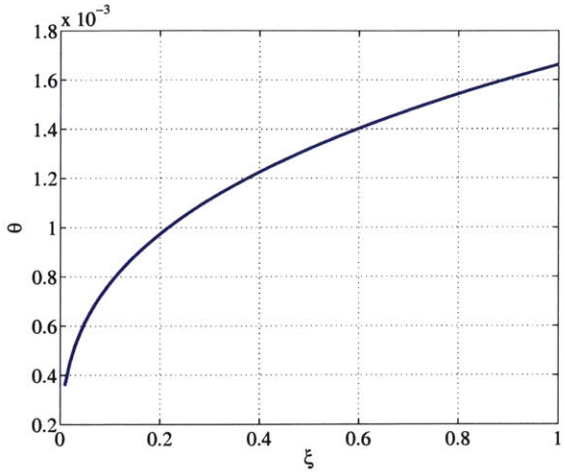

(b) Momentum Thickness

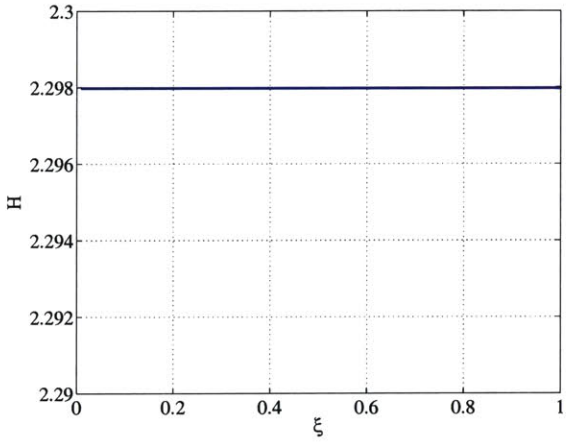

(c) Shape Parameter

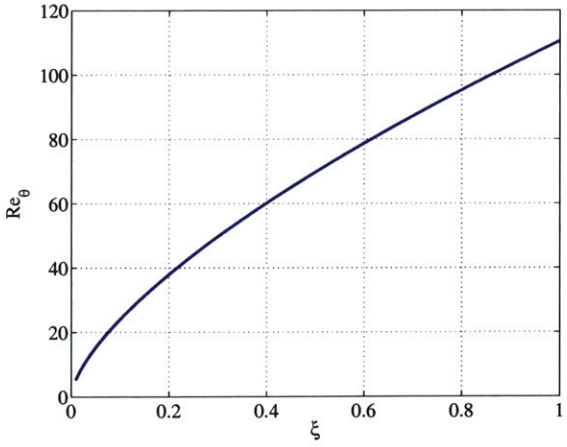

(d) Reynolds Number

Figure A-7: Constant τ_w: δ^*, θ, H, and Re_θ vs. ξ.

A.9.3 Flat Plate ($\beta_u = 0$)

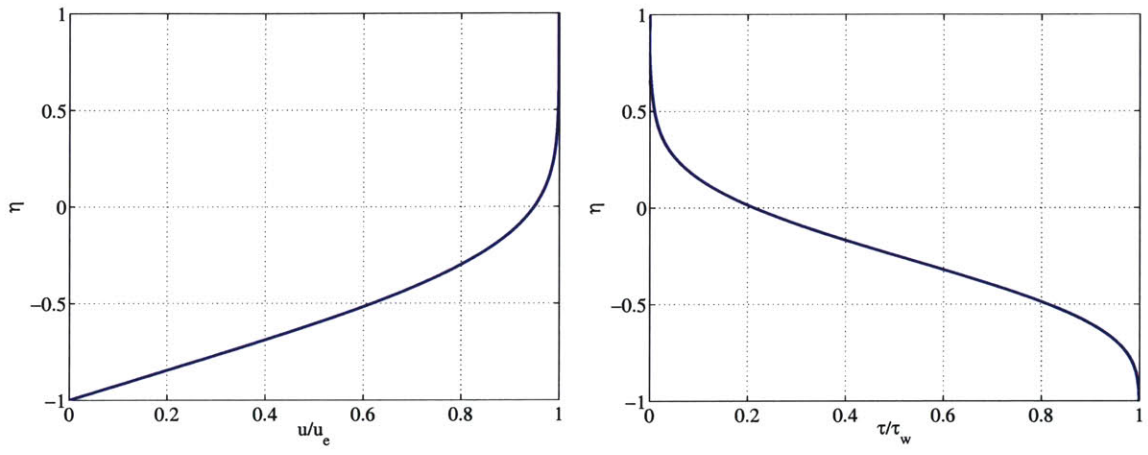

(a) Velocity Profile

(b) Shear Stress Profile

Figure A-8: Laminar flat plate: u/u_e and τ/τ_w profiles.

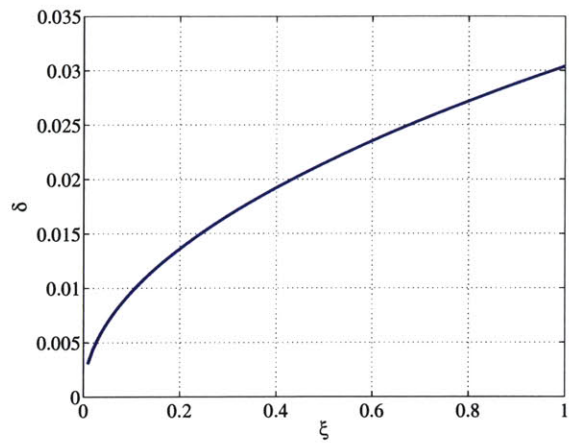

(a) Boundary Layer Thickness

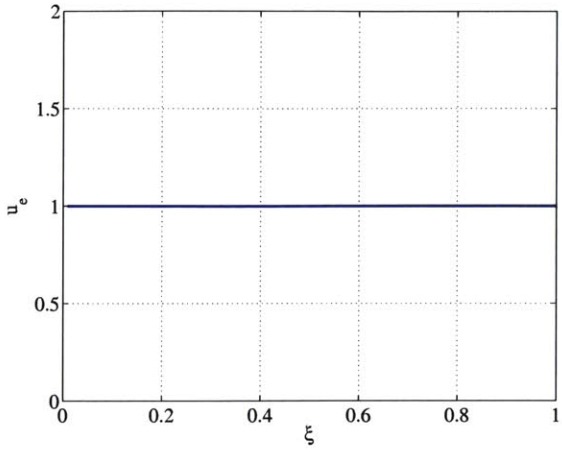

(b) Edge Velocity

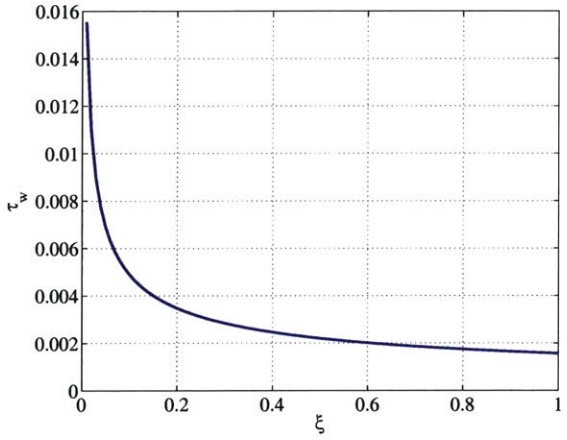

(c) Wall Shear Stress

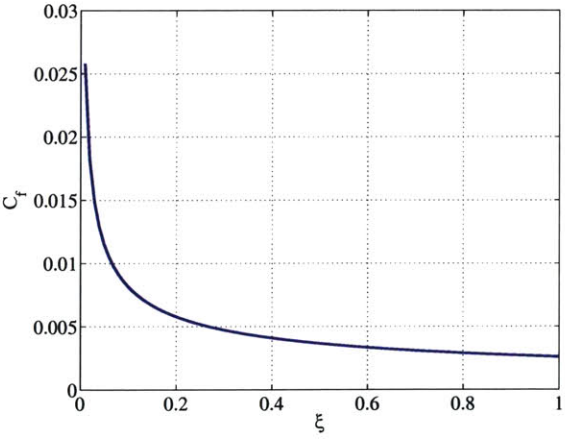

(d) Skin Friction Coefficient

Figure A-9: Laminar flat plate: δ, u_e, τ_w, and C_f vs. ξ.

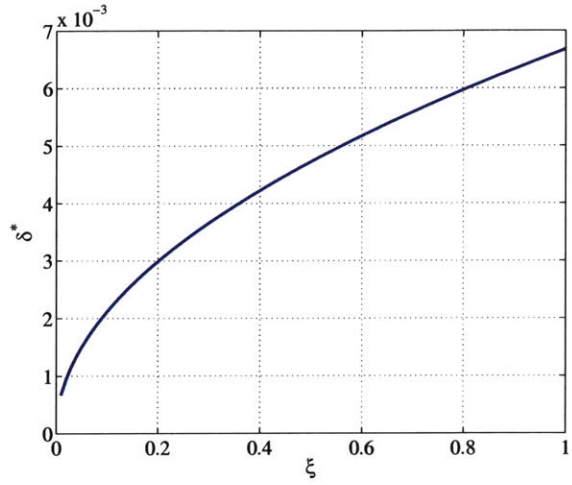

(a) Displacement Thickness

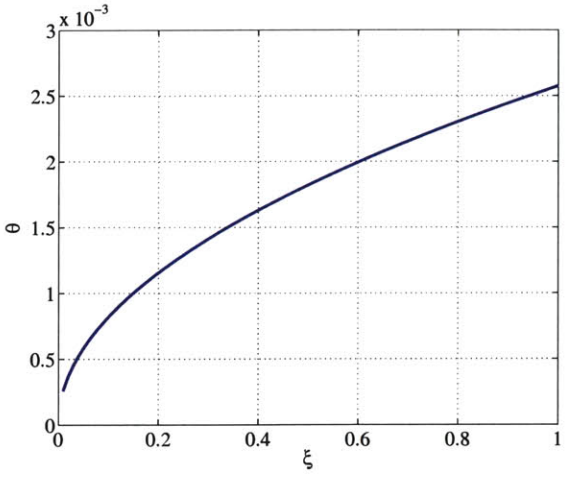

(b) Momentum Thickness

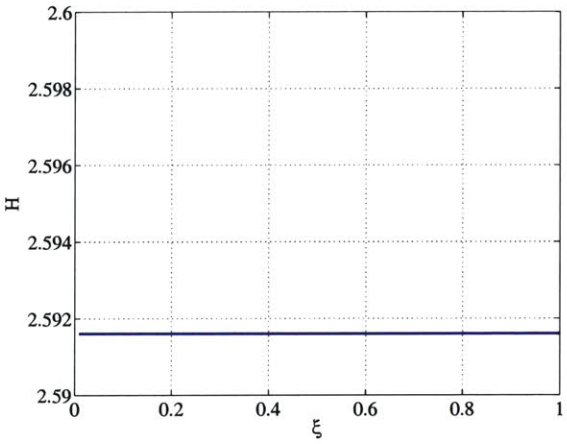

(c) Shape Parameter

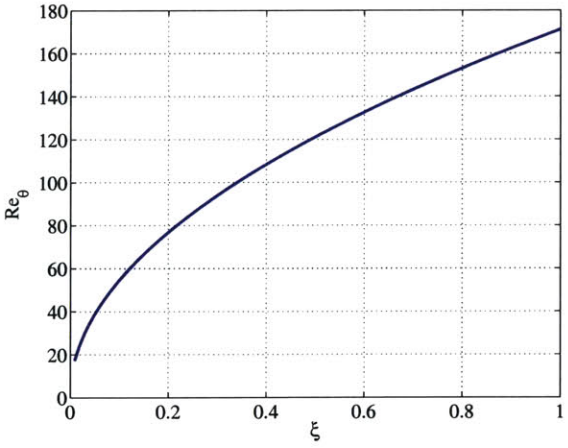

(d) Reynolds Number

Figure A-10: Laminar flat plate: δ^*, θ, H, and Re_θ vs. ξ.

A.9.4 Adverse Pressure Gradient ($\beta_u = -0.05$)

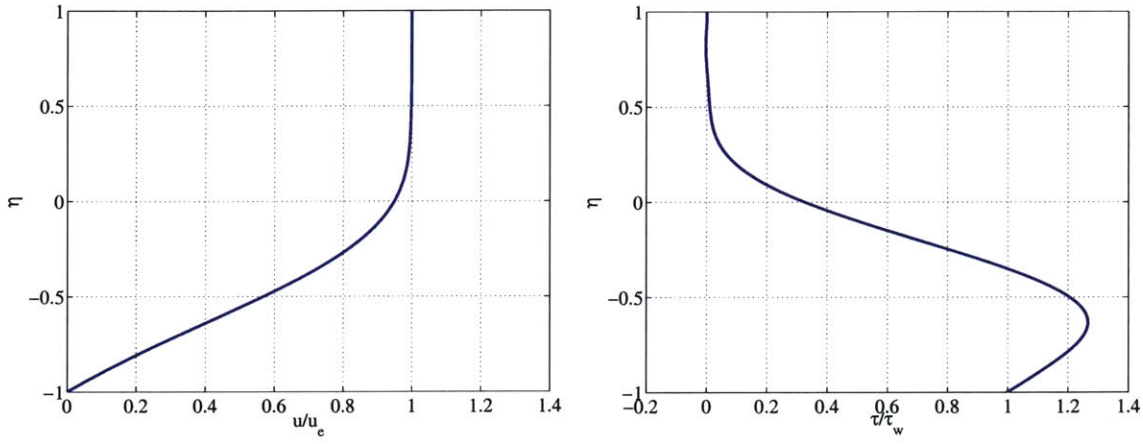

(a) Velocity Profile

(b) Shear Stress Profile

Figure A-11: Adverse pressure gradient: u/u_e and τ/τ_w profiles.

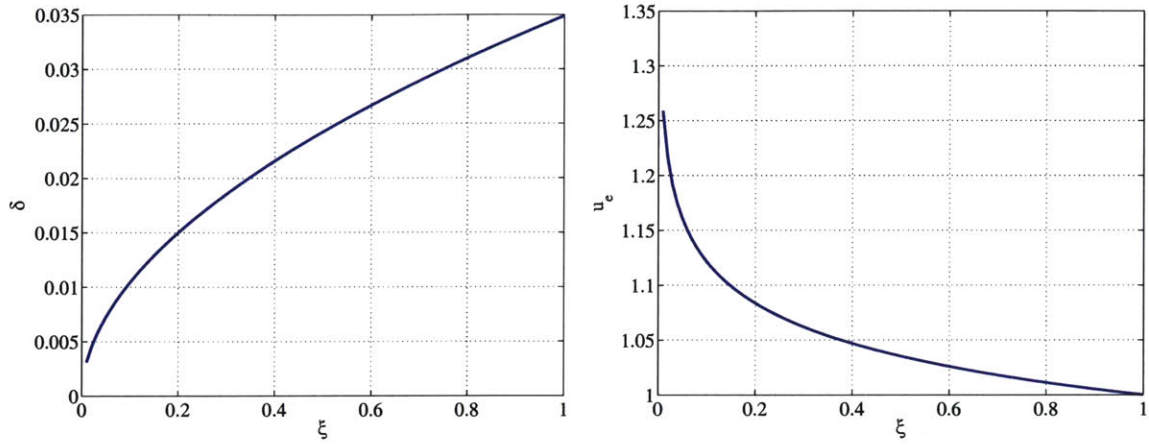

(a) Boundary Layer Thickness

(b) Edge Velocity

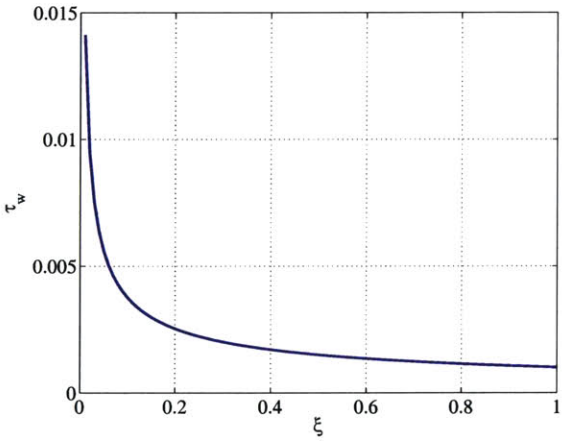

(c) Wall Shear Stress

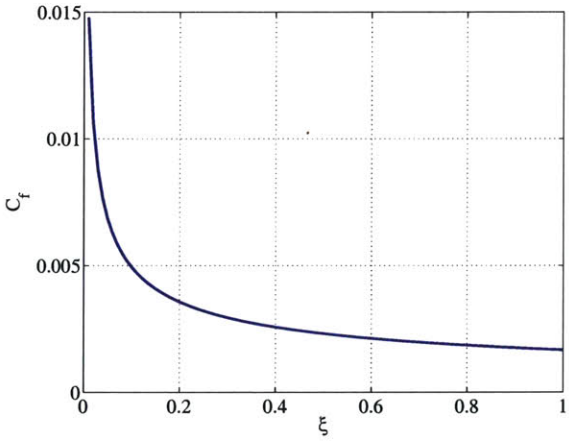

(d) Skin Friction Coefficient

Figure A-12: Adverse pressure gradient: δ, u_e, τ_w, and C_f vs. ξ.

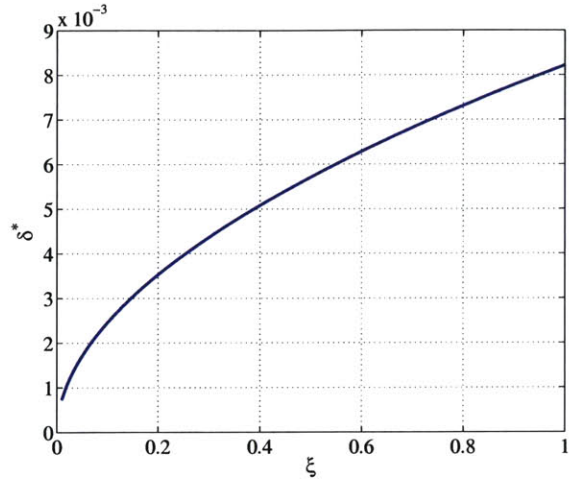

(a) Displacement Thickness

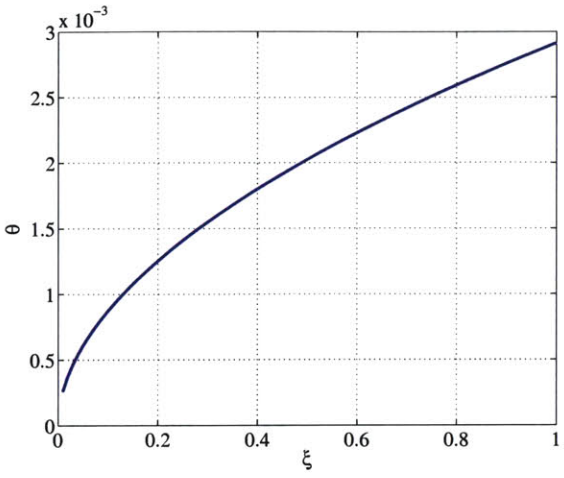

(b) Momentum Thickness

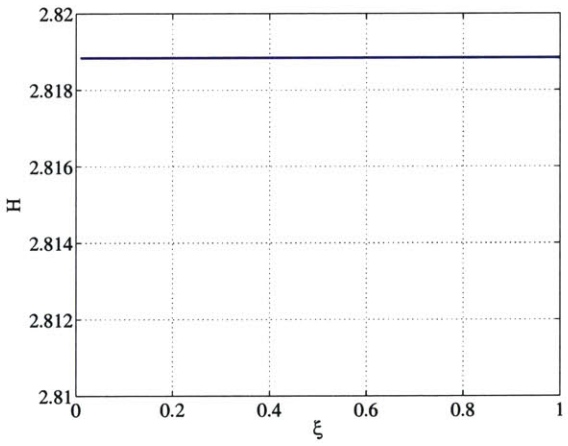

(c) Shape Parameter

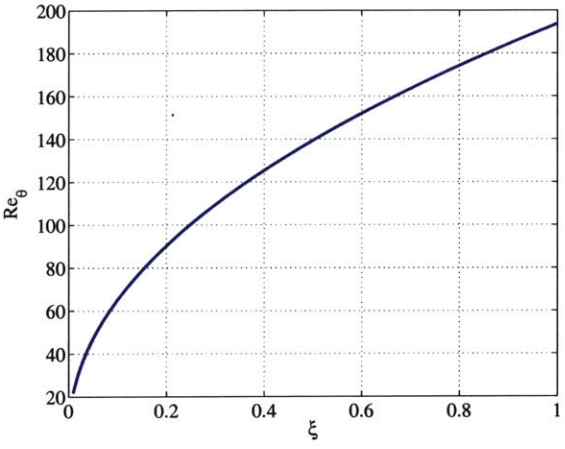

(d) Reynolds Number

Figure A-13: Adverse pressure gradient: δ^*, θ, H, and Re_θ vs. ξ.

A.9.5 Onset of Separation ($\beta_u = -0.088$)

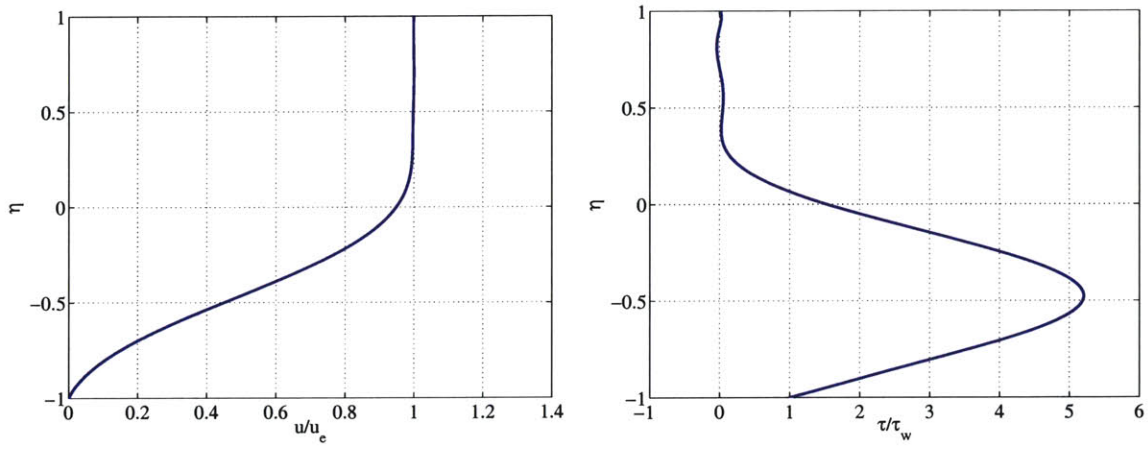

(a) Velocity Profile

(b) Shear Stress Profile

Figure A-14: Onset of separation: u/u_e and τ/τ_w profiles.

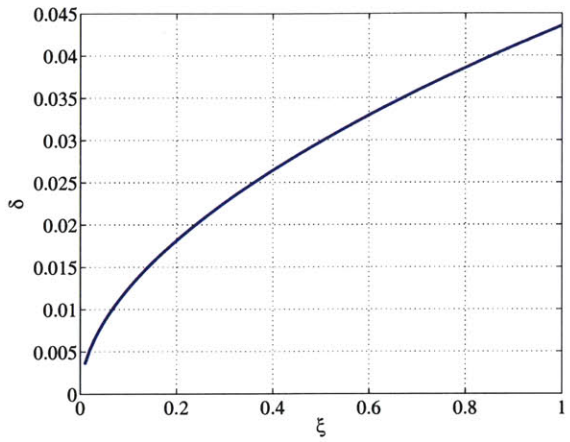

(a) Boundary Layer Thickness

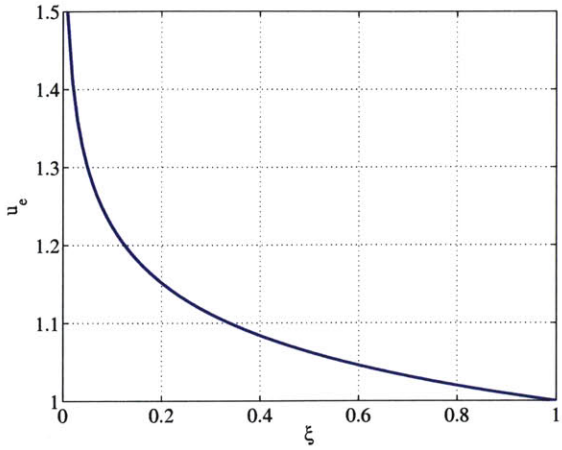

(b) Edge Velocity

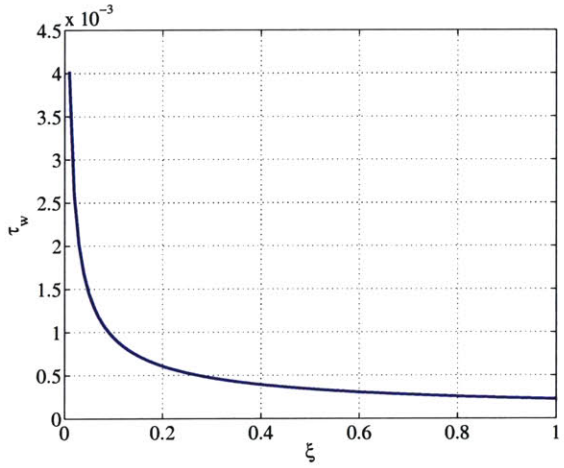

(c) Wall Shear Stress

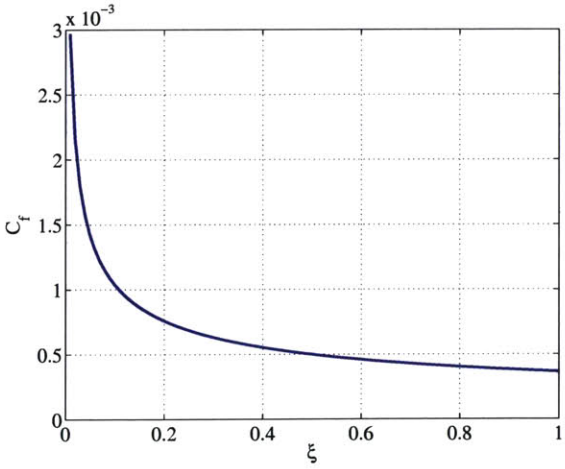

(d) Skin Friction Coefficient

Figure A-15: Onset of separation: δ, u_e, τ_w, and C_f vs. ξ.

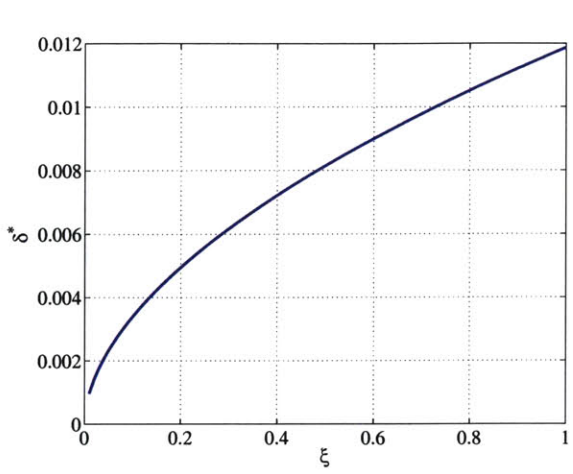

(a) Displacement Thickness

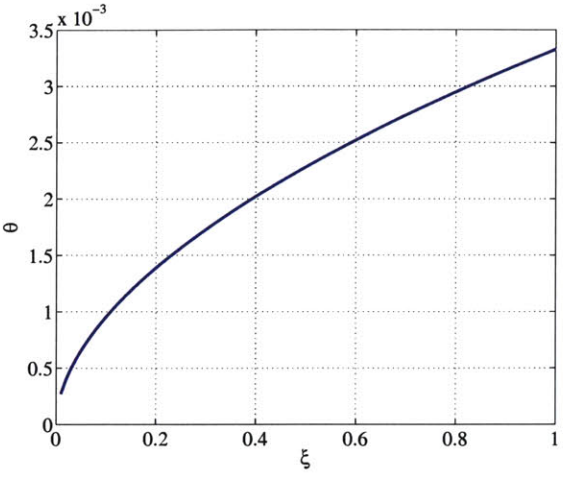

(b) Momentum Thickness

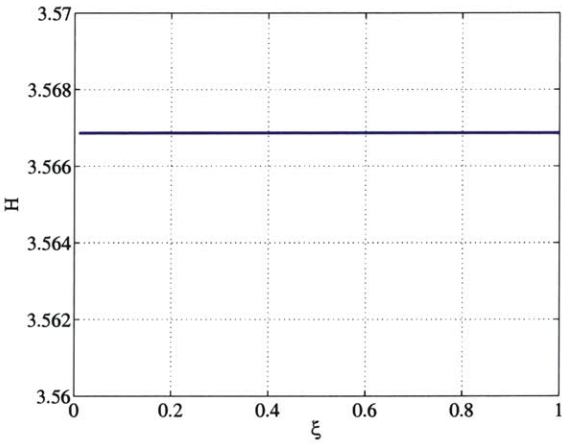

(c) Shape Parameter

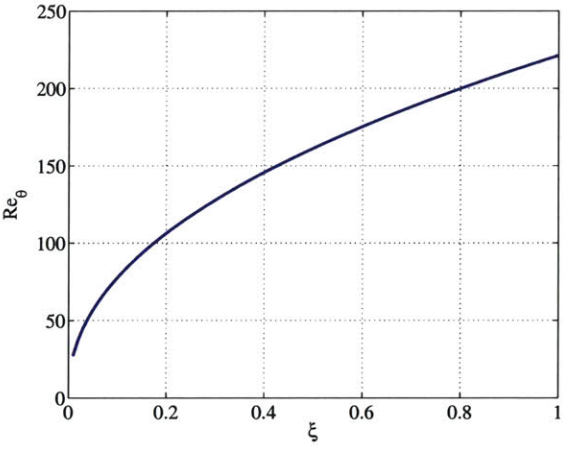

(d) Reynolds Number

Figure A-16: Onset of separation: δ^*, θ, H, and Re_θ vs. ξ.

Appendix B

Interacting Boundary Layer Theory for Separated Flows

The quasi 1-D flow in a diffuser is solved using a two-equation integral method and the spectral formulation. The integral boundary layer equations for both laminar and turbulent flow have identical forms differing only in their closure relations. The edge velocity constraint is formulated using Classical Boundary Layer Theory (CBLT) and Interacting Boundary Layer Theory (IBLT) [4, 10, 11, 24, 25, 26, 27, 42]. The solution procedure for the integral method is outlined and results to laminar and turbulent flow test cases for various Reynolds numbers are reported. The spectral method is applied in solving the diffuser problem in both flow regimes using the FLARE approximation [34, 43] for separated flow. In the case of turbulent flow, the Spalart-Allmaras turbulence model described in Chapter 6 is implemented in the spectral formulation. The agreement in laminar flow solutions from both methodologies is excellent. For turbulent flow, the Spalart-Allmaras turbulence model is strained but the trends in the flow solution variables are nonetheless correct. The incorporation of a wall function in the spectral approximation of the streamwise velocity has little effect in reducing the number of required modes due to the boundary layer thickness constraint.

B.1 Integral Boundary Layer Equations

B.1.1 Laminar Flow

The 2-D, steady, incompressible continuity and x-momentum thin shear layer equations governing the real viscous flow (RVF) in the laminar regime are given by

$$\frac{\partial u}{\partial x} + \frac{\partial v}{\partial y} = 0, \tag{B.1}$$

$$\frac{\partial}{\partial x}\left(u^2\right) + \frac{\partial}{\partial y}\left(uv\right) + \frac{1}{\rho}\frac{\partial p}{\partial x} - \frac{1}{\rho}\frac{\partial \tau}{\partial y} = 0. \tag{B.2}$$

In these expressions, u and v are, respectively, the x- and y-components of the RVF velocity; ρ is the mass density; p is the static pressure and τ is the shear stress given by

$$\tau = \mu\frac{\partial u}{\partial y}, \tag{B.3}$$

where μ is the dynamic viscosity.

B.1.2 Turbulent Flow

The 2-D, steady, incompressible Reynolds-averaged continuity and x-momentum thin shear layer equations governing the real viscous flow (RVF) in the turbulent regime are given by

$$\frac{\partial u}{\partial x} + \frac{\partial v}{\partial y} = 0, \tag{B.4}$$

$$\frac{\partial}{\partial x}\left(u^2\right) + \frac{\partial}{\partial y}\left(uv\right) + \frac{1}{\rho}\frac{\partial p}{\partial x} - \frac{1}{\rho}\frac{\partial \tau}{\partial y} = 0. \tag{B.5}$$

In these expressions, u and v are, respectively, the x- and y-components of the RVF velocity; ρ is the mass density; p is the static pressure and τ is the shear stress given by

$$\tau = \mu\frac{\partial u}{\partial y} - \rho\overline{u'v'}, \tag{B.6}$$

where μ is the dynamic viscosity and $-\rho\overline{u'v'}$ is the turbulent shear (or Reynolds stress).

B.1.3 Dimensional Form

Integrating across the laminar boundary layer

$$\int_0^\delta \left[(u - u_e) \times \text{(B.1)} + \text{(B.2)}\right] dy, \tag{B.7}$$

$$\int_0^\delta \left[\left(u^2 - u_e^2\right) \times \text{(B.1)} + 2u \times \text{(B.2)}\right] dy, \tag{B.8}$$

as well as the turbulent boundary layer

$$\int_0^\delta \left[(u - u_e) \times \text{(B.4)} + \text{(B.5)}\right] dy, \tag{B.9}$$

$$\int_0^\delta \left[\left(u^2 - u_e^2\right) \times \text{(B.4)} + 2u \times \text{(B.5)}\right] dy, \tag{B.10}$$

yields the dimensional form of both the von Kármán integral momentum equation and the integral Kinetic Energy (KE) equation for either case

$$\frac{d}{dx}\left(\rho_e u_e^2 \theta\right) + \rho_e u_e \delta^* \frac{du_e}{dx} = \tau_w, \tag{B.11}$$

$$\frac{d}{dx}\left(\rho_e u_e^3 \theta^*\right) = 2D. \tag{B.12}$$

The displacement thickness δ^*, momentum thickness θ, KE thickness θ^*, and the shear dissipation D are defined by

$$\delta^* \equiv \int_0^\delta \left(1 - \frac{u}{u_e}\right) dy, \tag{B.13}$$

$$\theta \equiv \int_0^\delta \left(1 - \frac{u}{u_e}\right) \frac{u}{u_e} dy, \tag{B.14}$$

$$\theta^* \equiv \int_0^\delta \left(1 - \frac{u^2}{u_e^2}\right) \frac{u}{u_e} dy, \tag{B.15}$$

$$D \equiv \int_0^\delta \tau \frac{\partial u}{\partial y} dy. \tag{B.16}$$

The pressure gradient term has been written in terms of the edge velocity u_e (streamwise component). This comes from the assumption that in a boundary layer

$$p(x, y) \approx p(x) = p_e(x), \tag{B.17}$$

where $p_e(x)$ is the static pressure at the edge and using Bernoulli, it can be shown that

$$\frac{dp_e}{dx} = -\rho_e u_e \frac{du_e}{dx}. \tag{B.18}$$

The edge density $\rho_e = \rho$ since the flow is incompressible. The shear stress at the wall τ_w is given by

$$\tau_w = \mu \left.\frac{\partial u}{\partial y}\right|_{y=0}. \tag{B.19}$$

B.1.4 Dimensionless Form

The dimensionless form of both the von Kármán integral momentum equation and the integral KE equation can be obtained by simply expanding their dimensional form, such that

$$\frac{d\theta}{dx} + (H+2)\frac{\theta}{u_e}\frac{du_e}{dx} = \frac{C_f}{2}, \tag{B.20}$$

$$\frac{d\theta^*}{dx} + 3\frac{\theta^*}{u_e}\frac{du_e}{dx} = 2C_D, \tag{B.21}$$

where the skin friction C_f, dissipation coefficient C_D, and shape parameters H and H^* are defined by

$$C_f \equiv \frac{\tau_w}{\frac{1}{2}\rho_e u_e^2}, \qquad C_D \equiv \frac{D}{\rho_e u_e^3}, \qquad H \equiv \frac{\delta^*}{\theta}, \qquad H^* \equiv \frac{\theta^*}{\theta}. \tag{B.22}$$

Utilizing the relation

$$\frac{1}{H^*}\frac{dH^*}{dx} = \frac{1}{\theta^*}\frac{d\theta^*}{dx} - \frac{1}{\theta}\frac{d\theta}{dx}, \tag{B.23}$$

the so-called shape parameter equation is obtained

$$\frac{\theta}{H^*}\frac{dH^*}{dx} + (1-H)\frac{\theta}{u_e}\frac{du_e}{dx} = \frac{2C_D}{H^*} - \frac{C_f}{2}, \tag{B.24}$$

which is used in lieu of the KE equation. Manipulating this equation further

$$\frac{\theta}{H}\frac{dH}{dx}\left(\frac{H}{H^*}\frac{dH^*}{dH}\right)+(1-H)\frac{\theta}{u_e}\frac{du_e}{dx}=\frac{2C_D}{H^*}-\frac{C_f}{2}. \tag{B.25}$$

B.1.5 Logarithmic Form

In logarithmic form the von Kármán integral momentum equation and the shape parameter equation become

$$\frac{d}{dx}(\ln\theta)+(H+2)\frac{d}{dx}(\ln u_e)=\frac{1}{\theta}\frac{C_f}{2}, \tag{B.26}$$

$$\frac{d}{dx}(\ln H^*)+(1-H)\frac{d}{dx}(\ln u_e)=\frac{1}{\theta}\left(\frac{2C_D}{H^*}-\frac{C_f}{2}\right). \tag{B.27}$$

Equivalently, the shape parameter equation can be written as

$$\frac{d}{dx}(\ln H)\left(\frac{H}{H^*}\frac{dH^*}{dH}\right)+(1-H)\frac{d}{dx}(\ln u_e)=\frac{1}{\theta}\left(\frac{2C_D}{H^*}-\frac{C_f}{2}\right). \tag{B.28}$$

B.1.6 Similarity Form

Noting that

$$\beta_{()}\equiv\frac{x}{()}\frac{d()}{dx}=\frac{d(\ln())}{d(\ln x)}, \tag{B.29}$$

the similarity form of the von Kármán integral momentum equation and the shape parameter equation become

$$\beta_\theta+(H+2)\beta_u=\frac{x}{\theta}\frac{C_f}{2}, \tag{B.30}$$

$$\beta_{H^*}+(1-H)\beta_u=\frac{x}{\theta}\left(\frac{2C_D}{H^*}-\frac{C_f}{2}\right), \tag{B.31}$$

or equivalently for the shape parameter equation

$$\beta_H\left(\frac{H}{H^*}\frac{dH^*}{dH}\right)+(1-H)\beta_u=\frac{x}{\theta}\left(\frac{2C_D}{H^*}-\frac{C_f}{2}\right), \tag{B.32}$$

B.2 Channel Geometry

The diffuser geometry is defined by

$$h(x)=h_0+(h_1-h_0)\left(3x^2-2x^3\right)\qquad\text{with}\qquad 0\le x\le 1, \tag{B.33}$$

where $h_0 = 0.05$ m and $h_1 = 0.1$ m. Only half the diffuser will be treated, assuming symmetry about the center plane, which can also be considered as an inviscid wall. The rate of change of $h(x)$ with x is given by

$$\frac{dh}{dx}=(h_1-h_0)\,6x(1-x)\qquad\text{with}\qquad 0\le x\le 1. \tag{B.34}$$

B.3 Edge Velocity

In Classical Boundary Layer Theory (CBLT), u_e is known a priori from the channel geometry whereas in Interacting Boundary Layer Theory (IBLT), the displacement thickness δ^* also influences u_e, such that

$$\text{CBLT:} \quad u_e(x) = \frac{\dot{m}/\rho}{h(x)} \qquad \text{and} \qquad \text{IBLT:} \quad u_e(x) = \frac{\dot{m}/\rho}{h(x) - \delta^*(x)}. \tag{B.35}$$

The constant volume flux $\dot{m}/\rho$ is known from the inlet flow and geometry. The rate of change of $u_e(x)$ with x is given by

$$\frac{du_e}{dx} = -\frac{u_e}{h}\frac{dh}{dx} \qquad \text{and} \qquad \frac{du_e}{dx} = \frac{u_e}{h - \delta^*}\left(\frac{d\delta^*}{dx} - \frac{dh}{dx}\right). \tag{B.36}$$

In similarity form these become

$$\beta_u = -\frac{x}{h}\frac{dh}{dx} \qquad \text{and} \qquad \beta_u - \frac{\delta^*}{h - \delta^*}\beta_{\delta^*} = -\frac{x}{h - \delta^*}\frac{dh}{dx}. \tag{B.37}$$

B.4 Reynolds Number

The Reynolds number can be appropriately defined with the length of the channel (unity) and the inlet velocity. The latter can also be set to unity so that $\mathrm{Re} = 1/\nu$.

B.5 Solution Procedure

The integral boundary layer equations are valid for both laminar and turbulent flow. However, the empirical closure functions $H^*(H)$, $C_f(H, \mathrm{Re}_\theta)$, and $2C_D/H^*(H, \mathrm{Re}_\theta)$ taken from Drela [8] quantitatively differ between the turbulent and laminar case. The flow is assumed laminar from the leading edge and turbulent downstream of some transition location. The transition location is where the shape parameter H first exceeds some critical value H_{crit}. This will nicely simulate transition induced by pressure gradients and/or laminar separation.

The three unknowns for the integral method are $\theta(x)$, $\delta^*(x)$, and $u_e(x)$. The governing ordinary differential equations (ODEs) are

$$\beta_\theta + (H+2)\beta_u = \frac{x}{\theta}\frac{C_f}{2}, \tag{B.38}$$

$$\beta_H\left(\frac{H}{H^*}\frac{dH^*}{dH}\right) + (1-H)\beta_u = \frac{x}{\theta}\left(\frac{2C_D}{H^*} - \frac{C_f}{2}\right), \tag{B.39}$$

$$\beta_u - \frac{\delta^*}{h - \delta^*}\beta_{\delta^*} = -\frac{x}{h - \delta^*}\frac{dh}{dx}, \tag{B.40}$$

where β_H can be expressed in terms of β_{δ^*} and β_θ as follows

$$\beta_H = \beta_{\delta^*} - \beta_\theta. \tag{B.41}$$

In matrix form these equations become

$$\text{IBLT:} \quad \begin{bmatrix} 1 & 0 & H+2 \\ -\frac{H}{H^*}\frac{dH^*}{dH} & \frac{H}{H^*}\frac{dH^*}{dH} & 1-H \\ 0 & -\frac{\delta^*}{h-\delta^*} & 1 \end{bmatrix} \begin{bmatrix} \beta_\theta \\ \beta_{\delta^*} \\ \beta_u \end{bmatrix} = \begin{bmatrix} \frac{x}{\theta}\frac{C_f}{2} \\ \frac{x}{\theta}\left(\frac{2C_D}{H^*} - \frac{C_f}{2}\right) \\ -\frac{x}{h-\delta^*}\frac{dh}{dx} \end{bmatrix}. \tag{B.42}$$

At any streamwise station x_i the coefficient matrix and righthand side vector can be evaluated. This 3×3 system can easily be solved for β_θ, β_{δ^*}, and β_u. The x-derivatives

$$\frac{d\theta}{dx} = \frac{\theta}{x}\beta_\theta, \qquad \frac{d\delta^*}{dx} = \frac{\delta^*}{x}\beta_{\delta^*}, \qquad \text{and} \qquad \frac{du_e}{dx} = \frac{u_e}{x}\beta_u, \tag{B.43}$$

can then be used to determine θ, δ^*, and u_e at station x_{i+1} using say, Forward-Euler, or some higher-order method such as Predictor-Corrector or Runge-Kutta. However, the integration method will be inaccurate if $\Delta x/x$ is not small (such as near the leading edge).

One way to get around this problem is by using β_θ, β_{δ^*}, and β_u directly, for instance,

$$\beta_\theta = \frac{x}{\theta}\frac{d\theta}{dx} = \frac{d\theta/\theta}{dx/x} = \frac{d(\ln\theta)}{d(\ln x)} \approx \frac{\Delta \ln\theta}{\Delta \ln x} = \frac{\ln\theta_{i+1} - \ln\theta_i}{\ln x_{i+1} - \ln x_i} = \frac{\ln(\theta_{i+1}/\theta_i)}{\ln(x_{i+1}/x_i)}, \tag{B.44}$$

such that

$$\ln(\theta_{i+1}/\theta_i) = \beta_\theta \ln(x_{i+1}/x_i) \qquad \text{or} \qquad \theta_{i+1} = \theta_i \left(\frac{x_{i+1}}{x_i}\right)^{\beta_\theta}. \tag{B.45}$$

Similarly

$$\delta^*_{i+1} = \delta^*_i \left(\frac{x_{i+1}}{x_i}\right)^{\beta_{\delta^*}} \qquad \text{and} \qquad u_{e_{i+1}} = u_{e_i} \left(\frac{x_{i+1}}{x_i}\right)^{\beta_u}. \tag{B.46}$$

These are exact for similar flows (i.e. near the leading edge) no matter how large the quotient $\Delta x/x = (x_{i+1} - x_i)/x_i$ may be. For small $\Delta x/x$ the above power-law integration is equivalent to normal Forward-Euler to first order in $\Delta x/x$. Tabulated Blasius solutions are used to generate solution quantities at the first grid point. This is necessary to start the downstream integration.

To solve the CBLT problem simply neglect δ^* in the third line of the 3×3 system to obtain

$$\text{CBLT:} \quad \begin{bmatrix} 1 & 0 & H+2 \\ -\frac{H}{H^*}\frac{dH^*}{dH} & \frac{H}{H^*}\frac{dH^*}{dH} & 1-H \\ 0 & 0 & 1 \end{bmatrix} \begin{bmatrix} \beta_\theta \\ \beta_{\delta^*} \\ \beta_u \end{bmatrix} = \begin{bmatrix} \frac{x}{\theta}\frac{C_f}{2} \\ \frac{x}{\theta}\left(\frac{2C_D}{H^*} - \frac{C_f}{2}\right) \\ -\frac{x}{h}\frac{dh}{dx} \end{bmatrix}. \tag{B.47}$$

B.6 Spectral Formulation

The spectral method applied to the diffuser problem for either laminar or turbulent flow follows the formulation of Chapters 4 and 5. The Spalart-Allmaras turbulence model described in Chapter 6 is implemented in the spectral formulation for the turbulent case. The only modification occurs in regions of separated flow. For flows with negative wall shear it is necessary to overcome the stability problem in order to continue the calculations past the separation point. This may be done with the approximation suggested by Reyhner and Flügge-Lotz [34]. This approximation, referred to as FLARE by Williams [43], consists of

neglecting $u\partial u/\partial x$ in the x-momentum equation whenever $u < 0$. For turbulent flow, the term $u\partial\tilde{\nu}/\partial x$ in the transport equation must also be neglected for $u < 0$.

B.7 Laminar Test Cases

Both the CBLT and IBLT solutions for Re $= 10^4$, 10^5, 10^6 with $H_{\text{crit}} = 500$ (fully laminar) were computed using the two-equation integral method and the spectral formulation. Figures B-1 to B-3 compare the CBLT solutions whereas Figures B-5 to B-7 compare the IBLT solutions using both methods. Note that $\xi = x$ in the graphs. The spectral method uses $N = 10$ for all the Reynolds numbers in the CBLT case and $N = 20$, 30, 90 for the IBLT case. The integration was performed using the trapezoidal rule with $\Delta\varphi = \pi/180$ in the CBLT case and $\Delta\varphi = \pi/1800$ for the IBLT case. The velocity and shear stress profiles are shown in Figures B-4 and B-8 where $\eta = 2y/\delta - 1$.

The CBLT encounters the Goldstein singularity [36] at separation (i.e. at $\xi \approx 0.185$ m) and fails whereas the IBLT does not. At separation $dH^*/dH = 0$ and $H \approx 4$ such that the coefficient matrices become

$$\text{CBLT:} \quad \begin{bmatrix} 1 & 0 & 6 \\ 0 & 0 & -3 \\ 0 & 0 & 1 \end{bmatrix} \quad \text{and} \quad \text{IBLT:} \quad \begin{bmatrix} 1 & 0 & 6 \\ 0 & 0 & -3 \\ 0 & -\frac{\delta^*}{h-\delta^*} & 1 \end{bmatrix}. \tag{B.48}$$

The matrix is singular for the CBLT case whereas the IBLT matrix is not because of the displacement term $-\delta^*/(h - \delta^*)$.

Furthermore, the separation location for the CBLT is independent of Reynolds number. Conversely, the separation point moves closer to the leading edge as the Reynolds number is increased for the IBLT case. The reason for this is that the edge velocity u_e does not depend on Re in the CBLT case but does so for the IBLT through the displacement thickness δ^*.

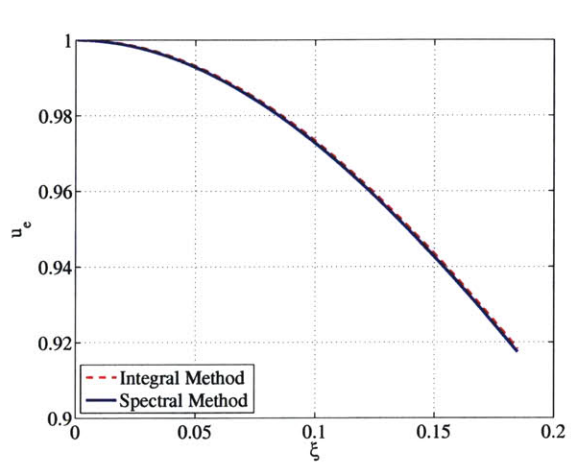

(a) Edge Velocity

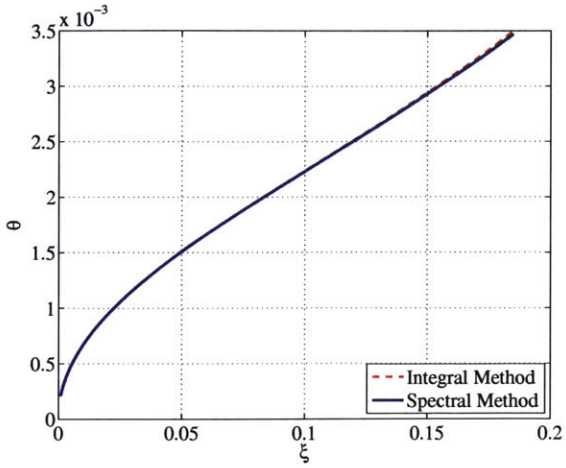

(b) Momentum Thickness

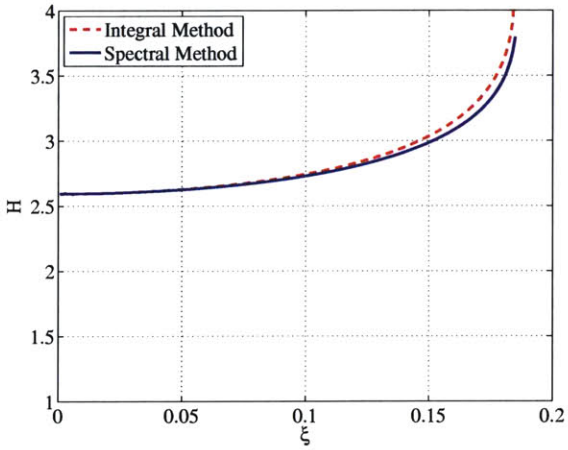

(c) Shape Parameter

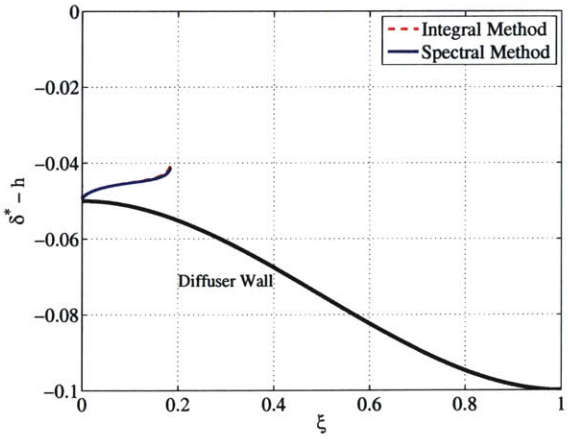

(d) Displacement Surface

Figure B-1: Laminar diffuser CBLT, Re $= 10^4$: u_e, θ, H, and $\delta^* - h$ vs. ξ.

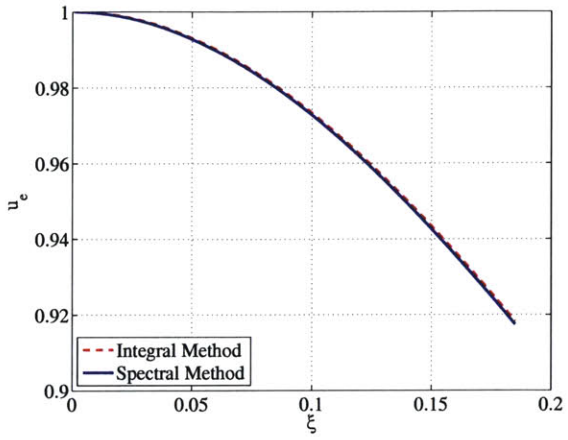

(a) Edge Velocity

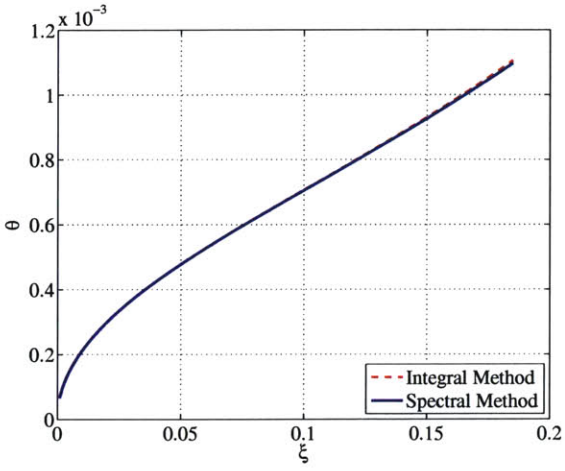

(b) Momentum Thickness

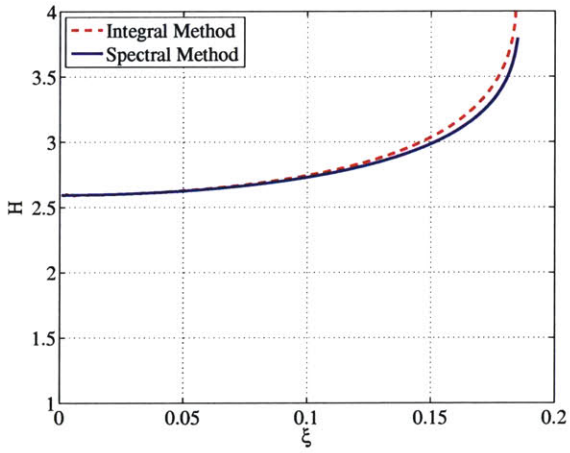

(c) Shape Parameter

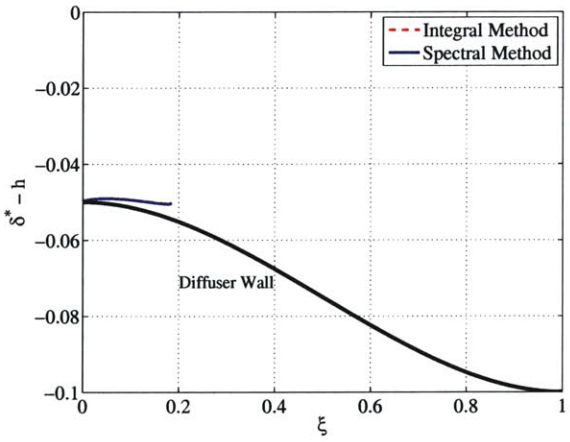

(d) Displacement Surface

Figure B-2: Laminar diffuser CBLT, Re = 10^5: u_e, θ, H, and $\delta^* - h$ vs. ξ.

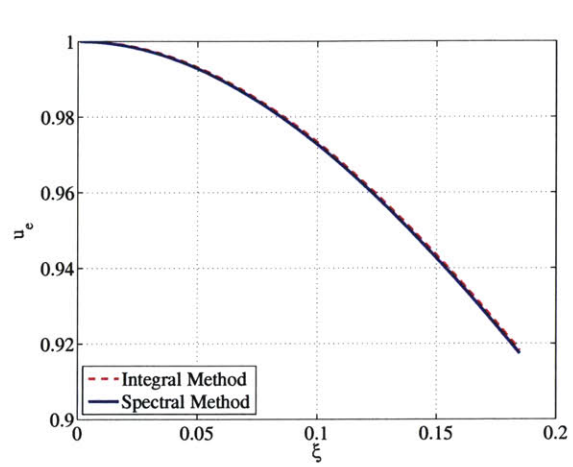

(a) Edge Velocity

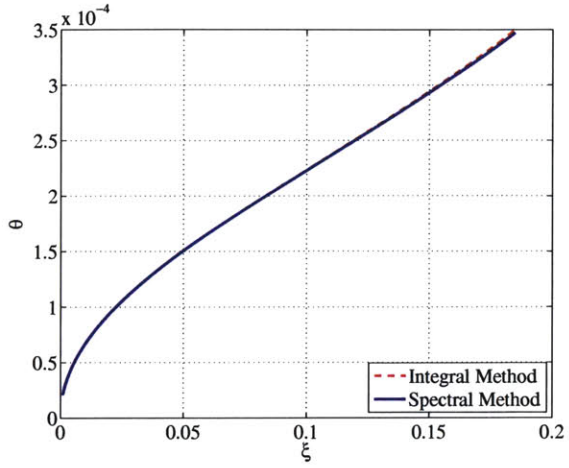

(b) Momentum Thickness

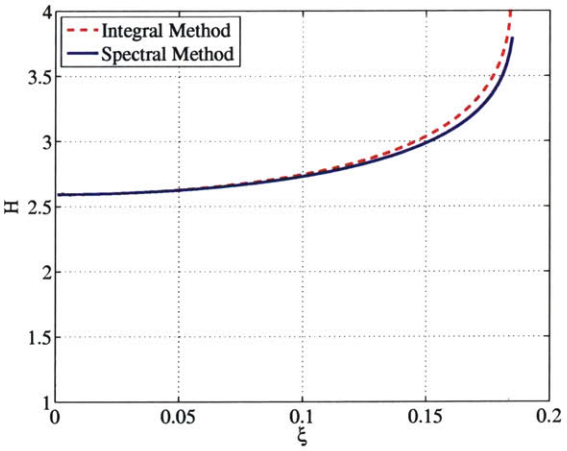

(c) Shape Parameter

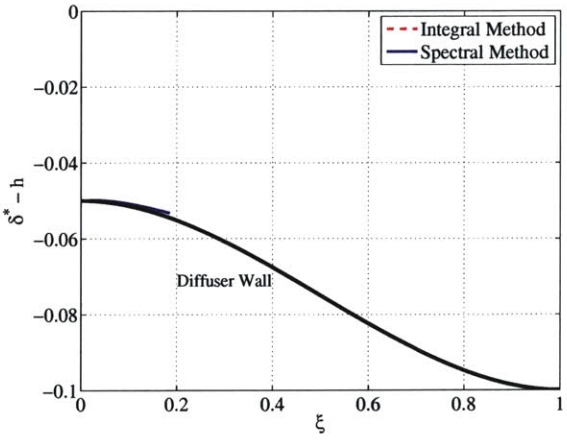

(d) Displacement Surface

Figure B-3: Laminar diffuser CBLT, Re = 10^6: u_e, θ, H, and $\delta^* - h$ vs. ξ.

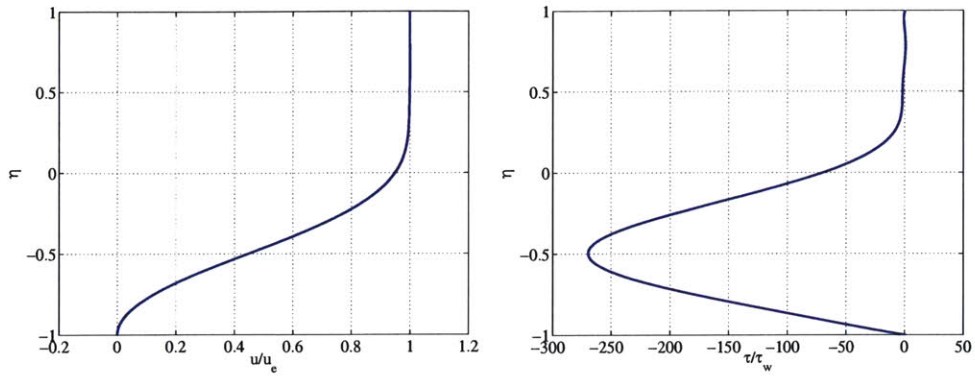

(a) Re = 10^4 (b) Re = 10^4

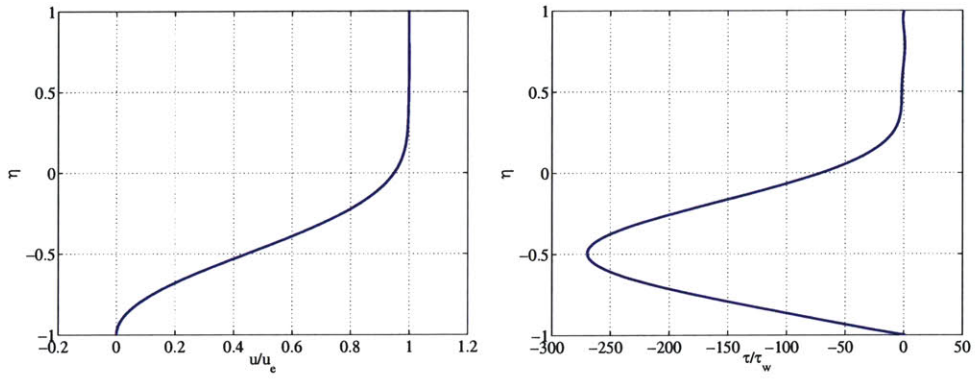

(c) Re = 10^5 (d) Re = 10^5

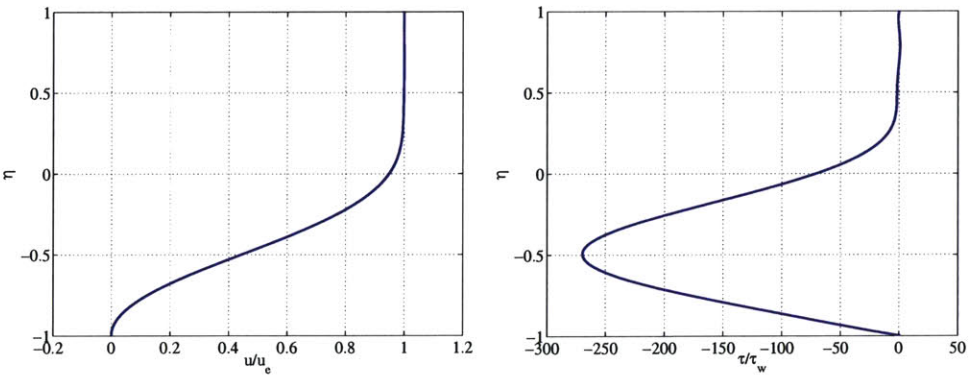

(e) Re = 10^6 (f) Re = 10^6

Figure B-4: Laminar diffuser CBLT: u/u_e and τ/τ_w profiles at $\xi = 0.185$ m.

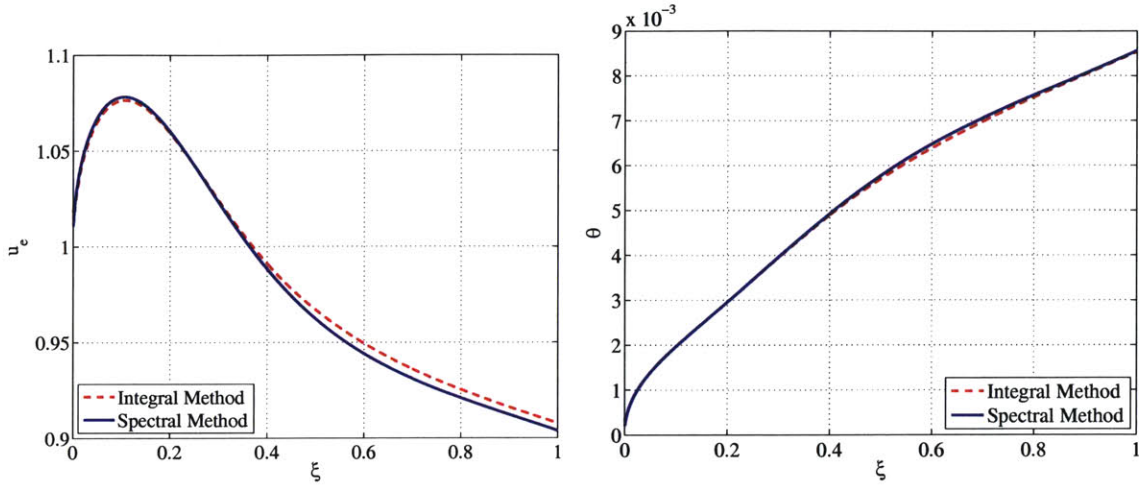

(a) Edge Velocity

(b) Momentum Thickness

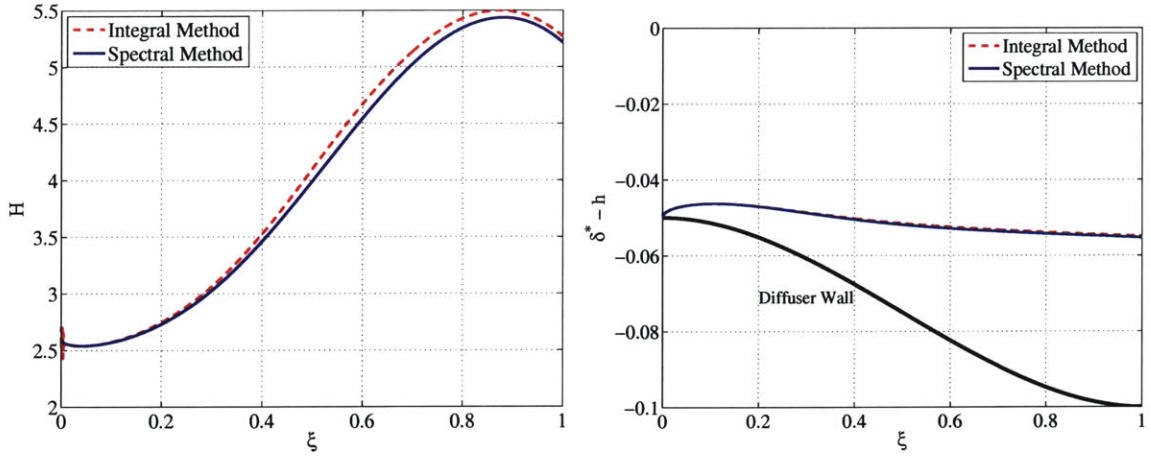

(c) Shape Parameter

(d) Displacement Surface

Figure B-5: Laminar diffuser IBLT, Re $= 10^4$: u_e, θ, H, and $\delta^* - h$ vs. ξ.

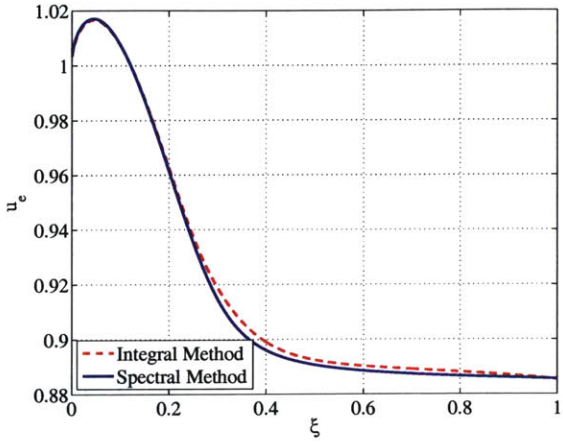

(a) Edge Velocity

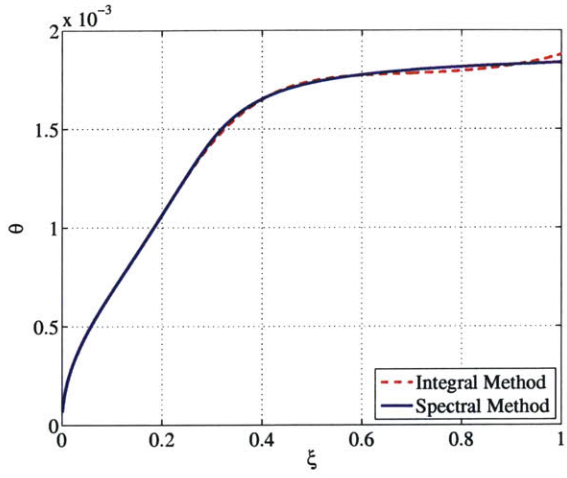

(b) Momentum Thickness

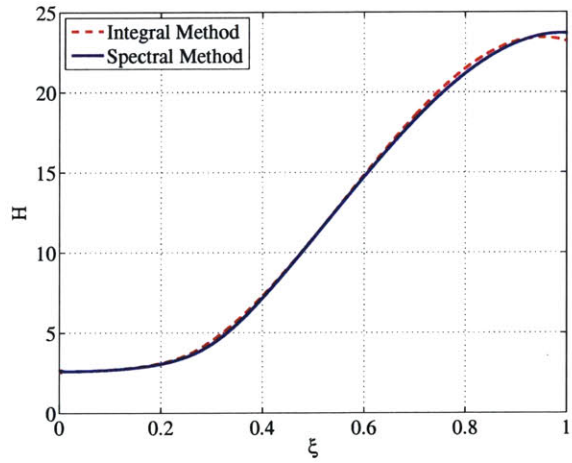

(c) Shape Parameter

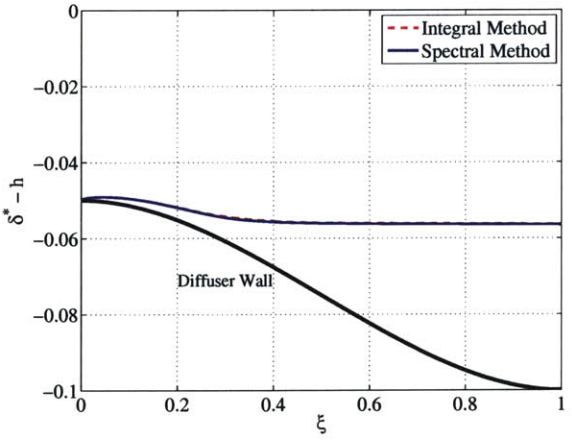

(d) Displacement Surface

Figure B-6: Laminar diffuser IBLT, Re = 10^5: u_e, θ, H, and $\delta^* - h$ vs. ξ.

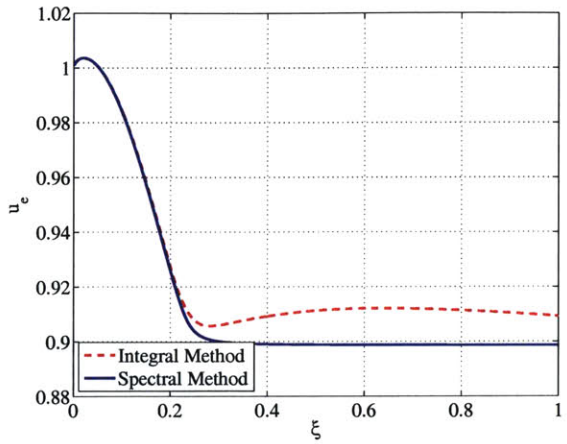

(a) Edge Velocity

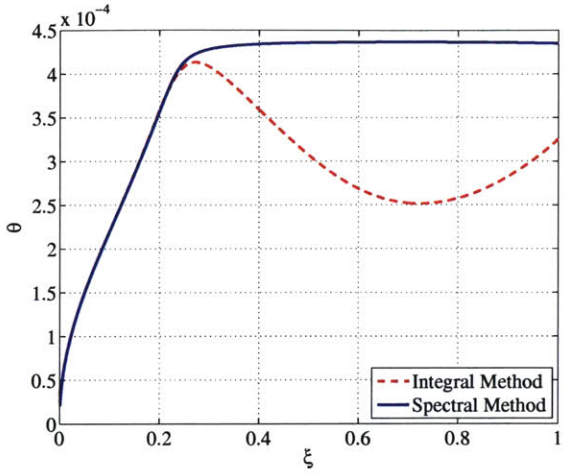

(b) Momentum Thickness

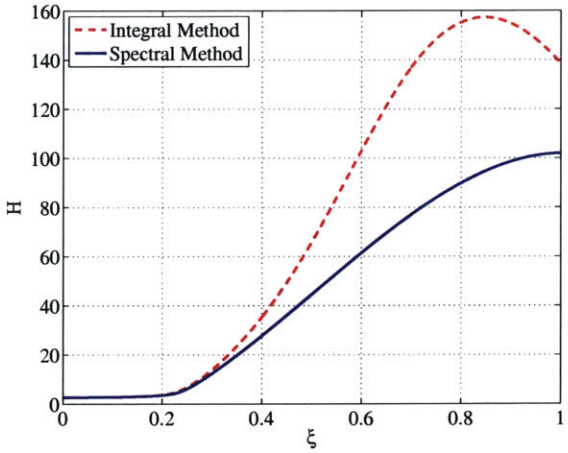

(c) Shape Parameter

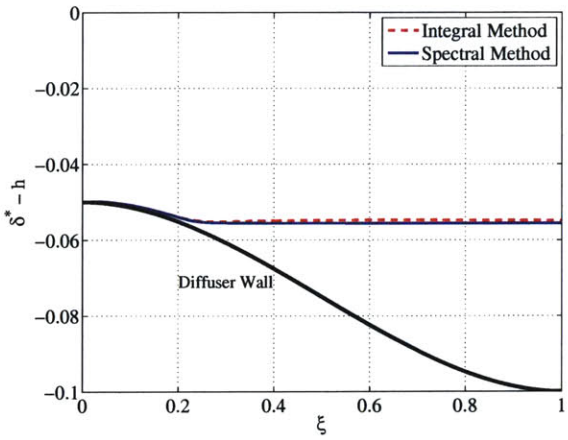

(d) Displacement Surface

Figure B-7: Laminar diffuser IBLT, Re = 10^6: u_e, θ, H, and $\delta^* - h$ vs. ξ.

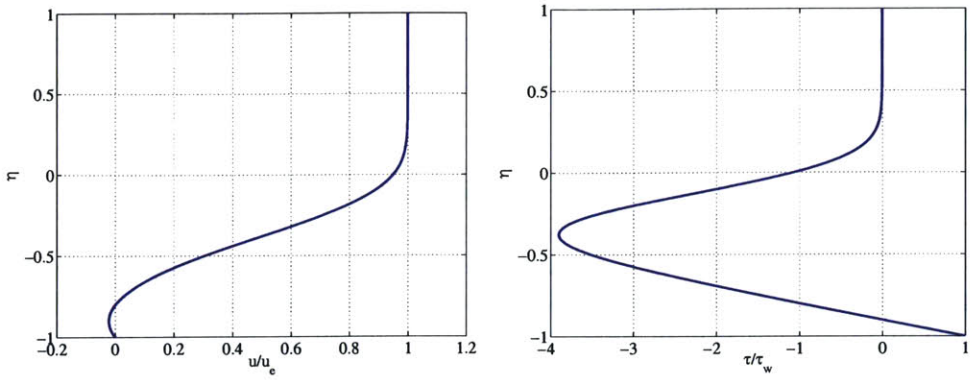

(a) $\mathrm{Re} = 10^4$ (b) $\mathrm{Re} = 10^4$

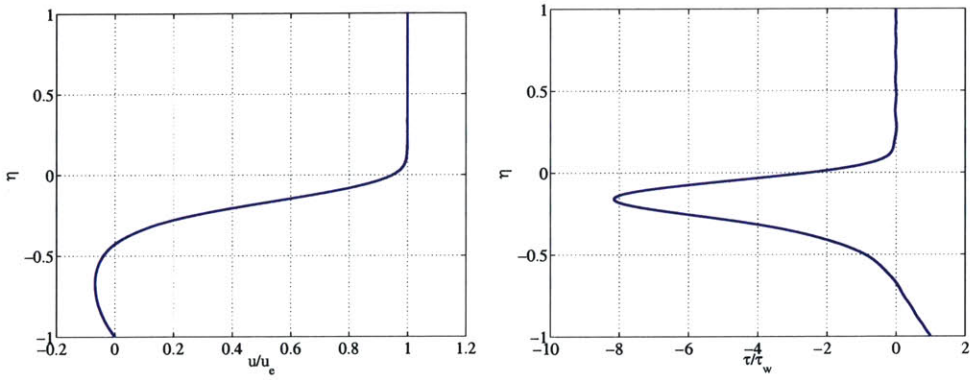

(c) $\mathrm{Re} = 10^5$ (d) $\mathrm{Re} = 10^5$

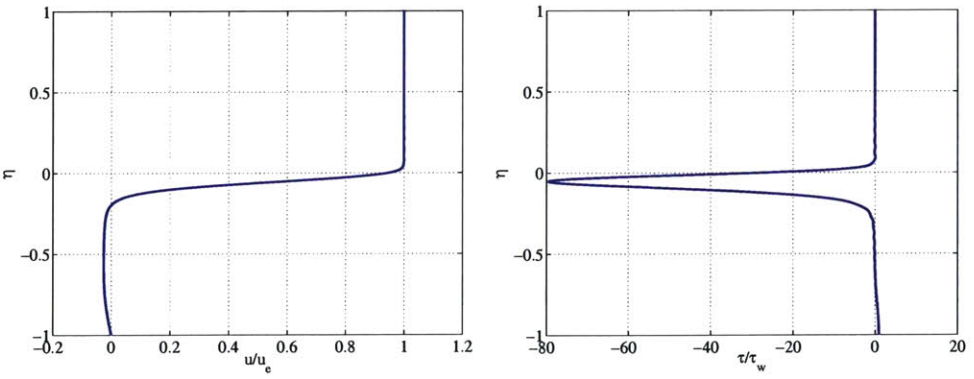

(e) $\mathrm{Re} = 10^6$ (f) $\mathrm{Re} = 10^6$

Figure B-8: Laminar diffuser IBLT: u/u_e and τ/τ_w profiles at $\xi = 1$ m.

B.8 Turbulent Test Cases

A useful measure of diffuser efficiency involves comparison of mixed-out quantities far downstream of the exit. The assumptions are that the skin friction vanishes and the channel width remains constant downstream of the exit. The mixed-out static and stagnation pressure coefficients are given by

$$C_p = \frac{p_\infty - p_{\text{inlet}}}{\frac{1}{2}\rho u_0^2} \qquad \text{and} \qquad C_{p_\circ} = \frac{p_{\circ\infty} - p_{\circ_{\text{inlet}}}}{\frac{1}{2}\rho u_0^2}, \tag{B.49}$$

where C_p measures the diffuser pressure rise while $C_{p_\circ}$ measures the diffuser loss. Using the integral theorems for the conservation of mass and momentum, these coefficients can be expressed more conveniently in terms of the inlet velocity u_0, inlet and exit channel widths h_0 and h_1, and the boundary layer quantities at the exit θ_1 and δ_1^* as follows

$$C_p = 1 + \left(\frac{h_0}{h_1 - \delta_1^*}\right)^2 \left[1 - 2\left(\frac{\delta_1^* + \theta_1}{h_1}\right)\right] - 2\left(\frac{h_0}{h_1}\right)^2, \tag{B.50}$$

$$C_{p_\circ} = \left(\frac{h_0}{h_1 - \delta_1^*}\right)^2 \left[1 - 2\left(\frac{\delta_1^* + \theta_1}{h_1}\right)\right] - \left(\frac{h_0}{h_1}\right)^2. \tag{B.51}$$

Figure B-9 shows the variation of C_p with respect to $C_{p_\circ}$ for $h_0 = 0.05$ m and a range of exit widths 0.1 m $\leq h_1 \leq$ 0.3 m, using Re $= 10^7$ and $H_{\text{crit}} = 3$. As h_1 is increased, the pressure rise increases until separation sets in. After this point, little additional pressure rise is realized and the loss increases rapidly. For small h_1, the loss also increases due to larger u_1 and hence larger skin friction $\tau_{w_1} = \frac{1}{2}C_f \rho u_1^2$.

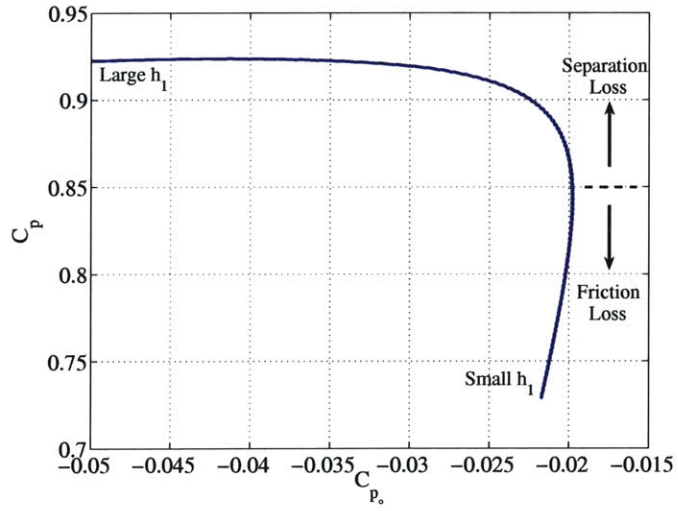

Figure B-9: Graph of C_p vs. $C_{p_\circ}$.

The integral method was used to generate Figure B-9 since using the spectral formulation would have required an exorbitant amount of computational resources. For the sake of comparison, Figure B-10 plots the flow solution for $h_1 = 0.2$ m. In this case, $N = 180$ and $\tilde{N} = 50$. Note that $\xi = x$ in the graphs. It is evident that the Spalart-Allmaras model is

strained in separated flow but the trends are nonetheless correct. The C_p value from the spectral method is 0.8990 whereas the integral method yields 0.9120, a difference of 1.4%. The C_{p_o} value is about 51% off (i.e -0.3853 instead of -0.2550) mainly due to the fact that the separation loss increases rapidly for large h_1.

The velocity and shear stress profiles are shown in Figure B-11 where $\eta = 2y/\delta - 1$. The fact that both the velocity and shear stress are zero for about half the boundary layer thickness forces N and $\tilde{N}$ to be large. This is due to the R_δ constraint. To ease the abruptness with which the eddy viscosity goes to zero, an artificial viscosity ν' replaced ν in the diffusion term of the transport equation. It is given by

$$\nu' = \left[\nu^2 + (K\Delta\eta\delta u)\right]^{1/2}, \tag{B.52}$$

where $K = 1.0$, $\Delta\eta$ is the smallest integration interval scaled with the boundary layer thickness δ, and u is the x-component of the RVF velocity.

The spectral solution to the turbulent diffuser problem with $h_1 = 0.2$ m was also computed with the incorporation of the wall function. The benefits of using a wall function are rendered useless by the fact that the velocity and shear stress are zero for half the boundary layer thickness. As such, $N = 150$ and $\tilde{N} = 50$. Figure B-12 compares the flow solution and Figure B-13 depicts the velocity and shear stress profiles. These are almost identical to Figures B-10 and B-11, respectively. The C_p and C_{p_o} values are also the same.

Figure B-14 breaks down the velocity profile into its two contributions. The Spalding profile contributes a negative velocity since the friction velocity, u_τ, is negative for flow reversal. The Chebyshev profile is zero (on the average) following the constraint equation R_{u_τ}. The function w_{u_τ} was taken from the turbulent jet case

$$w_{u_\tau} = \frac{1}{2}\left\{1 - \tanh\left[K\left(\frac{y}{\delta} - \frac{y^*}{\delta}\right)\right]\right\}, \tag{B.53}$$

where $K = 1000$. The term y^* was chosen to be 0.1δ. Noting that $\eta = 2y/\delta - 1$ and $\eta^* = 2y^*/\delta - 1$ the expression can be simplified to

$$w_{u_\tau} = \frac{1}{2}\left\{1 - \tanh\left[\frac{K}{2}(\eta - \eta^*)\right]\right\}. \tag{B.54}$$

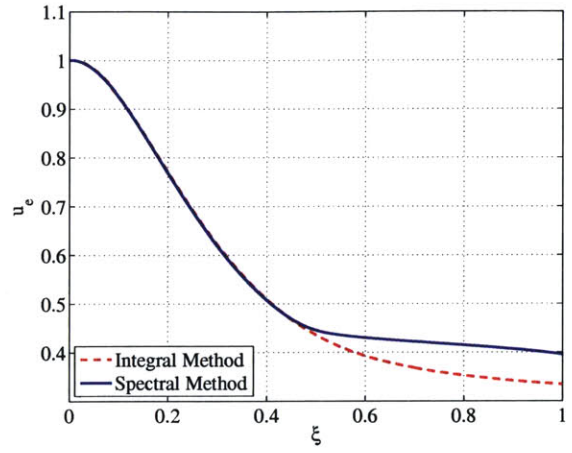

(a) Edge Velocity

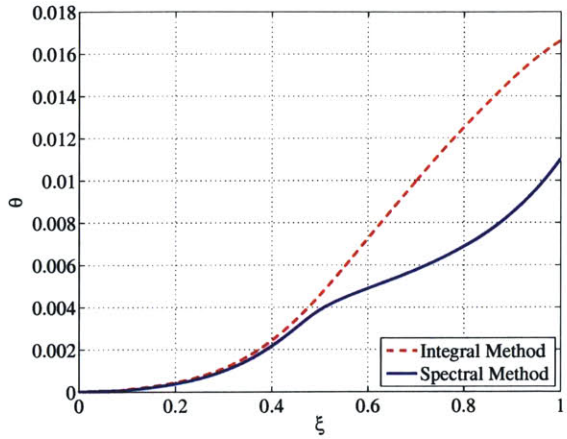

(b) Momentum Thickness

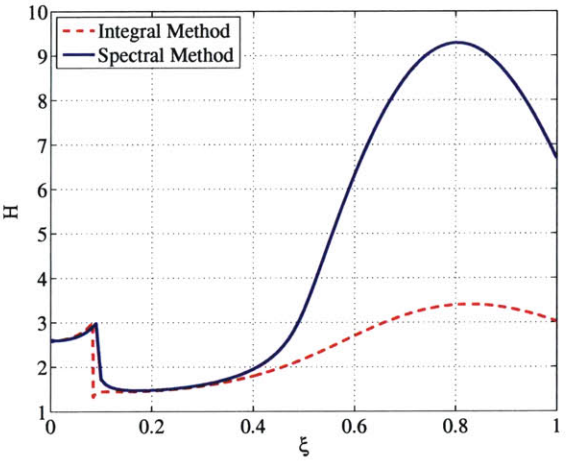

(c) Shape Parameter

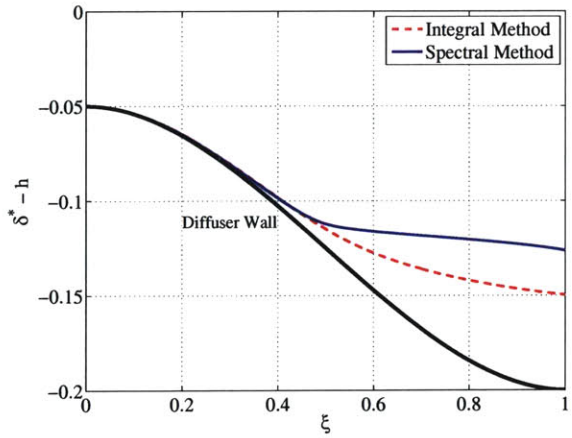

(d) Displacement Surface

Figure B-10: Turbulent diffuser: u_e, θ, H, and $\delta^* - h$ vs. ξ.

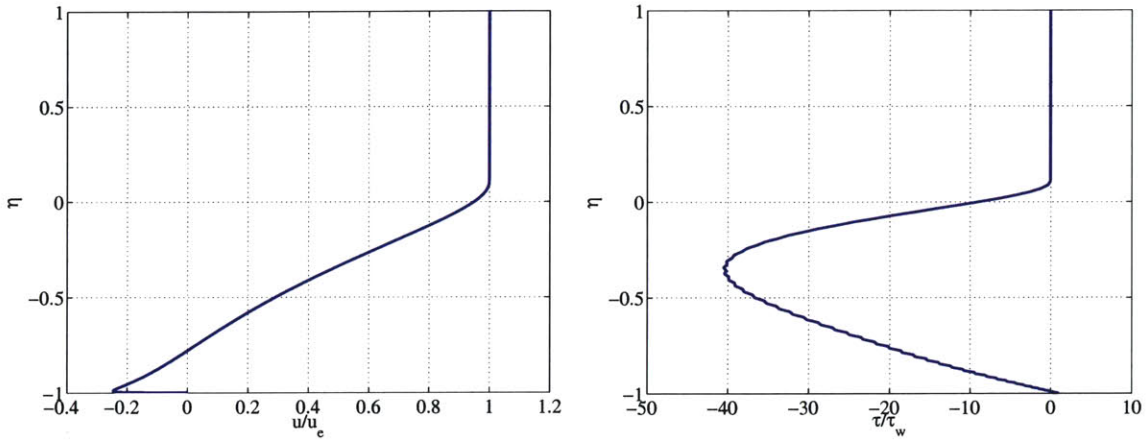

(a) Velocity Profile

(b) Shear Stress Profile

Figure B-11: Turbulent diffuser: u/u_e and τ/τ_w profiles at $\xi = 1$ m.

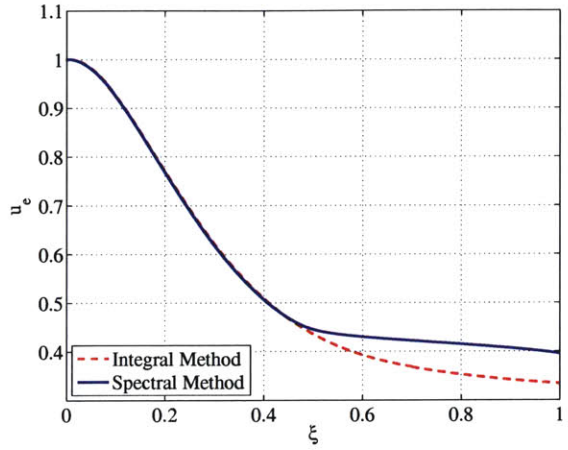

(a) Edge Velocity

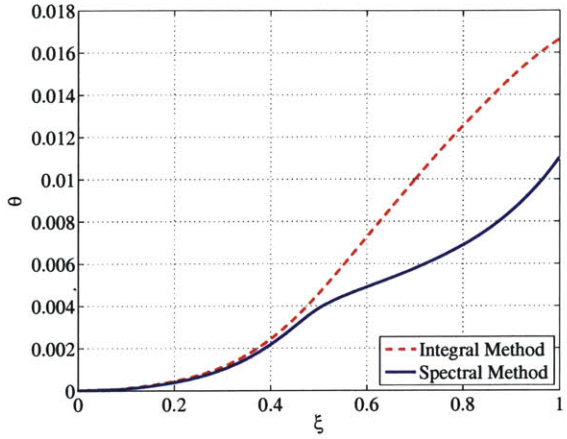

(b) Momentum Thickness

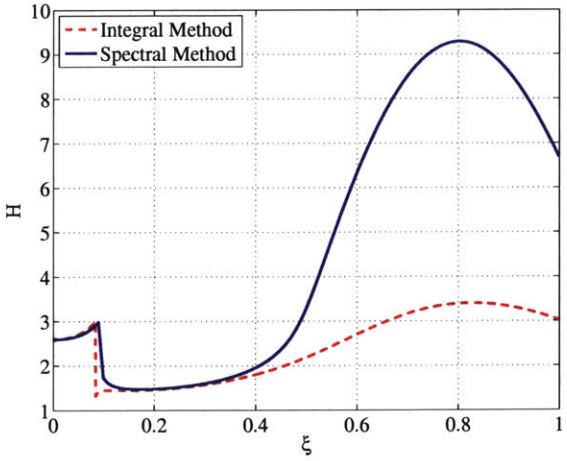

(c) Shape Parameter

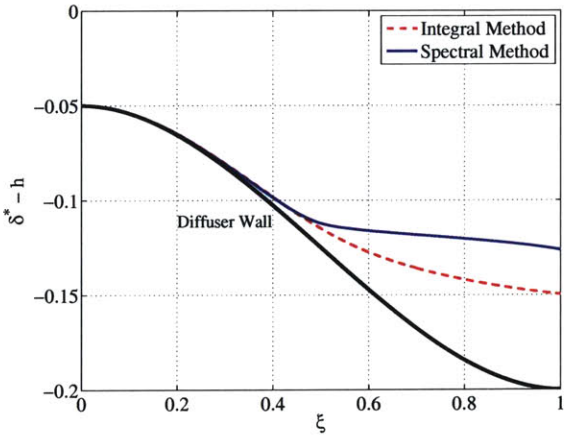

(d) Displacement Surface

Figure B-12: Turbulent diffuser (WF): u_e, θ, H, and $\delta^* - h$ vs. ξ.

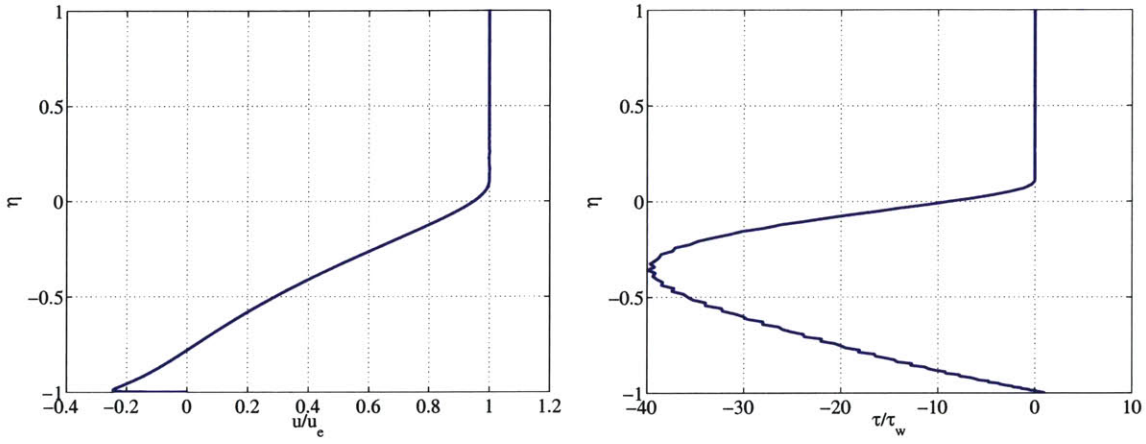

(a) Velocity Profile

(b) Shear Stress Profile

Figure B-13: Turbulent diffuser (WF): u/u_e and τ/τ_w profiles at $\xi = 1$ m.

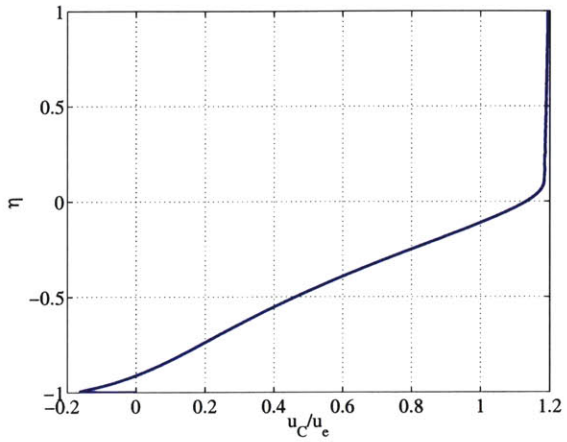

(a) Chebyshev

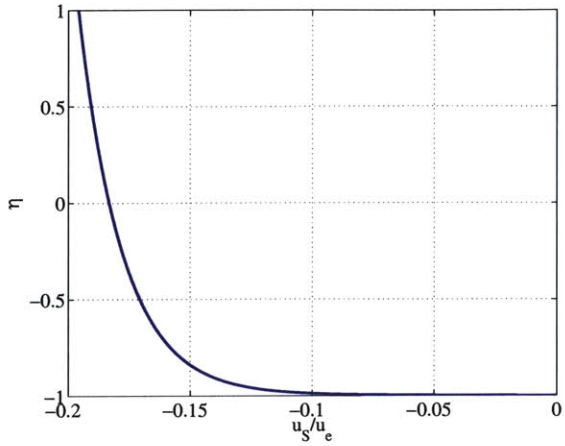

(b) Spalding

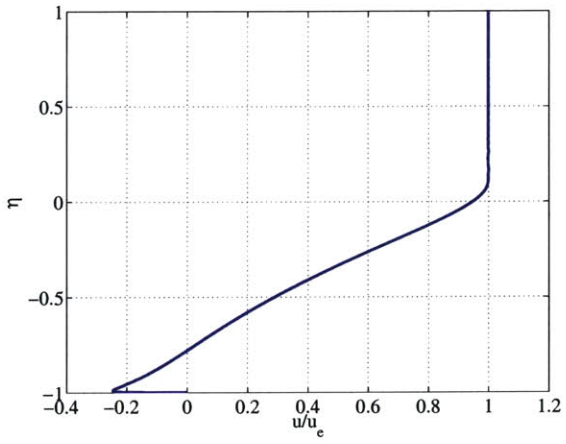

(c) Total

Figure B-14: Velocity profile contributions (WF).

Bibliography

[1] H. Blasius. Grenzschichten in flüssikeiten mit kleiner reibung. *Z. Angew. Math. Phys.*, 56:1–37, 1908. [English translation in NACA Technical Memo. 1256].

[2] J. P. Boyd. *Chebyshev and Fourier Spectral Methods.* Dover, New York, NY, second edition, 2001.

[3] C. Canuto et al. *Spectral Methods in Fluid Dynamics.* Springer-Verlag, New York, NY, 1988.

[4] J. E. Carter. A new boundary layer inviscid iteration technique for separated flow. AIAA-79-1450, July 1979.

[5] F. H. Clauser. The turbulent boundary layer. *Adv. in Appl. Mech.*, 4:1–51, 1956.

[6] D. E. Coles. The law of the wake in the turbulent boundary layer. *J. Fluid Mech.*, 1:191–226, 1956.

[7] D. E. Coles and E. A. Hirst, editors. *Computation of Turbulent Boundary Layers*, number 2 in 1968 AFOSR-IFP Standford Conference, Mech. Eng. Dept. Standford University, Standford, CA, 1968.

[8] M. Drela. *Two-Dimensional Transonic Aerodynamic Design and Analysis Using the Euler Equations.* Ph.D. thesis, Massachusetts Institute of Technology, Department of Aeronautics and Astronautics, December 1985.

[9] M. Drela. Integral boundary layer method with a one-equation turbulence model. Unpublished work, July 1994.

[10] M. Drela and M. B. Giles. Viscous-inviscid analysis of transonic and low Reynolds number airfoils. *AIAA Journal*, 25(10):1347–1355, October 1987.

[11] D. E. Edwards and J. E. Carter. A quasi-simultaneous finite difference approach for strongly interacting flow. In *Third Symposium on Numerical and Physical Aspects of Aerodynamic Flows*, Long Beach, CA, January 1985.

[12] E. Eliasen et al. On a numerical method for integration of the hydrodynamical equations with a spectral representation of the horizontal fields. Technical Report 2, Copenhagen University, Dept. of Meteorol., Copenhagen, Denmark, 1970.

[13] V. M. Falkner and S. W. Skan. Some approximate solutions of the boundary layer equations. *Phil. Mag.*, 12(7):865–896, 1931. [see also *Aero. Res. Council London*, R & M 1314, 1930].

[14] B. A. Finlayson. *The Method of Weighted Residuals and Variational Principles.* Academic Press, New York, NY, 1972.

[15] D. Gottlieb and S. A. Orszag. *Numerical Analysis of Spectral Methods: Theory and Applications*, volume 26 of *Regional Conference Series in Applied Mathematics.* Society for Industrial and Applied Mathematics, Philadelphia, PA, 1977.

[16] D. R. Hartree. On an equation occurring in Falkner and Skan's approximate treatment of the equations of the boundary layer. *Proc. Cambridge Phil. Soc.*, 33:223–239, 1937.

[17] M. Y. Hussaini and T. A. Zang. Spectral methods in fluid dynamics. *Ann. Rev. Fluid Mech.*, 19:339–367, 1987.

[18] R. Iglisch. Exakte berechnung der laminaren reibungsschicht an der längsangeströmten ebenen platte mit homogener absaugung. *Schr. Deutsch. Akad. Luftfahrtforschung*, 8(ser. B):1–51, 1944. (translated as NACA Technical Memo. 1205).

[19] J. L. Kerrebrock et al. Aspirated compressors. ASME Paper 97-GT-525, June 1997.

[20] J. L. Kerrebrock et al. A family of designs for aspirated compressors. ASME Paper 98-GT-196, June 1998.

[21] J. Kestin and L. N. Persen. The transfer of heat across a turbulent boundary layer at very high Prandtl numbers. *Internat. J. Heat Mass Transfer*, 5:355–371, 1962.

[22] H. -O. Kreiss and J. Oliger. Comparison of accurate methods for the integration of hyperbolic equations. Technical Report 36, Uppsala University, Dept. Comput. Sci., Uppsala, Sweden, 1971.

[23] C. Lanczos. Trigonometric interpolation of empirical and analytical functions. *Journal of Mathematics and Physics*, 17:123–199, 1938.

[24] J. C. Le Balleur. Strong matching method for computing transonic viscous flows including wakes and separations. *La Recherche Aérospatiale*, 1981-3:21–45, 1981. English Edition.

[25] M. J. Lighthill. On displacement thickness. *Journal of Fluid Mechanics*, 4:383–392, 1958.

[26] R. C. Lock and B. R. Williams. Viscous-inviscid interactions in external aerodynamics. *Progress in Aeronautical Sciences*, 24:51–171, 1987.

[27] R. E. Melnik et al. The computation of viscid/inviscid interaction on airfoils with separated flow. In *Third Symposium on Numerical and Physical Aspects of Aerodynamic Flows*, Long Beach, CA, January 1985.

[28] A. A. Merchant. Design and analysis of supercritical airfoils with boundary layer suction. Masters thesis, Massachusetts Institute of Technology, Department of Aeronautics and Astronautics, June 1996.

[29] A. A. Merchant. *Design and Analysis of Axial Aspirated Compressor Stages.* Ph.D. thesis, Massachusetts Institute of Technology, Department of Aeronautics and Astronautics, June 1999.

[30] A. A. Merchant. Aerodynamic design and performance of aspirated airfoils. ASME Paper 2002-GT-30369, June 2002.

[31] S. A. Orszag. Numerical methods for the simulation of turbulence. *Phys. Fluids*, 12:250–257 (Suppl. II), 1969.

[32] S. A. Orszag. Numerical simulation of incompressible flows within simple boundaries: I. Galerkin (spectral) representations. *Stud. Appl. Math.*, 50:293–327, 1972.

[33] R. Peyret. *Spectral Methods for Incompressible Viscous Flow.* Springer-Verlag, New York, NY, 2002.

[34] T. A. Reyhner and I. Flügge-Lotz. The interaction of a shock wave with a laminar boundary layer. *Int. J. Non-Linear Mech.*, 3:173–179, 1968.

[35] L. Rosenhead. *Laminar Boundary Layers.* Oxford University Press, London, England, 1963.

[36] H. Schlichting. *Boundary Layer Theory.* McGraw-Hill, New York, NY, seventh edition, 1979.

[37] B. J. Schuler et al. Experimental investigation of an aspirated fan stage. ASME Paper 2002-GT-30370, June 2002.

[38] P. R. Spalart and S. R. Allmaras. A one-equation turbulence model for aerodynamic flows. AIAA-92-0439, 1992.

[39] D. B. Spalding. A single formula for the law of the wall. *J. Appl. Mech.*, 28:455–457, 1961.

[40] T. N. Stevenson. A law of the wall for turbulent boundary layers with suction or injection. Technical Report 166, Cranfield College, Dept. of Aero., Cranfield, England, 1963.

[41] F. M. White. *Viscous Fluid Flow.* McGraw-Hill, New York, NY, second edition, 1991.

[42] L. B. Wigton and M. Holt. Viscous-inviscid interaction in transonic flow. AIAA-81-1003, 1981.

[43] P. G. Williams. A reverse-flow computation in the theory of self-induced separation. In *Proc. 4th Int. Conf. Numerical Methods in Fluid Dynamics*, number 35 in Lecture Notes in Physics, pages 445–451. Springer-Verlag, 1975.

[44] H. H. Youngren. Analysis and design of transonic cascades with splitter vanes. Masters thesis, Massachusetts Institute of Technology, Department of Aeronautics and Astronautics, February 1991.

[45] M. D. Zhou and I. Wygnanski. Parameters governing the turbulent wall jet in an external stream. *AIAA Journal*, 31(5):848–853, May 1993.